



Reconfigurable reflectarray with a flexible ground plane

Claire Benteyn

► To cite this version:

Claire Benteyn. Reconfigurable reflectarray with a flexible ground plane. Electronics. INSA de Rennes; Heriot-Watt university (Edimbourg, GB), 2021. English. NNT : 2021ISAR0010 . tel-03639279

HAL Id: tel-03639279

<https://theses.hal.science/tel-03639279>

Submitted on 12 Apr 2022

HAL is a multi-disciplinary open access archive for the deposit and dissemination of scientific research documents, whether they are published or not. The documents may come from teaching and research institutions in France or abroad, or from public or private research centers.

L'archive ouverte pluridisciplinaire **HAL**, est destinée au dépôt et à la diffusion de documents scientifiques de niveau recherche, publiés ou non, émanant des établissements d'enseignement et de recherche français ou étrangers, des laboratoires publics ou privés.

THESE DE DOCTORAT DE

L'INSTITUT NATIONAL DES SCIENCES
APPLIQUEES RENNES & HERIOT WATT UNIVERSITY

ECOLE DOCTORALE N° 601
*Mathématiques et Sciences et Technologies
de l'Information et de la Communication*
Spécialité : *Electronique*

Par

Claire BENTEYN

Reconfigurable reflectarray with a flexible ground plane

Thèse présentée et soutenue à Rennes, le 20 avril 2021

Unité de recherche : Institut d'Electronique et des Technologies du numéRique (IETR), UMR CNRS 6164

Thèse N° : 21ISAR 10 / D21 - 10

Rapporteurs avant soutenance :

Thierry MONEDIERE
Alexandros FEREDISIS

Professeur, Université de Limoges
Senior lecturer, University of Birmingham

Composition du Jury :

Président : Marc Philippe Yves DESMULLIEZ
Examineurs : Marc Philippe Yves DESMULLIEZ
Christine LETROU
Dir. de thèse : Raphaël GILLARD
Co-dir. de thèse : George GOUSSETIS

Professeur, Heriot Watt University
Professeur, Heriot Watt University
Professeur, Paris- Tech Sud
Professeur, INSA Rennes
Professeur, Heriot Watt University

Invité(s)

Erwan FOURN
Leri DATASHVILI
Hervé LEGAY

Maître de conférences, INSA Rennes
Docteur et CEO, Large Space Structures GmbH
Docteur et Ingénieur de Recherche, Thales Alenia Space

Intitulé de la thèse :

Reconfigurable reflectarray with a flexible ground plane

Claire BENTEYN



Document protégé par les droits d'auteur

HERIOT-WATT UNIVERSITY

Reconfigurable Reflectarray with a Flexible Ground Plane

Author:

Claire BENTEYN

Supervisors:

Raphaël GILLARD

George GOUSSETIS

Co-supervisor:

Erwan FOURN

Submitted for the degree of Doctor of Philosophy

in the

School of Engineering and Physical Sciences

July 2021



Research Thesis Submission

Please note this form should be bound into the submitted thesis.

Name:	Claire BENTEYN		
School:	Heriot Watt University, School of Engineering and Physical Sciences		
Version: <i>(i.e. First, Resubmission, Final)</i>	First	Degree Sought:	Doctor of Philosophy

Declaration

In accordance with the appropriate regulations I hereby submit my thesis and I declare that:

1. The thesis embodies the results of my own work and has been composed by myself
2. Where appropriate, I have made acknowledgement of the work of others
3. The thesis is the correct version for submission and is the same version as any electronic versions submitted*.
4. My thesis for the award referred to, deposited in the Heriot-Watt University Library, should be made available for loan or photocopying and be available via the Institutional Repository, subject to such conditions as the Librarian may require
5. I understand that as a student of the University I am required to abide by the Regulations of the University and to conform to its discipline.
6. I confirm that the thesis has been verified against plagiarism via an approved plagiarism detection application e.g. Turnitin.

ONLY for submissions including published works


Please note you are only required to complete the Inclusion of Published Works Form (page 2) if your thesis contains published works)

7. Where the thesis contains published outputs under Regulation 6 (9.1.2) or Regulation 43 (9) these are accompanied by a critical review which accurately describes my contribution to the research and, for multi-author outputs, a signed declaration indicating the contribution of each author (complete)
8. Inclusion of published outputs under Regulation 6 (9.1.2) or Regulation 43 (9) shall not constitute plagiarism.

* Please note that it is the responsibility of the candidate to ensure that the correct version of the thesis is submitted.

Signature of Candidate:		Date:	06.06.2021
-------------------------	---	-------	------------

Submission

Submitted By <i>(name in capitals)</i> :	Claire BENTEYN
Signature of Individual Submitting:	
Date Submitted:	06.06.2021

For Completion in the Student Service Centre (SSC)


Limited Access	Requested	Yes	No	Approved	Yes	No
E-thesis Submitted <i>(mandatory for final theses)</i>						
Received in the SSC by <i>(name in capitals)</i> :				Date:		


Inclusion of Published Works

Please note you are only required to complete the Inclusion of Published Works Form if your thesis contains published works under Regulation 6 (9.1.2)

Declaration

This thesis contains one or more multi-author published works. In accordance with Regulation 6 (9.1.2) I hereby declare that the contributions of each author to these publications is as follows:

Citation details	C. Benteyn, E. Fourn, R. Gillard, E. Girard, G. Goussetis, L. Datashvili, <i>Réseaux réflecteurs reconfigurables mécaniquement</i> , XXIèmes Journées Nationales Microondes, Caen, 2019.
Author 1	C. Benteyn
Author 2	E. Fourn, R. Gillard, E. Girard, G. Goussetis, L. Datashvili
Signature:	
Date:	2019

Citation details	C. Benteyn, R. Gillard, E. Fourn, G. Goussetis, H. Legay, L. Datashvili, <i>A Design Methodology for Reconfigurable Reflectarrays with a Deformable Ground</i> , EuCap; 2020.
Author 1	C. Benteyn
Author 2	R. Gillard, E. Fourn, G. Goussetis, H. Legay, L. Datashvili
Signature:	
Date:	2020

Please included additional citations as required.

AVIS DU JURY SUR LA REPRODUCTION DE LA THESE SOUTENUE

Titre de la thèse:

Reconfigurable reflectarray with a flexible ground plane

Nom Prénom de l'auteur : BENTEYN CLAIRE

Membres du jury :

- Monsieur FERESIDIS Alexandros
- Monsieur MONEDIERE Thierry
- Monsieur GILLARD Raphaël
- Madame LETROU Christine
- Monsieur DESMULLIEZ Marc Philippe Yves
- Monsieur GOUSSETIS George

Président du jury : Marc DESMULLIEZ

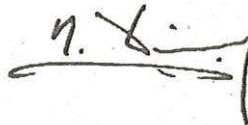
Date de la soutenance : 20 Avril 2021

Reproduction de la these soutenue

- ☒ Thèse pouvant être reproduite en l'état
☐ Thèse pouvant être reproduite après corrections suggérées

Fait à Rennes, le 20 Avril 2021

Signature du président de jury



Le Directeur,


Abdellatif MIRAOU


Acknowledgements

This document represents several years of work that couldn't have been done without the help and the support of many people.

First of all, I want to thank my directors and supervisor from INSA Rennes and Heriot Watt University, Raphaël Gillard, Erwan Fourn, and George Goussetis for their help, their advice, and work directions that they gave me during the whole thesis. They have been huge and continuous support even when I began to be less motivated by the redaction of the manuscript. In parallel, I also remember the good moments we had during the REVOLVE week or during the coffee break (with a chocolate bar as a side). To summarize: "Thank you and Merci, I am very glad that you were my supervisors".

I think also about Leri Datashvili from Large Space Structures who helps me a lot with the mechanical side of this thesis, notably for the definition and the design of the prototype. Thank you to him and his team, my period in Munich was really nice and fun (one of my best souvenirs). I hope I will meet them again soon. Again, "Danke!".

Thank you also to Herve Legay from Thales Alenia Space, who was the first one I met when I was applying for the adventure. The meetings we had together were helpful to go in a good direction and upon this, it was also really nice to meet at some events like the REVOLVE week. I take this chance to also make a warm thank you to the people from Thales Alenia Space who were welcoming and nice (I still have some kilos from the Epiphanie of 2019). I think notably of Etienne, Ségolène, Jean-Philippe, Eric, Fabienne...

Thierry Monédière from Université de Limoges and Alexandros Feredisis from University of Birmingham have accepted to be the reviewers of my thesis and I want to thank them for this. I appreciated the care they took to comment my work. I am honored that Marc Philippe Yves Desmulliez from Heriot Watt University has agreed to chair the jury for my viva. I am also grateful that Christine Letrou from Paris-Tech Sud accepted to be a member of my jury. They all made me feel comfortable to present my work and answer to their questions.

I have to make a special award for the best office mates to Laurent, Gilles, and Jérémy at IETR. Merci beaucoup to let me stay in this french Brittany office while I was bringing the sun inside!

To my future or actual doctor friends, I was really happy to share this time with you and I am sure that we will do something soon to celebrate! I think about the Ph.D. students from INSA Rennes: Vincent, Alexandre, Paul, Aurélie, Samara, Hassan, Jean-Claude, Guillaume... from the REVOLVE project: Louis, Florian, Petros, Thomas, Andreas, and Haris... from Heriot University: Victoria, Rahil...Paul and Aurélie, maybe it is not even enough.

To my old and new friends from France and Norway, I am very glad that you are part of my life. I hope I could be the same support that you have been for me. "Merci" or "Takk" to Pierre-Edouard, Simon, Céline, Alexandra, Cléa, Bernard, Carl Ulrik, Luc to make me laugh when it is necessary.

Finally, last but not least I want to thank: my parents Jean-Marc and Marie-Christine, my sister Lauren and my grandmother Monique. I could say a lot of things but the best summary is: "On est une petite tribu mais au moins elle roule bien".

Abstract

In the frame of the european project Horizon 2020 named REVOLVE project initiated by Thales Alenia Space, Heriot Watt University, Large Space Structures, and Institut d'Electronique et des Technologies du numéRique, this Ph.D. investigates a new Reconfigurable Reflectarray Antenna (*RRA*) for Space applications. This work proposes a concept based on reflectarray antennas and mechanical reconfiguration. The distance between the ground plane and the metallic elements printed on the higher panel (noted h) is modified to control their reflected phase and therefore, change the radiation pattern provided by the antenna. This distance is tuned by modifying the shape of the ground plane thanks to actuators placed under it.

The first step is to analyze the impact of the distance h on the reflected phase of the cells. The design process of the *RRA* needs to be clearly defined to identify the parameters to take into account to ensure good performance of the antenna. The main issue is to minimize the number of actuators and the magnitude of the ground plane deformation while ensuring good RF and payload performance.

In the first instance, the methodology is defined considering an ideal control of the deformation and so, of the distance h . It is then applied on a sample of a two-configuration *RRA* and discussed while introducing one by one realistic constraint (number of actuators, material behavior...) for the control of the ground plane shape.

The design methodology is then extended over a 2D array sample composed by 21x21 cells which has to provide two ideal radiation patterns. The design methodology identified is then tested through the manufacturing and the measurements of a prototype. This developed breadboard has been assembled and tested at Large Space Structures and at IETR. Indeed, two series of tests are carried out. The first one is mechanical and aims to validate the prediction of the ground plane shape using Ansys Mechanical software for each configuration. The second series of tests deals with the RF measurements with the objective to assess predictions provided by the semi-analytical and fullwave analysis for both coverages.

The validation of the mechanical model has been done using photogrammetry to evaluate the control and the prediction of the ground plane shape. Considering the

complexity of the breadboard and the state-of-art, the results obtained are acceptable and show the repeatability capability of the deformation which is mandatory for a RRA. Once the control of the deformation has been validated, the antenna has been measured in the anechoic chamber.

The RF measurements (cf. Figure 1) show an acceptable correlation between the normalized predicted and measured radiation patterns for the first configuration. Nevertheless, it presents a big directivity loss explained notably by the non-optimal ground plane deformation due to the layout error made during the design process.

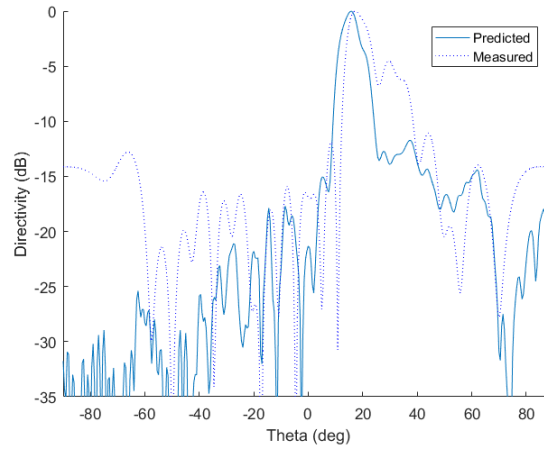


FIGURE 1: Normalized field at $f=12.85\text{GHz}$, Cut-plane $\Phi=90^\circ$.

Résumé

Dans le cadre du projet européen Horizon 2020 intitulé REVOLVE initié par Thales Alenia Space, Heriot Watt University, Large Space Structures, et l'Institut d'Electronique et des Technologies du numéRique, cette thèse s'intéresse à un nouveau concept d'antennes réseaux réflecteurs (*RRA*) reconfigurables pour des applications spatiales.

Le concept retenu suite à l'état de l'art est un réseau réflecteur reconfigurable mécaniquement. La modification du diagramme de rayonnement de l'antenne se fait en contrôlant la distance entre le plan de masse et les cellules imprimées (notée h) sur le réseau. Cette distance est modifiée à l'aide d'actionneurs placés sous le plan de masse pour le déformer.

Une fois le concept défini, la première étape consiste en l'analyse de l'impact de la distance h sur la phase réfléchie des cellules afin de mieux comprendre leur comportement. L'analyse de ces résultats permet alors d'identifier un couple (distance h ; phase réfléchie) pour la cellule et d'utiliser ces informations pour mettre en place une méthodologie de conception du réseau réflecteur. Cette procédure a pour but de fournir une sélection optimale des éléments rayonnants constituant le panneau à une fréquence donnée qui, associée à des déformations de plan de masse, produit les configurations souhaitées.

Trois étapes majeures sont identifiées afin de proposer une méthodologie de conception du *RRA* avec plan de masse flexible. Dans un premier temps, elle est définie en utilisant le cas d'un réseau linéaire à deux configurations de diagramme de rayonnement en considérant un contrôle idéal de la déformation et donc, de la distance h . Des contraintes plus réalistes relatives au contrôle de la forme du plan de masse (nombre d'actionneurs, comportement du matériau...) sont ensuite introduites une à une afin d'améliorer la méthodologie au fur et à mesure. Enfin, la troisième étape consiste dans l'extension de la méthodologie à un réseau 2D. Elle est ensuite testée à l'aide d'un prototype.

Les antennes réseau réflecteurs et la reconfiguration mécanique

Les réseaux réflecteurs et les éléments réfléchissants

Du fait de l'essor du marché des télécommunications, les antennes doivent être de plus en plus performantes tout en minimisant leurs coûts de fabrication. Ainsi, de nombreuses études ont été menées sur les antennes réflecteurs (paraboliques, formés...) ou encore les réseaux d'antennes. Etant donné que chacune de ces technologies présente des avantages et des inconvénients, un nouveau type d'antennes hybrides a été développé: les réseaux réflecteurs.

Les réseaux réflecteurs (RR) consistent en un panneau illuminé par une source sur lequel sont imprimés des motifs métalliques. On appelle cellules réfléchissantes du RR l'ensemble composé du motif métallique, du substrat sur lequel il est imprimé et du plan de masse situé en face arrière. Celles-ci réfléchissent l'onde incidente avec une phase particulière ce qui permet de produire la couverture souhaitée. Les réseaux réflecteurs sont donc compacts, peu chers, simples à fabriquer et légers tout en ayant des performances égales aux réseaux d'antennes et aux réflecteurs. La Figure 2 présente un exemple de réseau réflecteur.

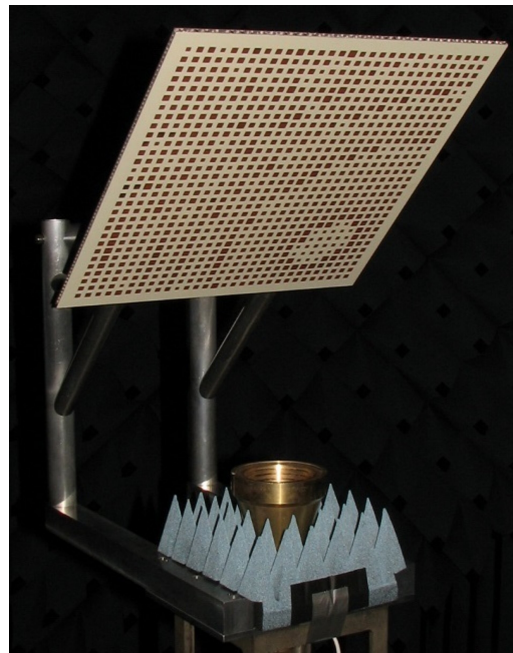


FIGURE 2: Exemple d'un réseau réflecteur, source: www.esa.int.

Les réseaux réflecteurs ont été étudiés pour répondre à de nombreuses applications spatiales notamment grâce à leur compacité et à leur surface plane. Parmi elles, les antennes à large envergure (cf. Figure 3), ou les antennes gonflables (cf. Figure 4).

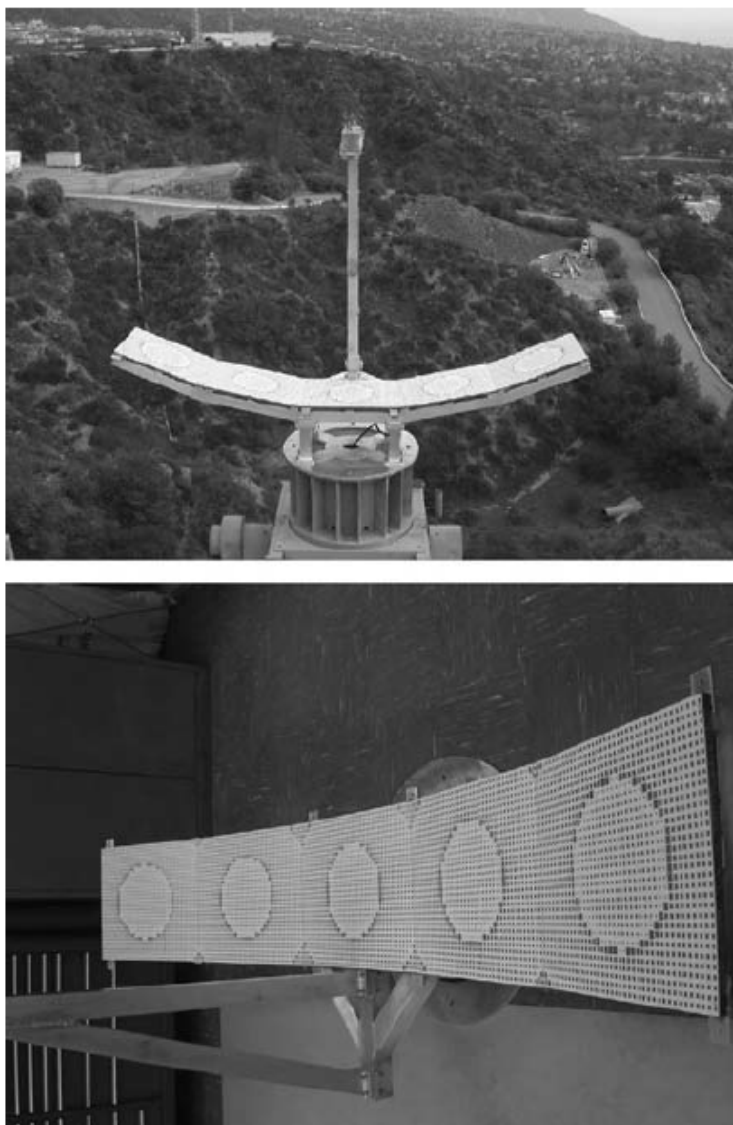


FIGURE 3: Photos de l'antenne réseau réflecteur à large envergure (2m x 0.5m) de la NASA-JPL [1].

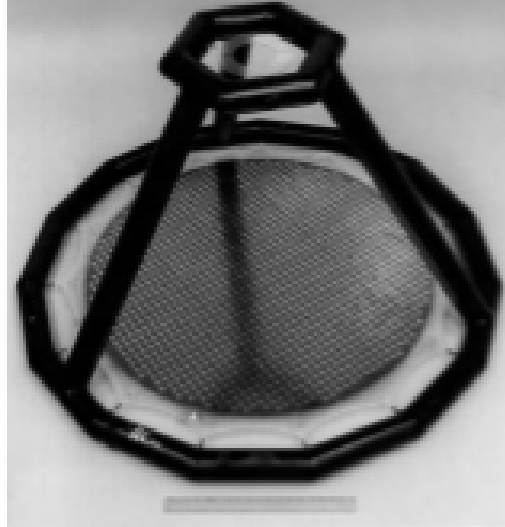


FIGURE 4: X-band 1-m réseau réflecteur gonflable [1].

Néanmoins, l'utilisation des *RRA* présente deux inconvénients majeurs: leur largeur de bande réduite et leurs performances. Ceux-ci dépendent des éléments rayonnants utilisés (limitations notamment en fréquence).

La découverte des cellules Phoenix [2] a permis de palier certaines de ces limitations notamment car elles peuvent produire des phases entre 0° et 360° grâce à une variation douce de leur géométrie tout en présentant une dispersion fréquentielle faible. Les capacités des cellules Phoenix de premier ordre sont néanmoins limitées du fait de leur unique paramètre variable. Les cellules Phoenix du second ordre ont donc été choisies pour être utilisées dans la méthodologie de conception du *RRA* mécaniquement reconfigurable. En effet, elles présentent de bonnes caractéristiques et l'utilisation d'un ordre supérieur permet une plus grande flexibilité pour le contrôle des caractéristiques de réflexion de la cellule.

Reconfiguration des antennes

De nombreuses études ont voulu tirer avantages des caractéristiques prometteuses des réseaux réflecteurs tout en permettant une modification en-orbite de la couverture réalisée par l'antenne. Ainsi, en s'inspirant des méthodes de reconfiguration déjà existantes telles que: l'électrique (Varactor [3–8], diodes PIN [9–20], and RF-MEMs [21–26]), l'optique (Photoconductrice [27–31]), la mécanique (par modification de la structure de l'antenne [32–34]), ou par changement de caractéristiques de matériau (Ferrites [35, 36] et crystal liquide [37, 38]), le concept

d'un réseau réflecteur reconfigurable mécaniquement par modification de la forme du plan de masse a été imaginé. En effet, la reconfiguration mécanique est préférée dans cette thèse car elle permet de s'abstenir de l'utilisation d'un nombre important d'éléments de commutation qui rendent le système plus complexe et plus cher.

Le réseau réflecteur à plan de masse flexible présenté dans cette thèse est basé sur des méthodes de reconfiguration appliquées aux réflecteurs simples [39] ou de compensation de l'erreur de forme d'une antenne [40]. Ainsi, pour chaque cellule du panneau, sa distance au plan de masse est modifiée par déformation mécanique de ce dernier afin de faire varier la phase qu'elle produit. La modification de la phase produite par chacune des cellules engendre une modification de la couverture réalisée par l'antenne. La Figure 5 illustre ce concept à l'échelle de la cellule.

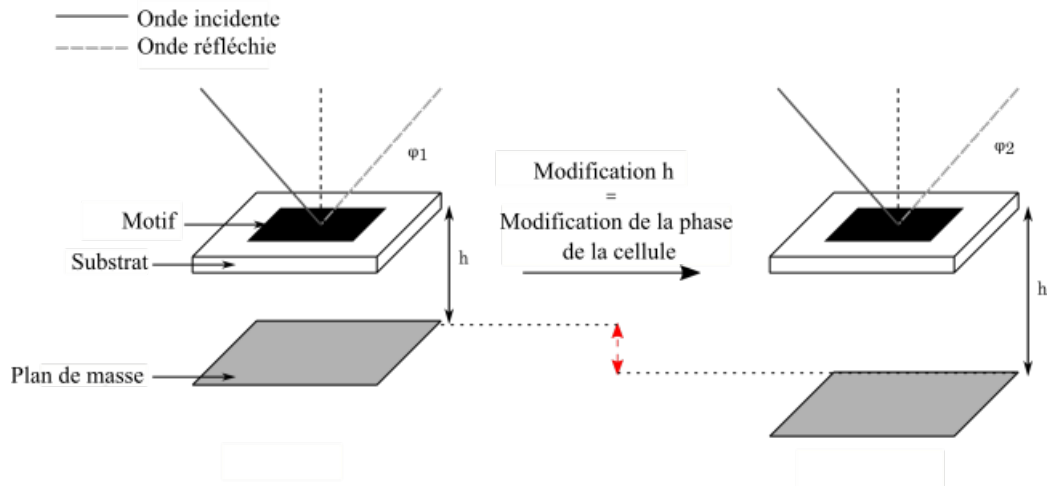


FIGURE 5: Vue de principe du concept à l'échelle d'une cellule.

Le concept à l'échelle du panneau est ensuite présenté Figure 6.

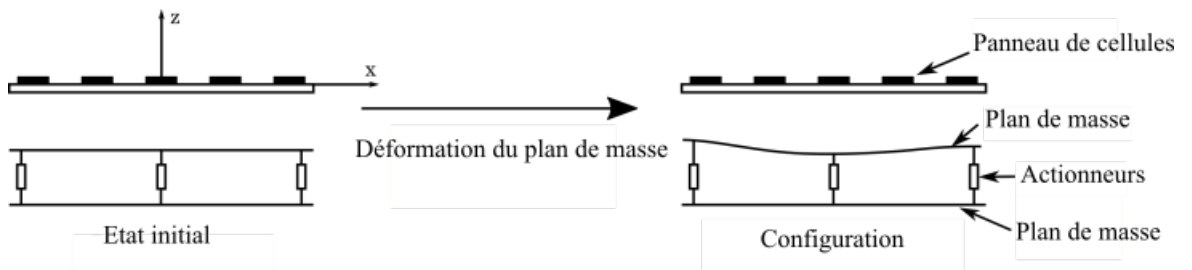


FIGURE 6: Concept proposé.

Les précédentes études réalisées, notamment sur le réflecteur reconfigurable [39], soulignent la difficulté de fournir simultanément d'excellentes performances RF, structurelles et mécaniques. En effet, étant donné que le contrôle du plan de masse se fait à l'aide d'actionneurs leur nombre et leur précision sont importants pour réaliser au mieux une déformation souhaitée. L'augmentation du nombre d'actionneurs augmente la masse totale de l'antenne, sa complexité et sa taille, ce qui va à l'encontre des objectifs structurels recherchés mais devrait permettre d'atteindre avec plus de précision la déformation voulue. De plus, l'envergure des déformations, l'étirement de la membrane entre deux cellules sont contraints par les caractéristiques du matériau utilisé. Ainsi, ce problème a de multiple objectifs inter-dépendants et parfois contraires.

Avant de définir une méthodologie de conception du réseau réflecteur reconfigurable à plan de masse flexible, il est nécessaire d'étudier le comportement des cellules en fonction de la distance h .

Etude des éléments réfléchissants

Le Chapitre 2 présente les modèles utilisés pour obtenir la phase produite d'une géométrie de cellule donnée à différentes valeurs de h pour une fréquence donnée. Ces modèles ont été développés dans l'optique de créer une base de données de cellules en réduisant le temps de calcul par rapport à une série de simulations fullwave. Pour cela, certaines hypothèses ont été adoptées notamment celle d'un plan de masse localement plan en dessous de chacune des cellules composant le panneau.

L'impact de la distance h sur la phase produite des cellules considérées est ensuite analysé. On remarque alors qu'il existe différents comportements de cellules qui sont plus ou moins intéressants en fonction de l'application souhaitée. En effet, trois types sont identifiés. Le premier type de cellules présente majoritairement une sensibilité faible aux variations de distance h en termes de variation de phase. Néanmoins, sur une faible portion de valeurs de h , les cellules deviennent extrêmement sensibles.

Le deuxième type de cellules réunit celles dont la variation de phase produite est modérée par rapport à la variation de hauteur. Leur comportement représente un

avantage puisqu'elles sont capables de produire une variation de phase produite importante pour une variation faible de h .

Le troisième type de cellules présente une variation quasi-linéaire de la phase produite par rapport à h . A l'échelle du panneau, cela peut être problématique puisque des différences de distances h entre deux cellules consécutives peuvent apparaître. Ces sauts ne pouvant pas être produits dans la réalité, cela engendrera forcément des erreurs de phase et donc une détérioration des performances RF.

Définition d'une méthodologie de conception

L'analyse de l'impact de la distance h sur la phase produite d'une cellule est le point de départ de l'identification d'une méthodologie de conception pour le *RRA* à plan de masse flexible. Néanmoins, malgré les informations fournies, il est difficile de définir l'état initial du *RRA* puisque même le nombre de configurations, le nombre d'actionneurs et leur distribution ne sont pas connus. Ainsi, il a été décidé d'identifier une première méthodologie de conception pour un cas particulier devant fournir deux configurations pour une distribution uniforme des actionneurs.

Cette première méthodologie est appliquée dans un premier temps à un réseau linéaire composé de 21 cellules comme le montre la Figure 7. Ce réseau est extrait d'un cas 2D utilisé par la suite lors de l'extension de la méthodologie et de sa validation à l'aide d'un prototype.

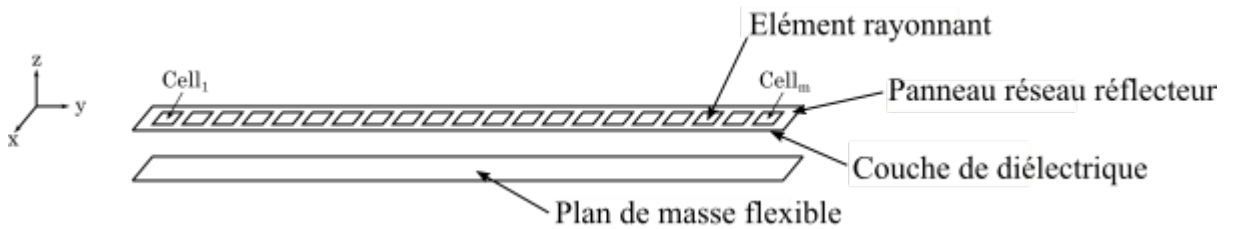


FIGURE 7: Configuration du réseau linéaire.

Les couvertures attendues pour les deux configurations à fournir, notées S_1 et S_2 , sont présentées Figure 8. S_1 consiste en un faisceau dépointé de 17° par rapport à la direction normale au réseau. Tandis que, S_2 correspond à un faisceau présentant le même dépointage mais élargi grâce à l'introduction d'une loi de phase non-linéaire dans le plan $0yz$.

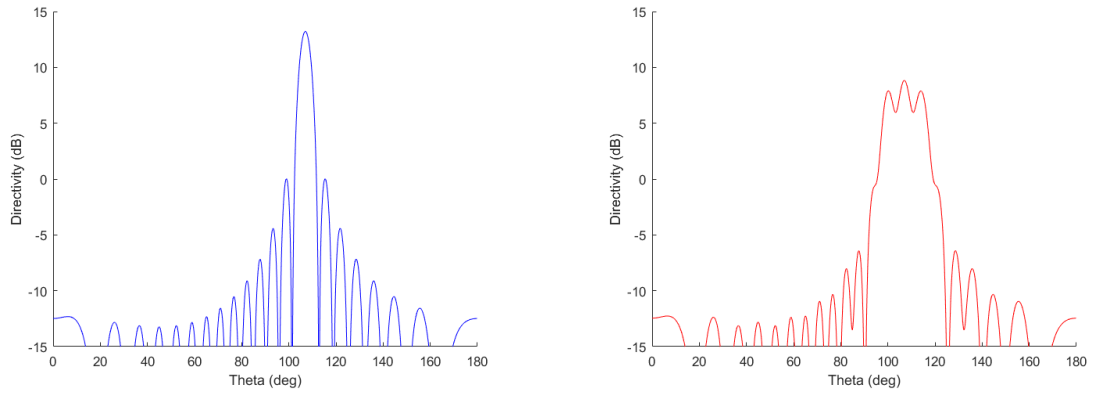


FIGURE 8: Diagrammes de directivité idéaux pour S_1 (*gauche*) et pour S_2 (*droite*).

Méthodologie développée pour un réseau linéaire

Une première proposition de méthodologie de conception du réseau linéaire est faite en considérant un contrôle et une déformation du plan de masse idéaux. Ainsi, le plan de masse est discrétisé selon le nombre de cellules et est considéré localement plan sous chacune d'entre elles. Ensuite, cette méthodologie est appliquée à un cas test de réseau linéaire extrait d'un réseau 2D. La solution trouvée n'est néanmoins pas réalisable en raison des hypothèses prises sur le nombre d'actionneurs et la déformation du plan de masse. Ainsi, la méthodologie est donc ensuite éprouvée en insérant au fur et à mesure de nouvelles contraintes notamment sur la déformation du plan de masse. Ces nouvelles contraintes concernent notamment la distribution et le nombre d'actionneurs du fait qu'elles ont un impact direct sur le contrôle de la forme du plan de masse et par conséquent sur le diagramme de rayonnement produit.

Suite à cela, une seconde méthodologie est proposée en considérant les informations obtenues par l'introduction de ces dites contraintes et est ensuite appliquée au même cas test.

Enfin, une dernière amélioration de la méthodologie est proposée. Celle-ci inclut un modèle de prédiction de la déformation du plan de masse sous le logiciel Ansys Mechanical. Le profil de la déformation obtenue par simulation est utilisé pour la sélection des cellules afin de minimiser l'erreur moyenne entre les déformations idéales et réelles. Une fois cette dernière modification de la méthodologie prise en compte, un layout est obtenu. Celui-ci est alors testé avec le plan de masse

déformé simulé précédemment, par simulation fullwave sur le logiciel *HFSS*. A ce stade, seule une onde plane est considérée. La Figure 9 présente la sélection des cellules faite le long du panneau pour l'exemple étudié ici.

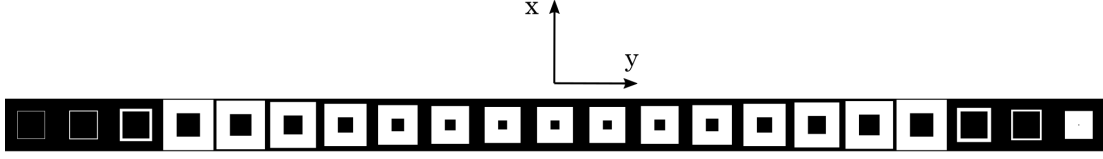


FIGURE 9: Sélection des cellules composant le réseau linéaire étudié.

La Figure 10 présente les déformations idéales, linéaires et prédites associées à S_1 et S_2 respectivement appelée *ideal*, *linear*, *Ansys*.

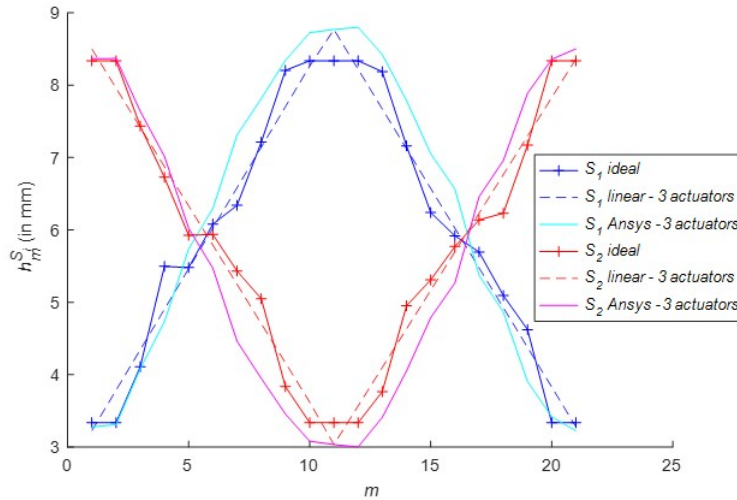


FIGURE 10: Déformations idéales, linéaires et prédites pour S_1 et S_2 .

La Figure 11 illustre les résultats obtenus pour la validation de la méthodologie. Il est important de noter que *ideal*, *HFSS*, *Provided* correspondent respectivement aux diagrammes de directivité obtenu dans le cas idéal, obtenu par simulation fullwave, et prédit avec le code Matlab mis en place. Ce dernier considère la modélisation des cellules, les couvertures idéales et les hauteurs h pour chaque cellule pour calculer la phase produite par la cellule.

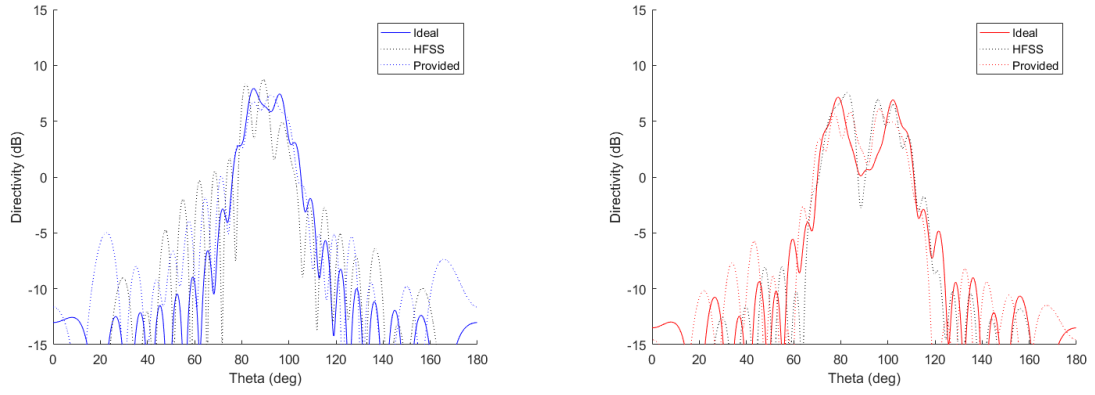


FIGURE 11: Résultat de la validation de la méthodologie pour les deux couvertures attendues S_1 (gauche) et pour S_2 (droite).

Les résultats des simulations fullwave montrent une bonne corrélation entre les résultats prédits et la simulations fullwave, ce qui permet d'envisager une extension de la méthodologie a un cas 2D.

Extension de la méthodologie à un réseau 2D

La méthodologie est ensuite étendue à un réseau 2D composé de 21x21 cellules. La Figure 12 illustre la configuration d'antenne considérée et les couvertures recherchées sont présentées Figure 13.

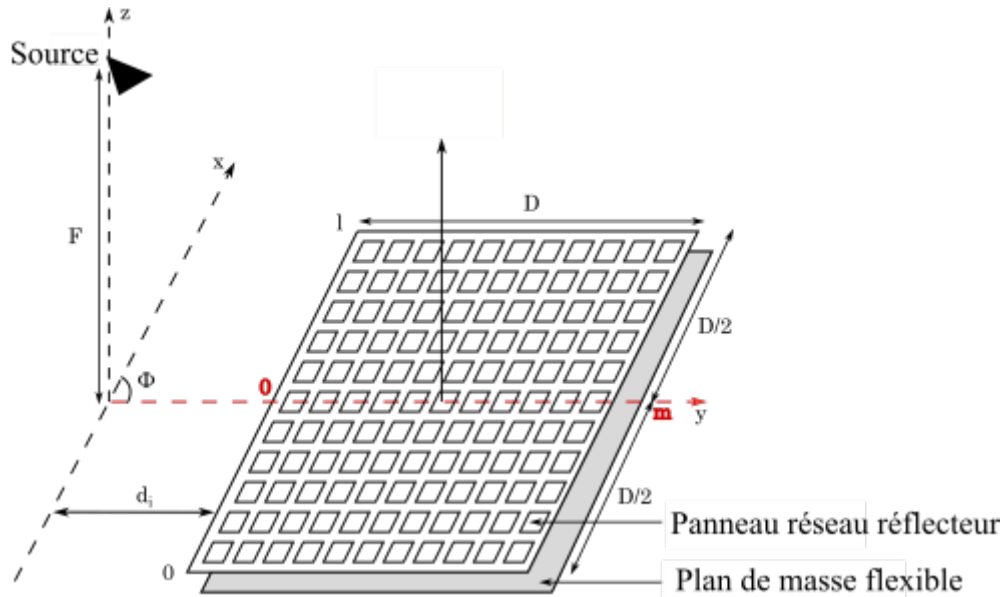


FIGURE 12: Configuration de l'antenne.

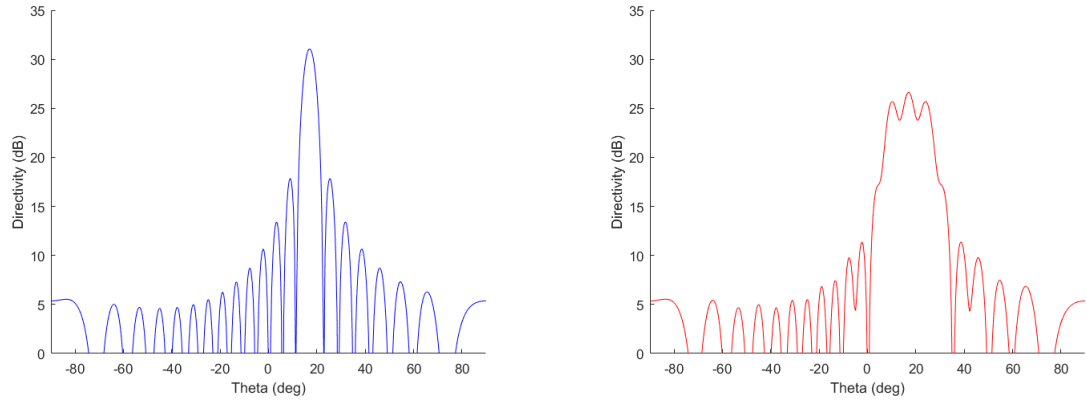


FIGURE 13: Diagrammes de directivité idéaux S_1 (*gauche*) et pour S_2 (*droite*).

Afin de simplifier l'extension de la méthodologie à un cas 2D, notre proposition a été de considérer le panneau 2D comme étant 21 réseaux linéaires mis côte à côte. Chacun de ces réseaux devant fournir les phases produites souhaitées en imposant les mêmes déformations que pour le réseau linéaire développé précédemment. Cela permet d'avoir une configuration d'antenne déjà fixe en termes de distribution et nombre d'actionneurs ainsi que de déformations à réaliser. Il suffit alors de trouver les cellules qui, pour chaque location sur le réseau, produisent la phase souhaitée en fonction de la distance au plan de masse qui lui est appliquée. Il est important de noter, que le modèle de prédiction de la forme du plan de masse a dû être modifié afin d'être étendu au réseau 2D. La Figure 14 présente la distribution cellulaire qui découle de la méthodologie mise en place.

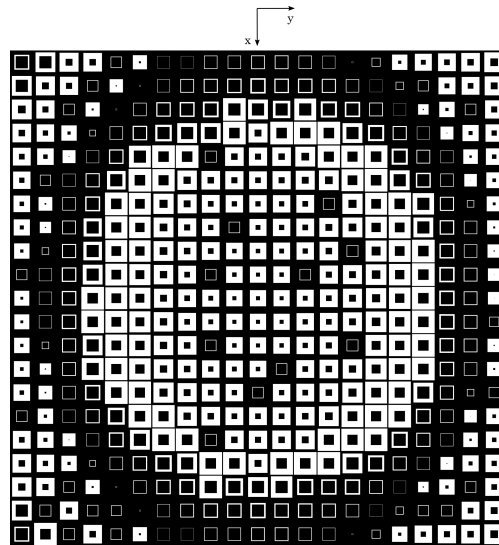


FIGURE 14: Distribution des cellules sur le réseau 2D.

En utilisant les déformations prédites ainsi que la base de données de cellules, et les phases à réaliser, les diagrammes de directivité obtenus par calcul du facteur de réseau, notés *predicted*, sont présentés Figure 15.

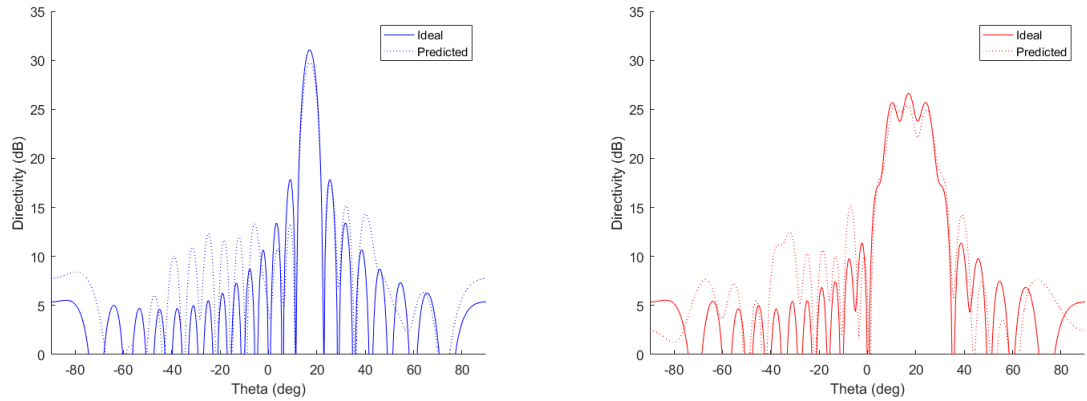


FIGURE 15: Diagrammes de directivité idéaux et prédits pour S_1 (*gauche*) et pour S_2 (*droit*).

Les diagrammes de directivité présentés Figure 15 présentent une bonne corrélation entre l'idéal et le prédit, et cela pour les deux couvertures. Au vue de ces résultats et de ceux obtenus avec la simulation fullwave du réseau linéaire, il semble intéressant de développer un prototype qui permettra de prouver le concept proposé.

Fabrication et test d'un prototype

Remarques préliminaires

La fabrication et l'assemblage du prototype se sont faits dans les locaux de *LSS* à Eching en Allemagne, tandis que les tests ont été réalisés à Rennes au sein de l'*IETR*. Une erreur dans le développement de la méthodologie a été remarquée alors que le panneau de cellules avait déjà été fabriqué et qu'il n'était plus possible d'en recommander un autre au vue des délais. Ainsi, étant donné que le concept repose sur le principe d'une possible reconfiguration, l'idée a été de compenser l'erreur de la sélection des cellules du mieux possible par la déformation du plan de masse. Néanmoins une autre difficulté s'ajoute à cela, la distribution des actionneurs et leur nombre sont fixes ce qui limite les possibilités de déformation.

La Figure 16 illustre la sélection des cellules du prototype.

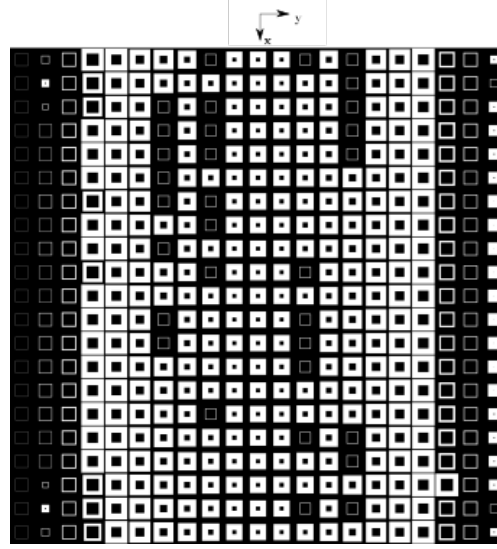


FIGURE 16: Cells distribution for the 2D panel.

Les diagrammes de rayonnement prédits sont présentés Figure 17.

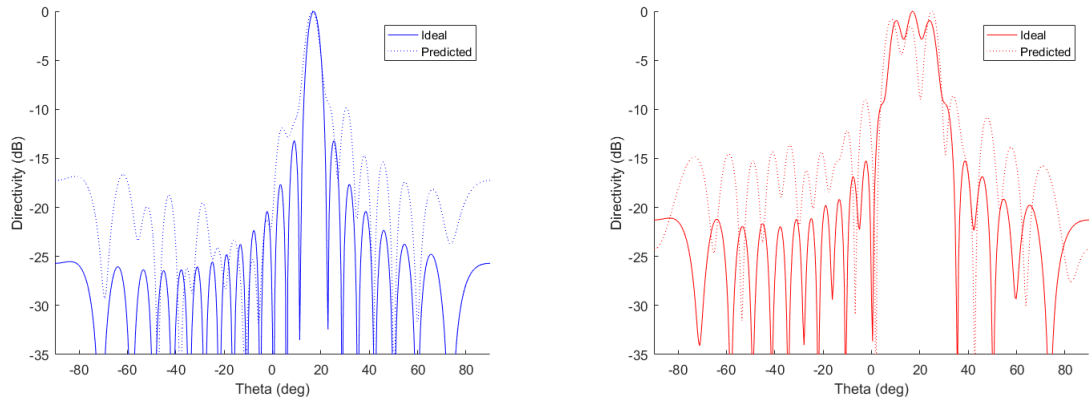


FIGURE 17: Diagrammes de rayonnement, Plan de coupe $\Phi = 90^\circ$ pour S_1 (gauche), et S_2 (droite) en considérant des déformations prédites.

La couverture S_1 semble être bien respectée tandis que S_2 présente une corrélation entre l'idéal et le prédit assez mauvaise. Par conséquent, il a été décidé de s'intéresser uniquement aux résultats RF de S_1 .

Fabrication et test du prototype

La fabrication doit prendre en compte différentes contraintes notamment en termes d'intégration de chacun des éléments vis-à-vis des autres. Le parallélisme et le centrage de certaines parties sont essentiels, comme par exemple l'alignement du panneau de cellules avec la membrane et les actionneurs.

La Figure 18 illustre les différentes parties du prototype à assembler.

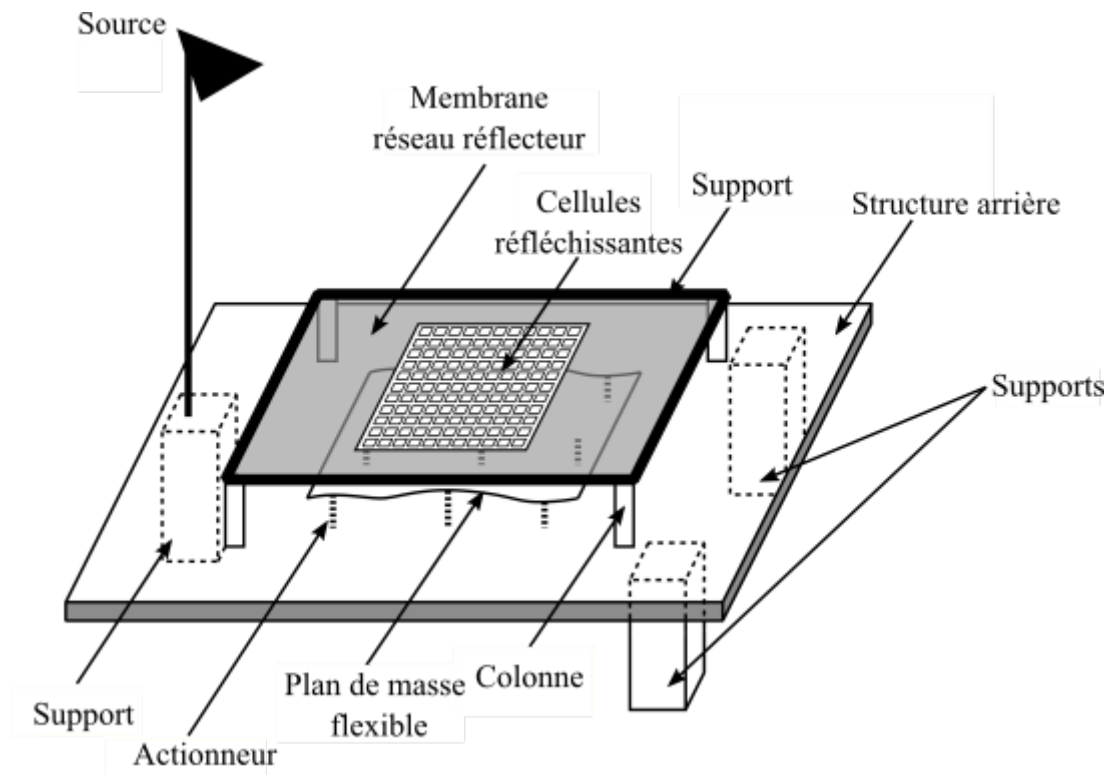


FIGURE 18: Schéma de la structure.

Différents tests sont réalisés afin de valider le modèle de déformation du plan de masse (tests de photogrammétrie, cf. Figure 19) et celui des performances RF.

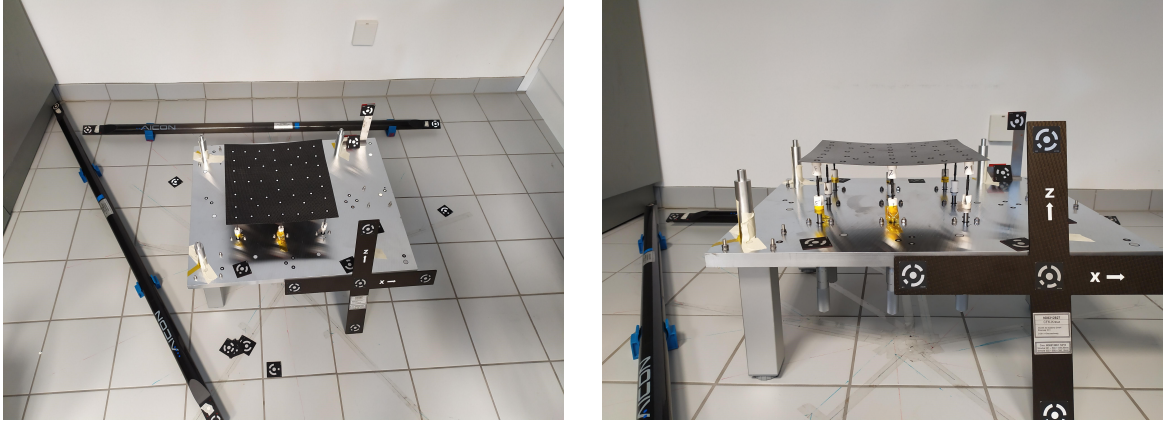
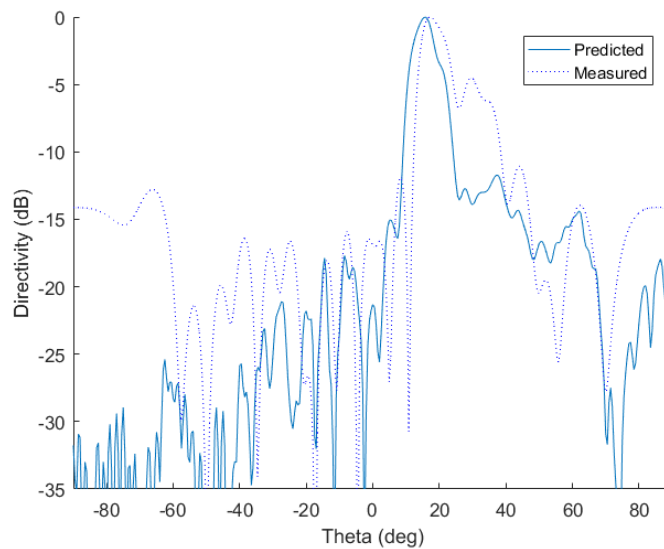


FIGURE 19: Mise en place des tests de photogrammétrie.

On remarque que les résultats de photogrammétrie sont cohérents avec ceux présentés dans la littérature notamment pour un réflecteur déformable de diamètre 500mm utilisant 19 actionneurs. Ainsi, la déformation mécanique et sa prédiction semblent acceptables à ce niveau.

Une fois la validation mécanique réalisée, l'antenne est testée à l'*IETR*. Les résultats sont ensuite comparés avec les idéaux et les prédits.

La Figure 20 présente les résultats obtenus. A la fréquence de $f = 12.85GHz$, la directivité prédite était de 26.5 dB quand celle obtenue est de 20.2 dB.

FIGURE 20: Champ normalisé $f=12.85$ GHz, plan de coupe $\Phi=90^\circ$.

On remarque ainsi que malgré une corrélation acceptable du profil de diagramme prédit par l'outil développé, il y a une perte de directivité importante. Cette perte peut être en partie explicable par l'hypothèse de la planarité locale du plan de masse sous chaque cellule prise pour la base de donnée, de l'onde incidente non considérée dans cette même base de données et des couplages qui peuvent exister entre les cellules. Néanmoins, étant donné les résultats obtenus par simulation fullwave du réseau linéaire, cela ne semble à ce stade ne pas être suffisant pour justifier une telle perte.

Le concept est donc validé partiellement car d'autres investigations doivent être réalisées afin de permettre de mettre réellement en valeur l'intérêt d'une telle antenne. De plus, on peut également remarquer que sa complexité de mise en place est relativement élevée. Néanmoins, cela peut-être palié par le développement d'un outil d'optimisation plus poussé que ce qui est présenté comme première approche dans cette thèse. Certaines des études faites pour la mise en place de ce concept et notamment pour l'application à un cas considérant 3 configurations sont présentées en Annexe.

List of Figures

1	Normalized field at $f=12.85\text{GHz}$, Cut-plane $\Phi=90^\circ$	vii
2	Exemple d'un réseau réflecteur, source: www.esa.int	ix
3	Photos de l'antenne réseau réflecteur à large envergure (2m x 0.5m) de la NASA-JPL [1].	x
4	X-band 1-m réseau réflecteur gonflable [1].	xi
5	Vue de principe du concept à l'échelle d'une cellule.	xii
6	Concept proposé.	xii
7	Configuration du réseau linéaire.	xiv
8	Diagrammes de directivité idéaux pour S_1 (<i>gauche</i>) et pour S_2 (<i>droite</i>).	xv
9	Sélection des cellules composant le réseau linéaire étudié.	xvi
10	Déformations idéales, linéaires et prédites pour S_1 et S_2	xvi
11	Résultat de la validation de la méthodologie pour les deux couver- tures attendues S_1 (<i>gauche</i>) et pour S_2 (<i>droite</i>).	xvii
12	Configuration de l'antenne.	xvii
13	Diagrammes de directivité idéaux S_1 (<i>gauche</i>) et pour S_2 (<i>droite</i>).	xviii
14	Distribution des cellules sur le réseau 2D.	xviii
15	Diagrammes de directivité idéaux et prédits pour S_1 (<i>gauche</i>) et pour S_2 (<i>droit</i>).	xix
16	Cells distribution for the 2D panel.	xx
17	Diagrammes de rayonnement, Plan de coupe $\Phi = 90^\circ$ pour S_1 (<i>gauche</i>), et S_2 (<i>droite</i>) en considérant des déformations prédites.	xx
18	Schéma de la structure.	xxi
19	Mise en place des tests de photogrammétrie.	xxii
20	Champ normalisé $f=12.85\text{ GHz}$, plan de coupe $\Phi=90^\circ$	xxii
1.1	Principle of a reflectarray antenna.	6
1.2	Geometrical configuration for some reflector systems.	7
1.3	Example of a shaped reflector with large aperture [51].	8
1.4	Principle of a parabolic reflector.	10
1.5	Example of a flat reflectarray antenna (source: www.esa.int).	10
1.6	Shape comparison between a reflectarray and a simple reflector to produce a directive beam.	11
1.7	Shape comparison between a reflectarray and a shaped reflector to produce a shaped beam.	11
1.8	Representation of a multi-layer patch: (left) two layers and (right) three layers.	13

1.9	First Phoenix cycle [2].	14
1.10	Phoenix cycle for a first-order cell capacitive (<i>top</i>), inductive (<i>bottom</i>).	14
1.11	Capacitive (<i>left</i>), inductive (<i>right</i>) second-order Phoenix cells [88].	15
1.12	Radiating paths between the feed and the <i>RA</i> panel.	16
1.13	(Right) Radiation with a steering - (left) Radiation in the broadside direction (array axis).	17
1.14	The AstroMesh in deployed configuration [89].	18
1.15	6m configuration for deployable <i>RA</i> (<i>left</i>) and 10 m configuration for deployable <i>RA</i> (<i>right</i>).	19
1.16	<i>RA</i> parameters.	19
1.17	Photos of the NASA-JPL very large aperture <i>RA</i> 2m x 0.5m [1].	20
1.18	X-band 1-m Inflatable Reflectarray.	21
1.19	Ka-band 3-m Inflatable Reflectarray [99].	22
1.20	Principle schema of the "movie screen" reflectarray antenna [94].	23
1.21	Reconfigurable reflectarray by modification of its configuration.	27
1.22	Reflector antenna with reconfiguration capabilities thanks to actuators.	28
1.23	3D view of a selectable sub-reflectarray (right), versus a selectable dish system (left).	29
1.24	Concept for rollable reflectarray/transmittarray antenna.	30
1.25	Schema of a piezoelectric actuator controlled by phase shifter [121].	31
1.26	Concept for <i>RA</i> used for distortion compensation [124].	32
1.27	Schematic view of the concept at the cell level.	34
1.28	Concept proposal.	34
1.29	Structure of the radiating element.	35
2.1	Structure of the radiating element.	39
2.2	Representation of the Ansys HFSS Setup for the reflecting element structure. Note: PerH (Perfect Magnetic Boundary), PerE (Perfect Electric Boundary).	40
2.3	EC of the radiating element with S matrix.	41
2.4	Phoenix cell simulation setup in Ansys HFSS.	43
2.5	Phoenix cells geometrical parameter for first, second and third order (left to right) capacitive (bottom) and inductive (top).	43
2.6	Capacitive 2 nd order Phoenix cell: $P = 11.7mm$, $C_1 = 4.4mm$, $C_2 = 3.8mm$ at $f = 12.5GHz$	44
2.7	Inductive 2 nd order Phoenix cell: $P = 11.7mm$, $C_1 = 4.4mm$, $C_2 = 3.8mm$ at $f = 12.5GHz$	45
2.8	Geometrical parameters of the reflecting elements.	46
2.9	EC of the radiating element without substrate.	47
2.10	Capacitive 2 nd order Phoenix cells: $P = \frac{\lambda_0}{2} = 11.7mm$	48
2.11	Impact of an error of position on the phase response versus the reference distance.	50
2.12	Impact of the frequency on the phase for $Cell_1$	52
2.13	Impact of the frequency on the phase for $Cell_2$	52

2.14	Impact of the frequency on the phase for $Cell_3$.	53
2.15	Impact of h on the frequency dispersion.	54
3.1	Concept of the two-configuration RRA .	59
3.2	Linear array configuration.	60
3.3	EC model of the cell without substrate.	61
3.4	Antenna configuration.	65
3.5	Ideal directivity patterns for S_1 (<i>left</i>) and for S_2 (<i>right</i>).	66
3.6	Introduced phase law for S_2 .	68
3.7	Phases that need to be produced by the cells at $x=0$.	68
3.8	Admittances $b_m^{S_1}$, $b_m^{S_2}$, and b_m^{ave} for the 1D panel considering $h = \frac{\lambda_0}{4}$.	69
3.9	Average phase along the panel.	70
3.10	First cells selection for the linear array.	71
3.11	Ideal and produced average phase along the panel.	71
3.12	Ideal deformations associated with S_1 and S_2 .	72
3.13	Ideal deformations associated with S_1 and S_2 .	73
3.14	Ideal phase distribution over the panel for S_1 (<i>left</i>) and for S_2 (<i>right</i>).	74
3.15	Homogeneous and adjusted actuators' distribution.	76
3.16	Application of the actuators' action on the ground plane considering the RRA panel.	78
3.17	Ideal and linear approximation of the deformations for S_1 and S_2 for the case 1 (<i>left</i>) and the case 2 (<i>right</i>).	78
3.18	Directivity patterns for the linear array for the case with 5 actuators uniformly distributed for S_1 (<i>left</i>) and for S_2 (<i>right</i>).	79
3.19	Directivity patterns for the linear array for the case with 3 actuators uniformly distributed for S_1 (<i>left</i>) and for S_2 (<i>right</i>).	79
3.20	Setup of the mechanical model.	81
3.21	Result of the mechanical model for S_1 .	81
3.22	Result of the mechanical model for S_2 .	81
3.23	Ideal, linear and predicted deformations for S_1 and S_2 .	82
3.24	Directivity patterns for S_1 (<i>left</i>) and for S_2 (<i>right</i>).	83
3.25	First cells distribution for the 1D panel after a second cell selection.	84
3.26	Directivity patterns for S_1 (<i>left</i>) and for S_2 (<i>right</i>) with the second layout.	84
3.27	Ideal phase laws with phase offsets.	85
3.28	Ideal, linear and predicted deformations for both coverages.	86
3.29	Selection of cells for the new layout.	87
3.30	Ideal and predicted directivity pattern for S_1 (<i>left</i>) and for S_2 (<i>right</i>).	87
3.31	Ideal and predicted directivity pattern for S_1 (<i>left</i>) and for S_2 (<i>right</i>) at 12.35 GHz.	88
3.32	2D Directivity patterns for S_1 , test case (<i>left</i>) and for S_2 (<i>right</i>) at 13.35 GHz.	88
3.33	Flowchart of the final design methodology for a linear array with a two-configuration capabilities.	89
3.34	Setup configuration of the HFSS simulation	90

3.35	Comparison between ideal, computed and full-wave simulations of the 1D directivity patterns obtained for S_1 (<i>left</i>) and for S_2 (<i>right</i>).	91
4.1	Antenna configuration.	96
4.2	Ideal directivity patterns, Cut-plane $\Phi = 90^\circ$ for S_1 (<i>left</i>) and for S_2 (<i>right</i>).	96
4.3	Distribution of the ideal cells phase response for S_1 (<i>left</i>) and for S_2 (<i>right</i>).	97
4.4	Representation of the interface between the surface and the actuators.	99
4.5	Boundary conditions of the ground plane shape prediction model for the 2D array.	99
4.6	Predicted ground plane shape for S_1 .	101
4.7	Predicted ground plane shape for S_2 .	101
4.8	Design of the 2D panel deduced using the predicted ground plane shapes.	102
4.9	Predicted directivity patterns obtained, Cut-plane $\Phi = 90^\circ$ for S_1 (<i>left</i>) and for S_2 (<i>right</i>).	103
4.10	Distribution of the average phase error for S_1 (<i>left</i>) and for S_2 (<i>right</i>).	103
4.11	Radiation patterns obtained for the ideal case of S_1 (<i>left</i>) and the predicted one (<i>right</i>).	104
4.12	Radiation patterns obtained for the ideal case of S_2 (<i>left</i>) and the predicted one (<i>right</i>).	104
4.13	Cells distribution for the 2D panel.	105
4.14	Scheme of the whole structure.	107
4.15	Ideal deformations for S_1 (<i>left</i>) and S_2 (<i>right</i>).	108
4.16	Ideal deformations for the lign n° 1, 11, and 21 extracted from the 2D panel for S_1 (<i>left</i>) and S_2 (<i>right</i>).	108
4.17	Ideal deformations considering the additional distance technique for S_1 (<i>left</i>) and for S_2 (<i>right</i>).	109
4.18	Simulation of the ground plane shape for S_1 , also called predicted deformation.	110
4.19	Simulation of the ground plane shape for S_2 , also called predicted deformation.	111
4.20	Radiation patterns, Cut-plane $\Phi = 90^\circ$ for S_1 (<i>left</i>), and S_2 (<i>right</i>) with the realistic deformations.	111
4.21	Radiation patterns obtained for the ideal case of S_1 (<i>left</i>) and the computed one (<i>right</i>).	112
4.22	Radiation patterns obtained for the ideal case of S_2 (<i>left</i>) and the computed one (<i>right</i>).	112
4.23	photo of the rear-structure with the actuators mounted.	114
4.24	photo of the rear-structure prepared for the photogrammetry tests.	115
4.25	Assembly process of the actuators, the membrane and their interfaces.	116
4.26	Assembly of the actuators, the membrane and their interfaces.	117
4.27	Photo of the ground plane assembly.	118
4.28	Assembly of the frame and the flexible ground plane.	119

4.29	Setup of the photogrammetry.	120
4.30	Photo of the antenna in the anechoic chamber.	122
4.31	Radiation pattern of the horn at $f=12.85$ GHz.	123
4.32	Predicted (u, v) pattern for S_1 at $f=12.85$ GHz.	123
4.33	Measured (u, v) pattern for S_1 at $f=12.85$ GHz.	124
4.34	Measured directivity for the whole frequency range.	125
4.35	Normalized field at $f=12.85$ GHz, Cut-plane $\Phi=90^\circ$	126
4.36	Normalized field at $f=12.35$ GHz, Cut-plane $\Phi=90^\circ$	126
4.37	Normalized field at $f=13.35$ GHz, Cut-plane $\Phi=90^\circ$	127
A.1	Phase laws that the cells along the panel have to produce for the three patterns (S_1 , S_2 , and S_3 at $f=12.2$ GHz).	134
A.2	Impact of the distance h on the reflected phase of the cells compos- ing the database.	135
A.3	Optimized ground deformation for S_1 , S_2 , and S_3 (cells are repre- sented by dots and actuators by stars).	137
A.4	Theoretical radiation patterns (desired and obtained ones) for S_1 at 12.2 GHz.	138
A.5	Theoretical radiation patterns (desired and obtained ones) for S_2 at 12.2 GHz.	138
A.6	Theoretical radiation patterns (desired and obtained ones) for S_3 at 12.2 GHz.	139
A.7	HFSS model (top view and side views for S_1).	140
A.8	HFSS radiation patterns and targeted ones for S_1 in the case of a plane incident wave.	140
A.9	HFSS radiation patterns and targeted ones for S_2 in the case of a plane incident wave.	141
A.10	HFSS radiation patterns and targeted ones for S_3 in the case of a plane incident wave.	141

List of Tables

2.1	Time consumption of each methodology	45
2.2	Impact of a position error on the phase response of a cell	50
2.3	Maximal frequency dispersion for $h \in [0; \frac{\lambda_0}{2}]$	54
3.1	Material characteristics of the flexible ground plane used for the Ansys Mechanical model.	77
3.2	Average error distance along the panel.	79
3.3	Displacements applied to the actuators taking the bottom of the substrate as a reference.	80
3.4	Displacements applied to the actuators for each configuration for the 2D panel.	86
4.1	Displacements applied to the actuators for each configuration for the 2D panel.	100
4.2	Displacements applied to the actuators for each configuration for the 2D panel	100
4.3	Displacements applied to the actuators for configuration S_1	110
4.4	Displacements applied to the actuators for configuration S_2	110
4.5	<i>RMS</i> computed for each photogrammetry test.	121
4.6	Predicted and measured directivities for coverages S_1 and S_2	125
A.1	Percentage of error in the radiation patterns.	139

Contents

Declaration statement	i
Acknowledgements	iv
Abstract	vi
Résumé	viii
List of Figures	xxiv
List of Tables	xxix
Contents	xxx
General introduction	1
1 Reflectarray antennas and reconfiguration	4
1.1 Introduction	5
1.2 Reflectarray antenna technology	5
1.2.1 Reflector antennas	6
1.2.2 Array antennas	8
1.2.3 Reflectarray antennas	9
1.2.3.1 Principle	9
1.2.3.2 Advantages and disadvantages of reflectarray antennas	12
1.2.3.3 Development of the radiating elements	12
1.2.3.4 Phase law definition	15
1.2.3.5 Few examples of applications	17
1.2.4 Conclusion	24
1.3 Existing reconfigurability concepts	24
1.3.1 Electrical reconfiguration	25
1.3.2 Optical reconfiguration	26
1.3.3 Material change reconfiguration	26
1.3.4 Mechanical reconfiguration of the radiation pattern	27
1.3.4.1 Re-shapeable reflector/reflectarray antennas	27
1.3.4.2 Selectable reflector/reflectarray antennas	29

1.3.4.3	Rollable reflectarray antenna	29
1.3.4.4	Motion of the ground plane	30
1.3.5	Conclusion on reconfiguration techniques	32
1.3.6	Multi-objective optimization	33
1.4	Reconfiguration concept proposal	33
1.4.1	Description	33
1.4.2	Study issues	35
1.5	Conclusion	36
2	Modeling and analysis of cells with tunable height	37
2.1	Introduction	38
2.2	Modeling tool	39
2.2.1	Objectives and hypothesis	39
2.2.2	Semi-analytical model	40
2.2.2.1	HFSS model	40
2.2.2.2	Equivalent electrical circuit model	41
2.2.3	Full-wave validation	42
2.2.3.1	Reflecting elements database	46
2.3	Impact of h on the reflected phase	47
2.4	Impact of an error on h	49
2.5	Impact of h on the frequency dispersion of the cells	51
2.6	Conclusion	55
3	Design methodology of a mechanically reconfigurable reflectarray with two configurations	57
3.1	Introduction	58
3.2	Objectives and constraints of a mechanically reconfigurable reflectarray	58
3.3	Methodology for a linear reflectarray	60
3.3.1	Development of the methodology	60
3.3.1.1	First cell selection	60
3.3.1.2	Identification of the ideal deformations	63
3.3.1.3	Reduction of the ideal deformations magnitude	64
3.3.2	Application case	65
3.3.2.1	Antenna characteristics	65
3.3.2.2	Phase law specification	66
3.3.2.3	Identification of the phase introduced by the cells	66
3.3.2.4	Computation of the average admittance along the panel	69
3.3.2.5	Computation of the average phase	70
3.3.2.6	First selection of cells	70
3.3.2.7	Identification of the ideal deformation	72
3.3.2.8	Results: directivity patterns	73
3.4	Proposal for improvements	74
3.4.1	Mechanical control and prediction of the ground planeshape	75

3.4.1.1	Distribution of the actuators for the control of the ground plane shape	75
3.4.1.2	Approximation and prediction of the ground plane shape for a linear array	77
3.4.1.3	Results	82
3.4.1.4	Solution proposal to improve the layout	83
3.4.2	Iteration on the possible set of deformations	84
3.4.3	Final methodology proposal for a linear <i>RRA</i>	89
3.4.4	Validation of the methodology by comparison with full-wave simulations	90
3.5	Conclusion	91
4	Extension of the methodology for a 2D case and breadboard testing	93
4.1	Introduction	95
4.2	Methodology for a 2D <i>RRA</i>	95
4.2.1	Application case definition	95
4.2.2	Application of the extended design methodology	98
4.3	Breadboard	105
4.3.1	Preliminary remarks	105
4.3.2	Objectives and inputs of the breadboard	106
4.3.3	Identification of the new ground plane shapes	107
4.3.4	Identification of the actuators displacement	109
4.3.5	Prediction of the ground plane shape	110
4.3.6	Predicted RF results	111
4.3.7	Outputs of the breadboard definition	113
4.4	Design and fabrication of the breadboard	113
4.4.1	Constraints of integration	113
4.4.2	Rear-structure	113
4.4.3	Actuators and surface-to-actuator interface	115
4.4.4	Ground plane	117
4.4.5	<i>RA</i> panel and its support system	118
4.5	Control and prediction tests of the ground plane shape	119
4.5.1	Photogrammetry tests definition	119
4.5.2	Photogrammetry tests results	121
4.6	RF performance	122
4.7	Conclusion	127
5	Conclusion	129
A	Investigation for a three-configurations <i>RRA</i>	132
A.1	Description of the proposed structure	133
A.1.1	Initial cells' selection process	135
A.1.2	Refinement in the selection process	136
A.2	Results and limits	136

A.2.1	Optimized design	136
A.2.2	Theoretical radiation patterns	137
A.2.3	Radiation patterns using fullwave simulations	140
Bibliography		142

A Lionel, Monique, Pierre, Raymonde

General introduction

Context of the study

This thesis project is proposed and performed in the context of the REVOLVE project funded by the European union's Horizon 2020 research and innovation program under the grant agreement n° 722840.

REVOLVE is structured around several partners located all over Europe, such as Heriot Watt University (Scotland), Institut d'Electronique et des Technologies du numéRique (IETR - France), Large Space Structures (Germany), Thales Alenia Space (France), and Inicio (Spain). This European initiative aims to develop new solutions for future satellite systems through seven PhDs. This thesis is the "ESR5" of the REVOLVE project, and realized under the supervision of Professor Raphaël Gillard (IETR), Professor George Goussetis (Heriot Watt University), and Doctor Erwan Fourn (IETR).

This work began in October 2017 at Thales Alenia Space (Toulouse, France) for two months with the other Ph.D. fellows of the REVOLVE project. These two months were used to gather information on antenna reconfiguration and reflectarray antennas *RA* technology to propose a reconfiguration concept for *RA*. It was followed by nine months at IETR in Rennes, France, within the scope to initiate a design methodology for reconfigurable reflectarray with a flexible ground plane. From October 2018 to March 2019, a secondment has been done in Edinburgh in the laboratory of Heriot Watt University to continue this study while considering a wider range of constraints to take into account for the design of a *RA* with a flexible ground plane notably for its shape control. As the work was mainly focused on the electromagnetic aspect, nine months were passed in Large Space Structures in Eching, Germany. This time was spent converging to a final methodology design taking into account electromagnetic and mechanical aspects. Finally,

a three-months period at LSS and two months at IETR aimed to finalize the design, the assembly of the demonstrator, and the measures. These measurements were performed at IETR.

Subject

The telecommunication market has grown rapidly these last decades due to the numerous satellite applications for civil and military communications, radars, geolocalization, and scientific missions. In this context, the design of the satellite's antennas has been investigated to improve their performances, notably for Space applications which imply specific constraints, such as the cost, the weight, the performances, and the reliability versus the thermal and mechanical constraints that the system will handle during its life cycle.

This thesis investigates the mechanical reconfiguration of reflectarray antennas based on the deformation of the ground plane. The work performed by Large Space Structure in collaboration with Thales Alenia Space with the support of ESA on reconfigurable reflectors [39, 41] is the starting point of the concept proposed in this document.

The interest in the reconfiguration of antennas increased due to the fast growth of the market, the emergence of satellite constellations, and the necessity of improving the performance of the existing antennas technologies [42–45]. The possibility to tune the antenna's characteristics would lead to a faster adaptation to the market evolution, a modification of the radiation pattern to adapt it to the meteorological conditions [46], nevertheless, other benefits are envisaged notably for the compensation of shape errors [40, 47].

This thesis focuses on the mechanical reconfiguration of reflectarray antennas (RAs) by modifying the distance between the metallic elements and the ground plane. The reflecting elements (also called cells) are composed by the metallic pattern, the substrate on which it is printed and the ground plane. Indeed, it is possible to control the reflected phase of the cell, and so to change the radiation pattern provided by the antenna, by tuning this distance.

Scope of the document

The manuscript is divided into five chapters. The first chapter presents the state-of-art of existing antenna technologies and reconfiguration methods focusing, of course, on reflectarrays. It presents the reflectarray concept by describing the existing antenna technologies, the radiating elements, and the possible applications of such systems. Then, the existing reconfiguration methods are detailed to introduce the concept proposed in this thesis.

The second chapter presents the analysis and modeling of reflecting elements (second-order Phoenix cells) printed on the *RA* panel considering a tunable distance between the cells and the ground plane. A semi-analytical tool, whose purpose is to extract with good accuracy and a reduced computation time the reflected phase of the cells versus the distance h , is then developed and validated by fullwave simulations. This tool is used afterward to build a database of reflecting elements useful for the Reconfigurable Reflectarray Antenna (*RRA*) design.

The third chapter details the definition of the design methodology of a two-configuration *RRA*. This methodology is applied to a linear array sample and discussed to improve it step by step. A final proposal is then tested thanks to fullwave simulation.

The fourth chapter extends this methodology to a 2D sample case from which the linear array was extracted. It also presents a demonstrator assembled to validate the concept of a *RRA* with a flexible ground plane.

Chapter 1

Reflectarray antennas and reconfiguration

Contents

1.1	Introduction	5
1.2	Reflectarray antenna technology	5
1.2.1	Reflector antennas	6
1.2.2	Array antennas	8
1.2.3	Reflectarray antennas	9
1.2.4	Conclusion	24
1.3	Existing reconfigurability concepts	24
1.3.1	Electrical reconfiguration	25
1.3.2	Optical reconfiguration	26
1.3.3	Material change reconfiguration	26
1.3.4	Mechanical reconfiguration of the radiation pattern	27
1.3.5	Conclusion on reconfiguration techniques	32
1.3.6	Multi-objective optimization	33
1.4	Reconfiguration concept proposal	33
1.4.1	Description	33
1.4.2	Study issues	35
1.5	Conclusion	36

1.1 Introduction

For decades, the telecommunication market has grown rapidly, which has led to the necessity to increase the performance of the antennas while reducing their size, and manufacturing cost. Following this tendency of technical improvements, different concepts have been studied that usually rely upon parabolic reflectors, shaped ones, or arrays, notably for high-gain antennas or antennas with a large aperture.

Reflectors and array antennas have been largely investigated these last decades due to their good features. Indeed, parabolic reflectors have a relatively structural simplicity and lightweight compared to arrays. Nevertheless, parabolic reflectors are more difficult to manufacture due to their curved reflecting surface shape. Reflectors cannot achieve wide-range electronic beam scanning, whereas array antennas can while becoming complex and costly.

To overcome the limitations of these two technologies and take advantage of both good features, reflectarray antennas (*RA*) were introduced by Berry [48] in 1963. It combines the best features of the parabolic reflectors and arrays with the purpose of replacing shaped reflectors. The reflectarray antenna technology has been studied these two last decades to provide intricate radiation patterns with a relative simplicity of manufacturing, low-cost, low-profile, and good performance.

The first section of this chapter presents the reflectarray concept by describing the existing antenna technologies, the radiating elements, and the opportunities offered by this new class of antennas. Some studies have been pursued to provide electronic or mechanical reconfiguration to allow more flexibility. The second section details some of the proposed solutions. Finally, the reconfiguration concept discussed in this thesis is described in the last section, with an overview of the possible targeted applications.

1.2 Reflectarray antenna technology

Reflectarray antennas (*RA*) consist of an array of radiating elements periodically spaced on a flat surface to reflect the incident wave from a feed source in the desired

direction. Due to their features, *RAs* are considered as a hybrid solution between reflector antennas and array antennas.

Reflectarray antennas have the same feed mechanism as the reflectors, and are composed of multiple radiating elements as array antennas.

In this section, both reflectors and array antennas are presented to introduce reflectarray antenna technology.

1.2.1 Reflector antennas

Reflector antennas are developed to follow the high demands for radar applications, radio astronomy, microwave communication, and satellite tracking. Their structural simplicity, low-mass, and mature design make them the most popular antenna system for spacecraft applications [49].

The reflector antenna principle is to collimate the waves from a feed illuminating a reflecting surface in a given direction, such as shown in Figure 1.1.

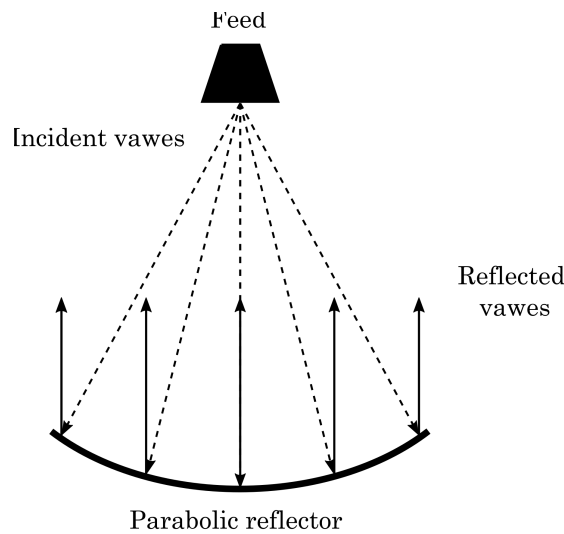


FIGURE 1.1: Principle of a reflectarray antenna.

As Figure 1.1 illustrates, the incident waves hit the reflecting surface and are reflected to create a specific wavefront. Consequently, the radiation pattern provided is directly dependent on the reflector's geometry.

The main advantage of a reflector antenna is its low-cost and high gain. Nevertheless, adding a beam-steering capability to a reflector is complex as a mechanical scanning system needs to be implemented [50].

The common shape of reflector antennas is parabolic, but other shapes such as hyperbolic, ellipsoid, corner, plan, or spheroid exist. Figure 1.2 illustrates some of them.

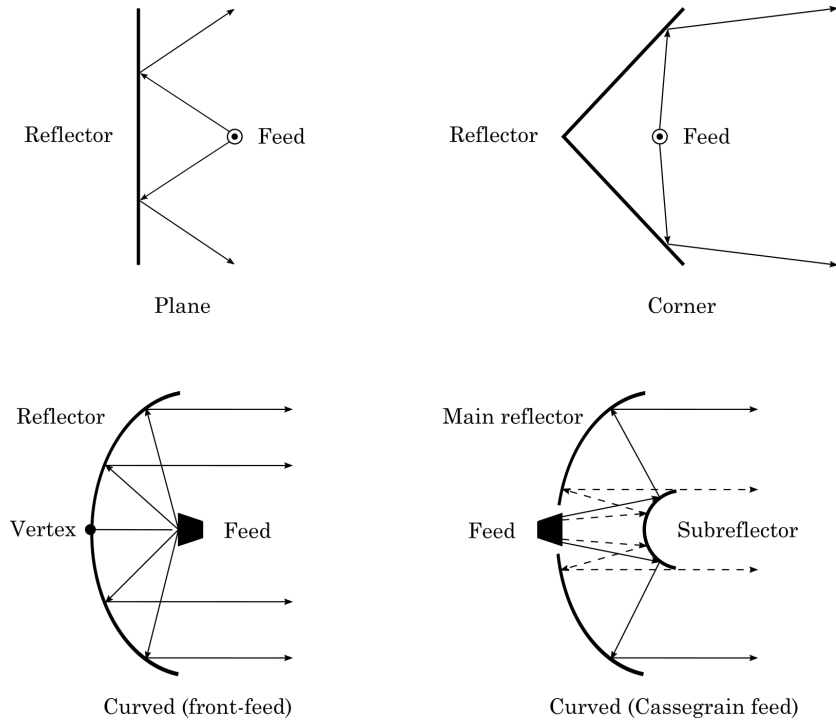


FIGURE 1.2: Geometrical configuration for some reflector systems.

The reflector concept has been enhanced to develop antennas that consist of deformed reflectors to provide contoured beam and illuminate specific regions of Earth, notably for communication satellites. Figure 1.3 presents an example of a shaped reflector.

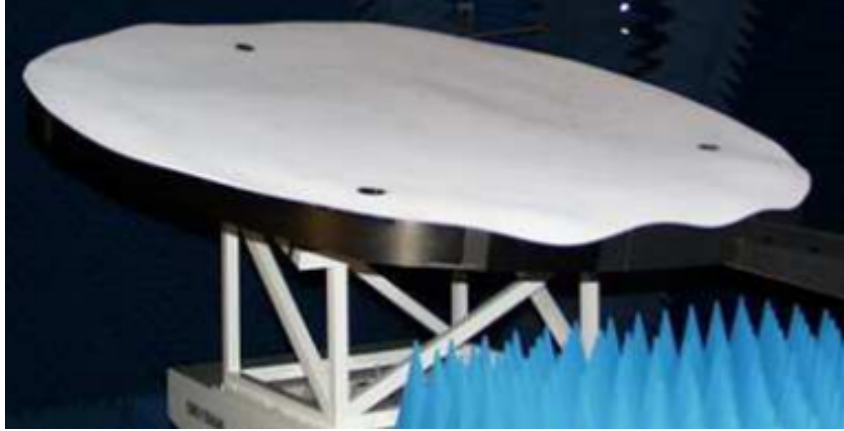


FIGURE 1.3: Example of a shaped reflector with large aperture [51].

For the shaped reflectors the surface's shape has to be accurate enough to present good radio frequency (RF) features and reliability. This accuracy mainly depends on the manufacturing, the prediction of the shape and RF performance [52], and on its aperture size.

Moreover, the design of shaped reflectors induces several constraints in terms of volume [53–55], cost and fabrication. Indeed, molds are needed to manufacture the specific shape of the shaped reflectors [52]. This molding process is costly and increases the manufacturing complexity.

1.2.2 Array antennas

Array antennas consist of radiating systems composed of multiple elementary distributed sources working together to generate the desired radiation pattern [56] [57]. The main purpose of this technology is to obtain a large antenna aperture compared to single antennas, thus enabling higher RF performance in directivity and radiation pattern synthesis.

Each element of the array can be connected to a single receiver or transmitter by feed lines to adjust its excitation law. Then, by tuning the excitation of each array element differently, it is possible to generate a customized pattern. The radiated field of each source is then superposed to enhance the power radiated in a specific direction.

The radiated characteristics of the system are then dependent on :

- the radiation pattern of the single element
- the magnitude and the phase coefficient of the excitation of each source
- the distance between each element

The main disadvantages of array antennas are the high losses that need to be compensated through the excitation of the sources, thanks to amplifiers. Adding these components to the antenna system leads to higher cost, complexity, and weight.

1.2.3 Reflectarray antennas

In the 60's, Berry validated the reflectarray principle by testing an array composed of waveguides and short-circuits to generate pencil beams, broad beams, and scanning beams [48]. Each waveguide composing the array re-radiated the incident field with a specific phase shift depending on their length to form a beam in the far-field distance. Several years later, a similar application was proposed by Roederer for radar applications [58].

In the 80's, the printed reflectarray was introduced as the first low-profile reflectarray using printed microstrip elements [59, 60]. As an example, the flat panel implies fewer constraints for the manufacture and reduces the price notably because no mold is required.

Many researches were initiated on reflectarray antennas to take advantages of their good features or improve them [61–69]. This section introduces the *RAs*, their advantages and disadvantages, and some possible applications.

1.2.3.1 Principle

Reflectarray antennas are derived from simple reflectors and array antennas. They have been studied as a new solution to reach a better performance than shaped reflectors in terms of mass, cost, and volume [70] for space applications.

As for the waveguide reflectarray presented by Berry in [48], printed reflectarrays consist of planar elements that re-radiate the incident field with a particular phase shift to produce a collimated or a shaped beam. Each element is individually

tuned to produce the appropriate phase distribution of the reflected field. Figure 1.4 illustrates the principle of a *RA* antenna system. The excitation law applied to the radiating elements printed on the flat panel is identified to produce the desired radiation pattern.

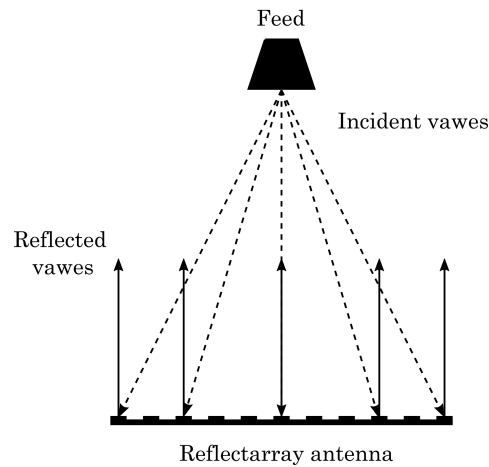


FIGURE 1.4: Principle of a parabolic reflector.

A particularity of the printed reflectarray antennas relies on controlling the reflection phase of each element by adjusting its geometry. Hence, the excitation law is synthesized by varying the shape or the size of the radiating cells. The panel is then composed of various geometries of cells. An example of a *RA* is illustrated in Figure 1.5.

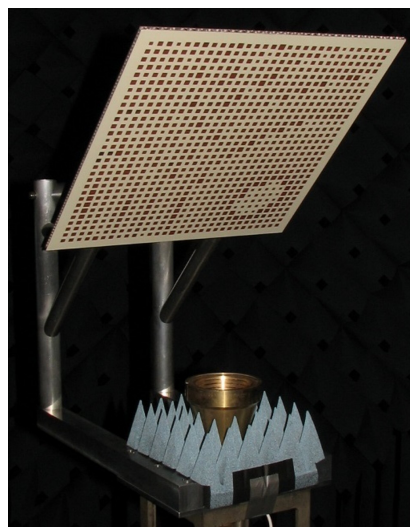


FIGURE 1.5: Example of a flat reflectarray antenna (source: www.esa.int).

RA antennas are mainly used to generate directive or shaped beams. In the case of a directive beam, the reflecting elements (also called cells) are selected to compensate for the path between the feeding source and each cell. Shaped beams can then be synthesized by the introduction of a specific phase shift from each cell, in addition to the feed-to-cell path compensation, according to the targeted pattern.

Figures 1.6 and 1.7 present the principle of an *RA* illuminated by a feed to produce a directive beam and a shaped one [51].

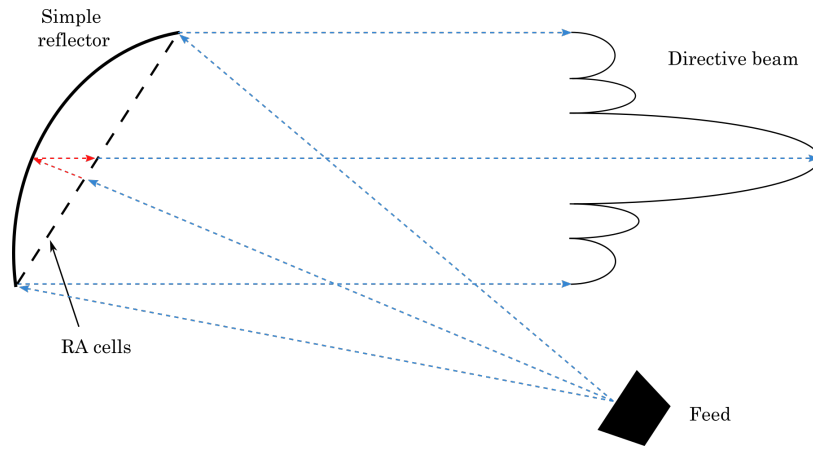


FIGURE 1.6: Shape comparison between a reflectarray and a simple reflector to produce a directive beam.

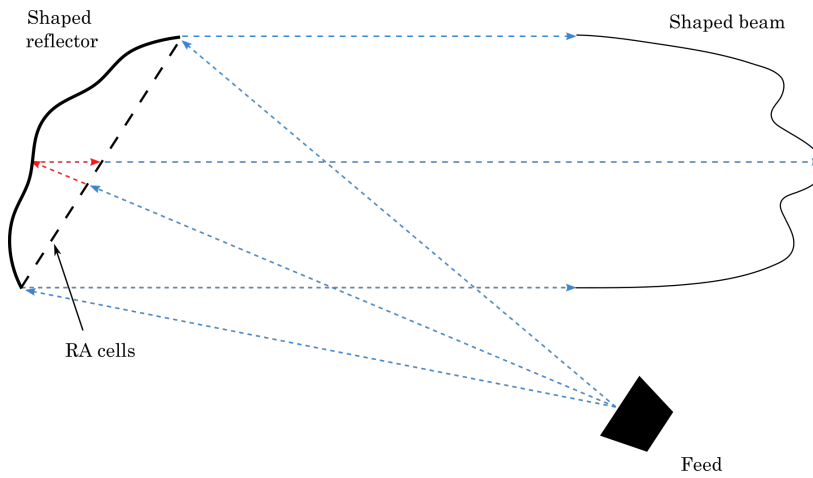


FIGURE 1.7: Shape comparison between a reflectarray and a shaped reflector to produce a shaped beam.

1.2.3.2 Advantages and disadvantages of reflectarray antennas

The reflectarray antennas offer a high gain thanks to their similitude with reflector antenna and provide adaptive beam-forming capabilities as an array antenna. These antennas have the main advantages to be low-profile, easy to manufacture, low-weight, and have good efficiency, and high gain compared to the existing antenna technologies [50].

As the telecommunication market targets large aperture spacecraft antennas, while also requiring compact systems with deployment mechanism, the flat structure of *RAs* presents a significant interest compared to parabolic reflectors. Indeed, the folding mechanisms are then simplified and more reliable [71].

Nevertheless, the literature points out the disadvantages of the reflectarray, such as its limited bandwidth due to the frequency dispersion [72] and the unit element bandwidth [73].

1.2.3.3 Development of the radiating elements

As presented in the last section, the reflectarray concept is based on the reflector and array principle. The radiation pattern provided by the reflectarray depends on the excitation law applied to the radiating elements and on their reflection characteristics. The control of this reflection could be made by adjusting the elements' geometry across the array. As a consequence, most solutions are based on the variation of unit cell dimension characteristics, such as the size of a patch, or rotation angle, to provide any phase shift variation. Following the same path, most efforts have been made for reflectarray design to find the suitable elements that provide a broad range of phases and a phase that does not vary too much with the frequency. This section mentions non-exhaustively some of the reflectarray designs proposed these last decades.

One technique to control each element phase is to connect transmission line segments or stubs of different lengths to the microstrips to add phase delay [74–76]. The disadvantage of this solution stands on the dissipative losses induced by the stubs.

Other concepts of microstrip reflectarrays have been developed, such as rectangular patches [77], aperture-coupled patches with stubs [78, 79], variable-size patches

[80], multiple-layers cells. Using panels with various sizes of patches reduces the complexity of implementation compared to the patches with stubs technology. Therefore, the dissipative losses are also reduced.

A multiple-layer cell has been proposed in [81] to improve the phase range and frequency band. This cell is a superposition of multiple patches of various sizes printed over a ground plane and separated by a dielectric. Figure 1.8 represents a schema of a typical multi-layer radiating element.

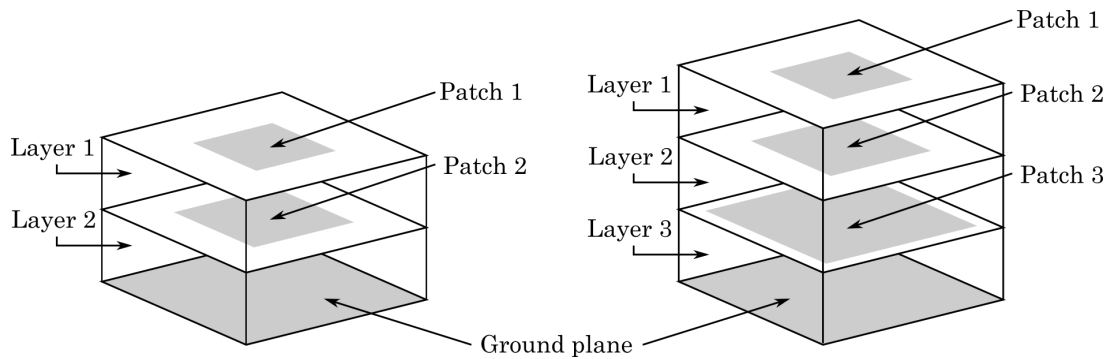


FIGURE 1.8: Representation of a multi-layer patch: (left) two layers and (right) three layers.

M. R. Chaharmir developed a one-layer cell with multiple resonators to improve the phase range and the frequency band while ensuring an easy manufacturing capability of the antenna. It consists of multiple concentric resonators printed on a single-layer substrate located over a ground plane [82, 83]. The method has been tested on a double-band reflectarray antenna in [84].

Inspired by this concept, a new cell with good features has been developed named Phoenix cell. This new cell allows a smooth geometry variation all over the RA surface, which is the condition for complying with the local-periodicity assumption. This cell is a small patch with two concentric slots printed in a ground plane [2].

The main advantage of the Phoenix cells, in addition to the smooth variation of geometry, is their re-birth capability [84]. Indeed, after a complete 360° phase range, the cell geometry is the same.

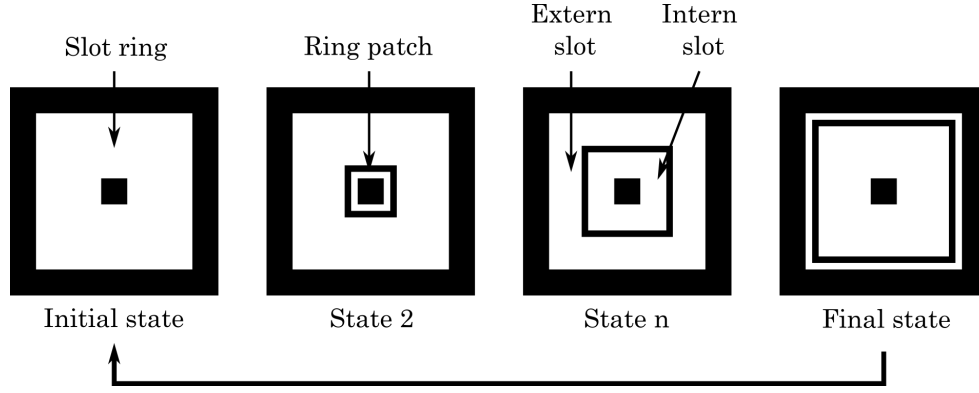
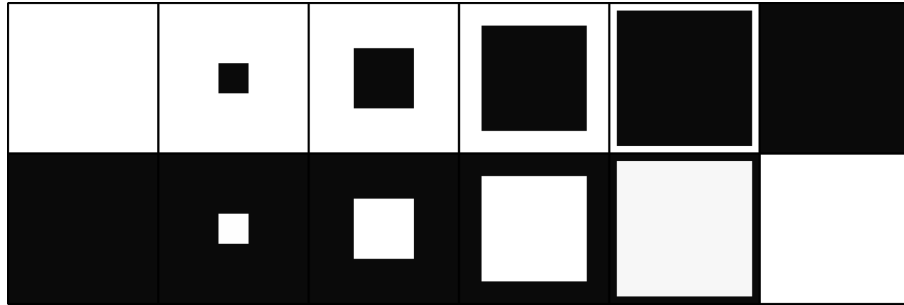


FIGURE 1.9: First Phoenix cycle [2].

Different versions of the Phoenix cell have been studied notably in [85, 86] until [87]. In [87], the Phoenix cycle has been defined thanks to the capacitive and the inductive geometry of the cell placed successively. Figure 1.10 presents the Phoenix cycle for a first-order cell. The advantage of this cycle is to provide two complementary phase ranges while avoiding dispersive behaviors [87].

FIGURE 1.10: Phoenix cycle for a first-order cell capacitive (*top*), inductive (*bottom*).

As it is illustrated in Figure 1.10, the cycle consists of two phases. During the first one, a square patch is enlarged until it fills the cell surface. During the second one, a slot is inserted in the middle of the patch. Its size increases until the metallic part disappears.

Phoenix cells are promising for their performance and allow a complete phase cycle of 360° with a smooth variation of geometry and low-frequency dispersion. Nevertheless, the first order Phoenix cells' capabilities are limited due to its single tuning parameter, and the re-birth capability of higher orders is not easy to handle due to the multi-dimensional geometry.

In this thesis, the second-order Phoenix cells have been considered by replacing the square patch or aperture (see Figure 1.10) with a square ring. Figure 1.11 presents the geometry of a second-order Phoenix cell. Adding this new degree of freedom provides more flexibility to control the reflection characteristics of the cell.

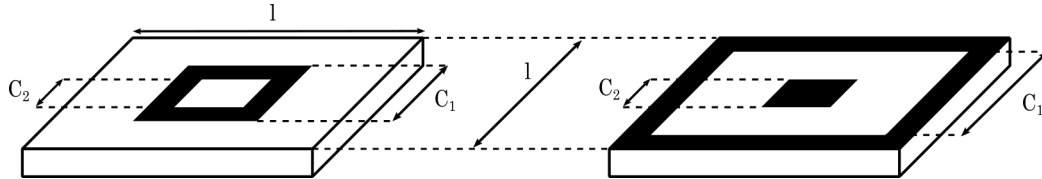


FIGURE 1.11: Capacitive (*left*), inductive (*right*) second-order Phoenix cells [88].

1.2.3.4 Phase law definition

The radiation pattern of the reflectarray is directly coupled with the phase law applied to the panel composed of the reflecting elements. The phase law is defined as the sum of the incident field delivered by the primary source and the introduced phase given by the radiation characteristics of the cells distributed all over the panel.

The incident field depends on the antenna configuration and more precisely, on the illuminating feed itself and its position. Indeed, it defines the phase delay compensation that has to be done between the radiating elements and the feed.

1.2.3.4.1 Incident field from the primary source

Let consider that the incident wave reaches the center of the n radiating element of the flat surface (or panel) with an incident phase (ϕ_n^{inc}), depending on the wavelength λ_0 and the distance S_n between the feed and the cell. Equation 1.1 gives the relation between those variables for cell n .

$$\phi_n^{inc} = -\frac{2\pi}{\lambda_0} S_n \quad (1.1)$$

Considering that the center cell of the panel is the reference one ($Cell_0$), the phase of the incident field (ϕ_0^{inc}) is given by the Equation 1.1, with S_0 the distance to the feed.

The incident field at the center of $Cell_n$ takes into account the phase delay, $\Delta S_n = S_n - S_0$, compared to the reference cell's one ($Cell_0$). Equation 1.2 gives the incident phase at the center of $Cell_n$ considering the variables illustrated in Figure 1.12.

$$\phi_n^{inc} = -\frac{2\pi}{\lambda_0} S_n = -\frac{2\pi}{\lambda_0} (S_0 + \Delta S_n) \quad (1.2)$$

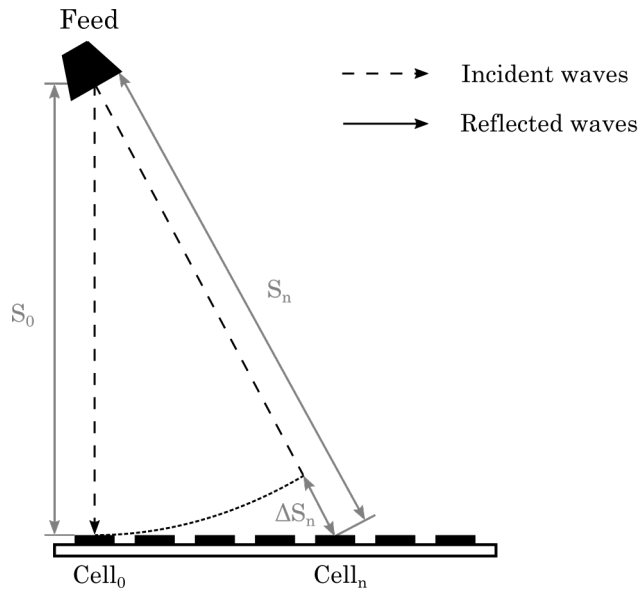


FIGURE 1.12: Radiating paths between the feed and the *RA* panel.

The phase shift between the cells of the panel is due to the phase delay introduced by the path that a wave has to follow to reach each element.

1.2.3.4.2 Introduced phase and radiation

When the incident wave reaches the surface and illuminates the reflecting elements, each of them has to radiate the energy with a specific phase shift, named introduced phase and noted ϕ_n^{int} for the n cell. The phase of the re-radiated wave (ϕ_n^{rad}) is equal to the sum of the incident phase and the introduced one of $Cell_n$

as in Equation 1.3.

$$\phi_n^{rad} = \phi_n^{inc} + \phi_n^{int} \quad (1.3)$$

The main radiation patterns targeted with reflectarray antennas are the ones along the broadside and steered (cf. Figure 1.13) or shaped beams.

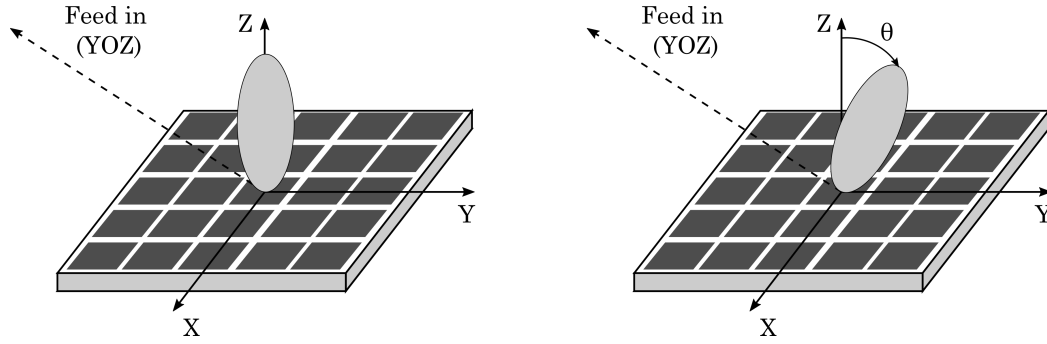


FIGURE 1.13: (Right) Radiation with a steering - (left) Radiation in the broadside direction (array axis).

1.2.3.5 Few examples of applications

New applications take advantages of the interesting features of the *RA* concept and are presented in this section. The main purpose is to guarantee good RF performance while preserving or improve its characteristics such as the simple manufacturing process, the low-weight, or the low-profile. This section presents three possible applications envisaged for reflectarray antennas.

1.2.3.5.1 Very large aperture

The demand for large-aperture antennas increases since decades and so the interest in deployable or foldable antennas in the space research area. Due to their storable, low-cost, and low-weight characteristics, reflectarray antennas seem to be good candidates compared to traditional antennas such as reflectors or array antennas.

In the 90's, Astro Aerospace Corporation contributed to the development of deployable mesh reflector technology with the AstroMesh deployable reflector (see Figure 1.14).

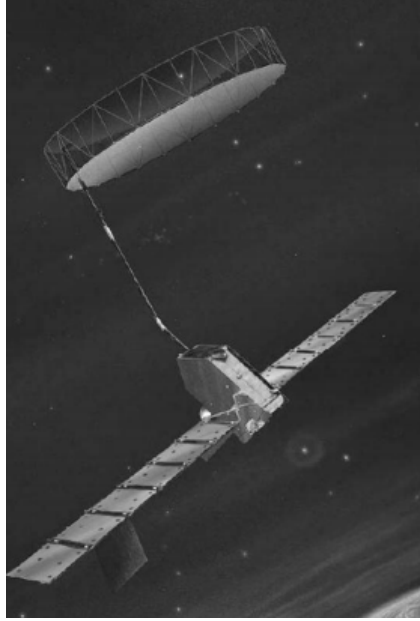


FIGURE 1.14: The AstroMesh in deployed configuration [89].

The resulting design was attractive due to its low mass, volume, high stiffness, thermal stability, and cost. It was studied to be applied to antennas with an aperture between 6m to 150m without major modification of their design. This effort led to multiple investigations on the design and analysis of deployable structures and mechanisms. Some examples of these concepts are detailed in [89–92].

The latest development of large *RA* combines the printed *RA* technology with the panel deployment method used for solar arrays to overcome the antenna's volume issue. It consists of several flat panels deployed to obtain a large surface illuminated by a single feed.

A large deployable *RA* has been studied by Thales Alenia Space and CNES to prove the feasibility of a 6-m and 10-m large deployable. Figure 1.15 shows the modelization of these deployed *RAs* [1].



FIGURE 1.15: 6m configuration for deployable *RA* (left) and 10 m configuration for deployable *RA* (right).

The ratio $\frac{F}{D}$, noted in Figure 1.16, has an important impact on the distance between the cell and the feed and so on its phase response with frequency. Hence, while increasing the size of the antenna, the bandwidth becomes more and more limited.

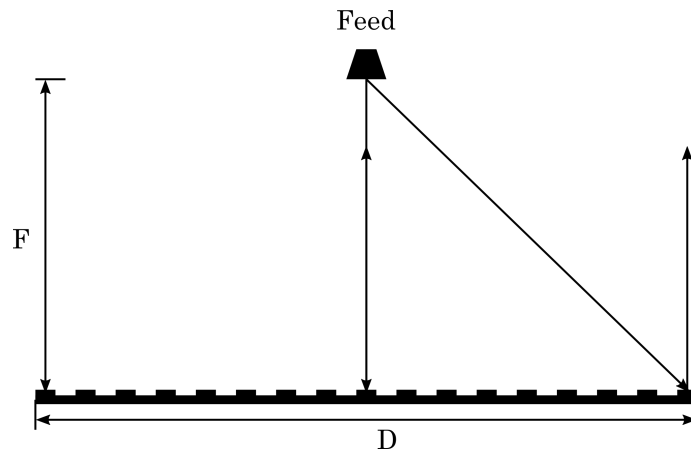


FIGURE 1.16: *RA* parameters.

Some solutions proposed were to use a locally flat antenna or to use a rectangular surface aperture [93] to overcome bandwidth and time-delay issues. One Ku-band radar application using very large aperture *RA* has been investigated by NASA and JPL. It has an aperture size of 2m x 0.5m and uses variable-size patches as elements. The antenna system consists of a set of five flat reflectarrays put together to form a curved parabola as Figure 1.17 illustrates it.

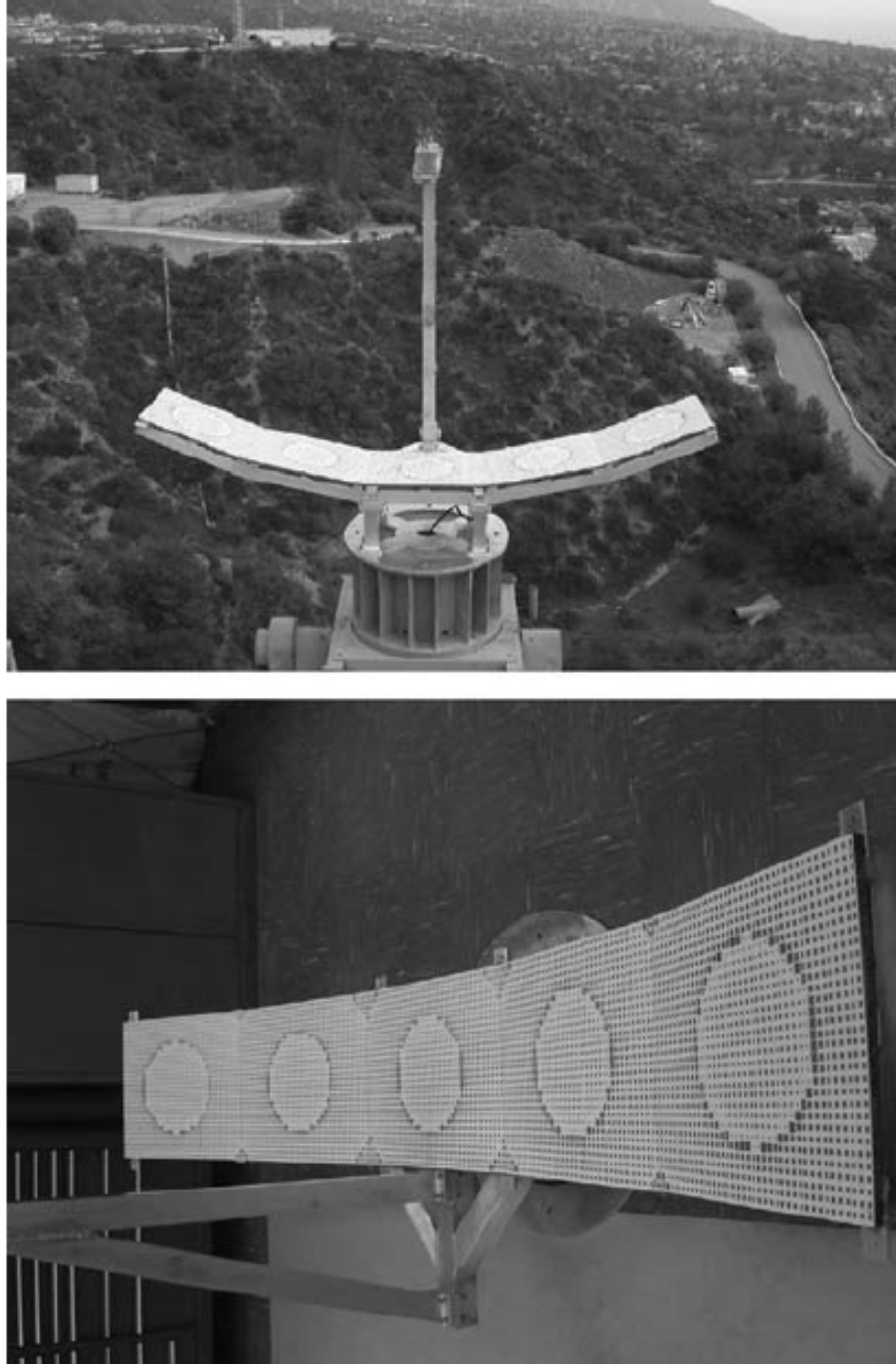


FIGURE 1.17: Photos of the NASA-JPL very large aperture *RA* 2m x 0.5m [1].

1.2.3.5.2 Inflatable and self-rigidizable membrane reflectarrays

The main goal of inflatable membrane reflectarrays is to propose an antenna with lower mass and smaller storable volume than a classical *RA* while ensuring the RF performance [94]. In the last section, the interest and the limitation due to the antenna size of large deployable structures have been underlined. Some

examples of inflatable deployment systems have been investigated to propose an accurate, low-mass system as it is presented in [71, 95, 96].

The development of inflatable structures needed the investigation of the possible supporting structures to ensure the feasibility of such technology. The major challenges for an inflatable antenna are: controlling the deployment, stabilizing the antenna's shape, and the accuracy of the final shape.

Most of the developments have been performed on reflector antennas, such as the Inflatable Antenna Experiment (IAE) initiated by the Jet Propulsion Laboratory (JPL). Then, this technology was applied to reflectarray antennas because of their flat surface that allows better reliability [94].

Figure 1.18 is the picture of a one-meter inflatable reflectarray antenna developed by JPL/NASA [97]. It consists of a planar array on which multiple microstrip patches were printed. At the edge of the membrane, a circular tube is attached and inflated to stretch the membrane as flat as possible. Once the structure is inflated, it is used as support. Other tubes are used to support a feed horn that illuminates the *RA*.

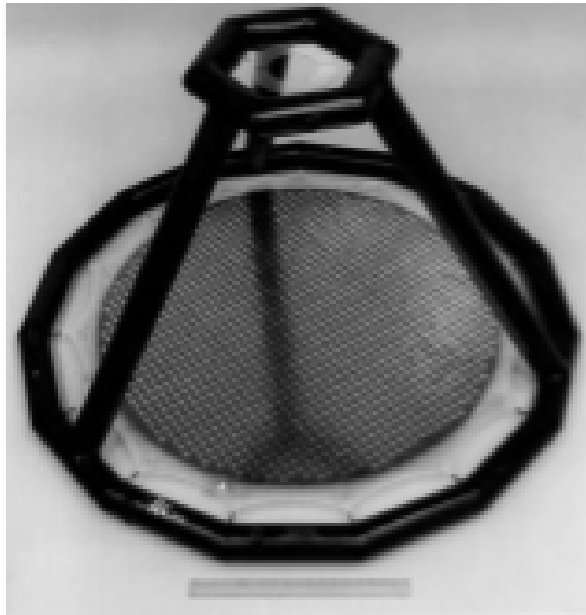


FIGURE 1.18: X-band 1-m Inflatable Reflectarray.

Once inflatable *RA* antenna has been designed and tested with a diameter of 1-m for the X-band (cf. Figure 1.18) and thanks to the good RF results, a three-meter

technology demonstration model of the inflatable reflectarray was also developed (see Figure 1.19) [98, 99].



FIGURE 1.19: Ka-band 3-m Inflatable Reflectarray [99].

Even if these concepts are interesting due to their weight, they present some disadvantages, notably due to the place of the feed and the amplifiers and the space environment constraints.

Some other designs have been investigated, such as the *movie screen*, which is an inflatable/self-rigidizable reflectarray antenna [94]. Its design is based on the same principle as for the 1-meter and 3-meter inflatable antennas except that it is illuminated by an offset feed and that the reflectarray surface is deployed independently from the feed by two inflatable booms.

Figure 1.20 illustrates the principle of this *movie screen* inflatable reflectarray antenna.

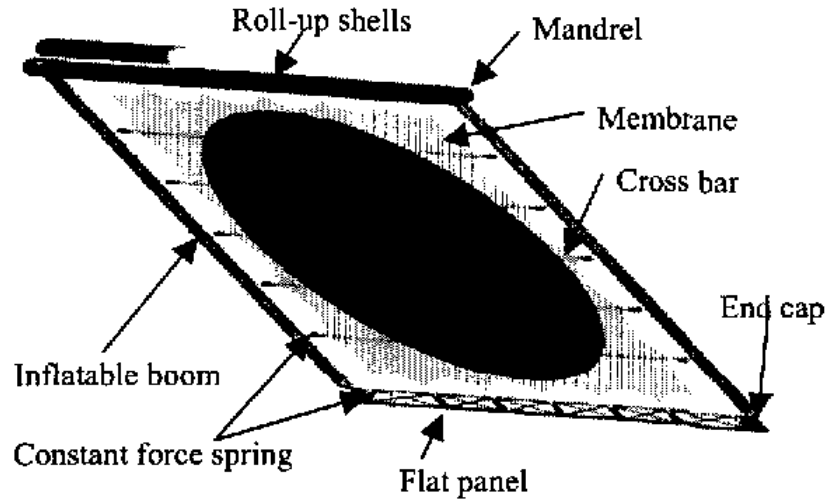


FIGURE 1.20: Principle schema of the "movie screen" reflectarray antenna [94].

In addition to the RF constraints existing with this new kind of antennas, mechanical constraints need to be taken into account due to the space environment. Nevertheless, new investigations have been initiated for new composite systems or new materials to overcome these limitations.

1.2.3.5.3 Contoured beam reflectarrays

RAs are good candidates for a contoured beam to replace the shaped reflectors that are expensive. As it has been reminded before in this chapter, the main advantage of the reflectarray antenna is that the elements' reflection phase could be adjusted to radiate as a shaped reflector. Hence, the volume of the antenna is reduced while ensuring the RF performance of a shaped reflector.

The main advantage of the *RA* compared to the shaped reflector is that a specific mold is not necessary for each coverage. The cost of manufacturing then decreases, considering that only the printed patches must be adjusted for specific coverage.

In [100], a contoured beam reflectarray is designed for a direct broadcast satellite European coverage application in the Ku-band.

In [101], a multi-facet composite panel reflectarray for space contoured beam antenna in Ku-band is proposed. It consists of a 1.3m reflectarray that has been designed, manufactured, and tested to provide a contoured coverage over North America.

1.2.4 Conclusion

The two main problems of RA are the narrow bandwidth, which is limited by the characteristics of the elements used (dispersive nature of the cells), and the coupling effects between the cells [84]. Those effects are even more enhanced when the geometrical differences between cells are large when a new period of 360° of the reflected phase begins, for example.

Due to these two problems, the challenge in the design of reflectarrays is to find a cell with a smooth geometry variation over the array with a capacity of coming back to its initial shape after a whole theoretically 360° phase [102].

To overcome the limited bandwidth, a new type of cells has been introduced: the Phoenix cells [84]. Thanks to their good features, Phoenix cells are good candidates for the reconfigurable RA concept investigated in this thesis.

1.3 Existing reconfigurability concepts

Two types of reflectarray antennas must be distinguished: the reconfigurable and the passive ones. Passive *RAs* produce a fixed radiation pattern while the reconfigurable ones can modify their radiation properties.

The purpose of on-orbit reconfiguration for satellite antennas is to make Telecommunication and Earth Observation missions more versatile. For example, it could be used for the modification of the coverages to follow the market evolution. It could also be used for the adaptation of the radiation patterns to the meteorological conditions (mitigating absorption losses by rain and snow) or the compensation of the thermal distortions. Finally, the reconfiguration can be defined as the antenna ability to radiate more than one coverage considering several frequencies or polarizations.

Six major methods to add reconfiguration capability to antennas have been investigated and sorted in four categories: Electrical (Varactor [3–8], PIN diodes [9–20], and RF-MEMs [21–26]), Optical (Photoconductive [27–31]), Mechanical (Modification of the antenna structure [32–34]), and Material change (Ferrites [35, 36] and liquid crystal [37] [38]). This section aims to go through the main solution

proposals in terms of antenna reconfiguration and details the mechanical existing solutions.

1.3.1 Electrical reconfiguration

The electrical reconfiguration of reflectarray antennas has been investigated due to their attractive qualities and the possibility to modify the reflection characteristics of the radiating elements. It is based on the integration of elements such as varactor, diodes, PIN diodes switches [50], MEMs [103, 104] to tune the provided radiation pattern.

The development of reconfigurable reflectarrays, and different tested techniques are discussed in terms of maturity, availability, performance, complexity, suitability to a frequency range, and other parameters in [50].

Hence, the main challenge of this kind of concept is to propose a reconfiguration of the beam with a moderate cost. Electronically reconfigurable *RAs* usually suffer from their high cost, complexity, high power consumption, weight, and volume notably due to the integration of electronic components. Two main types of components could be distinguished:

- Diodes PIN, and MEMs which allow a discrete variation of the phase,
- Varactors that allow a continuous variation of the phase.

In [105], the definition of varactors, PIN diodes, and RF-MEMs are given as follow:

- Varactors: They consist of a p-n junction diode. As the bias voltage applied to the diode is varied, the varactor capacitance is going to be changed. Typical values are from tens to hundreds of picofarads.
- PIN diodes: They operate in two modes. The "ON" state, where the diode is forward biased and the "OFF" state, where the diode is not biased.
- RF-MEMs: They use movement to achieve a short circuit or an open-circuit in a surface current path of an antenna structure. The forces required for the mechanical movement can be obtained using electrostatic, magnetostatic, piezoelectric, or thermal designs.

PIN and varactor diodes are mature technologies but are difficult to integrate and imply significant losses [106, 107]. To overcome these limitations, reconfigurable reflectarrays based on MEMs were developed [108–112].

PIN or MEMs are the most advantageous because the command is binary and easy to use, but the cell cannot provide a full phase range. As it is presented in [113], this technique relies on a compromise between the *RA* performance and its complexity. MEMs present some improvements compared to PIN diodes, even if they are less mature. For example, their low-loss up to mm-waves frequency, their good linearity over a large frequency band, and low power consumption. Nevertheless, MEMs present low stability with a variation of temperature, and consequently low-reliability.

MEMs components and PIN diodes are now used to improve the performance of phase shifters or reconfigurable antennas as in [114] and [115], notably for terrestrial and space applications.

1.3.2 Optical reconfiguration

The optical reconfiguration of an antenna consists of integrating an optical switch into the structure. This switch is controlled thanks to the light (incident wave) of the appropriate wavelength from a laser diode that hits a semi-conductor material. The incident field excites the electrons from the valence to the conduction band and creates a conductive connection.

This technique does not need biasing lines and has a linear behavior. Nevertheless, the main issues are the losses, the necessity of laser diodes, and the activation mechanism of the switches. [105] presents three possible activation techniques.

1.3.3 Material change reconfiguration

The material change reconfiguration relies mostly on the use of smart materials such as liquid crystals [37, 38] or ferrites [35, 36]. The change of the antenna's characteristics is implied by the modification of the substrate properties, such as its relative electric permittivity or magnetic permeability.

The dielectric constant of the liquid crystal can change with the applied voltage, whereas the permittivity or permeability of the ferrites can change due to the electric or magnetic field applied.

1.3.4 Mechanical reconfiguration of the radiation pattern

The mechanical reconfiguration of antennas has been investigated mainly for reflectors, notably because this technique does not rely on switching mechanisms, biasing lines, or laser diode integration. Avoiding these components allows less complexity in the integration, manufacturing, and assembly of the antenna. Several techniques to modify the antenna structures have been proposed and tested. This section aims to detail a non-exhaustive list of the possible methods to modify the radiation characteristics of the antenna.

1.3.4.1 Re-shapeable reflector/reflectarray antennas

The first reconfiguration method studied was to move or re-orientate the reflector mechanically to modify its radiation pattern by alteration of its initial configuration. The study of this solution has underlined some issues, such as high secondary lobes and cross-polarization. Hence, the modification of the reflector structure was envisaged [116, 117]. Figure 1.21 illustrates this reconfiguration method.

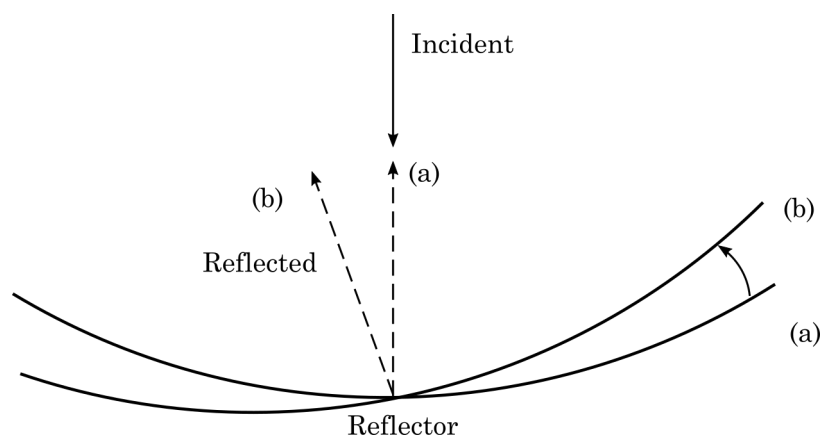


FIGURE 1.21: Reconfigurable reflectarray by modification of its configuration.

In the 90's, a reconfigurable reflector has been developed by alteration of its shape to re-orientate the field and change its shape.

In [39, 41], a step further has been achieved by dynamically modifying the shape of the reflector thanks to actuators placed under it. Nevertheless, it induces several mechanical problems in terms of concept (surface material, boundary conditions, realization, and interfaces), of actuators and actuation and of mathematical modeling (for the deformation).

In 2009, TICRA [118] studied the feasibility of a re-shapeable reflector antenna for satellite communications based on realistic mission scenarios and antenna configuration. The antenna was designed by Thales Alenia Space and tested for three intercontinental missions (Europe, Brazil, and the US). The study also proposed a comparison between three different design configurations. It concludes on the fact that a reconfigurable sub-reflector and shaped fixed main reflector is the best to optimize the RF performance.

Recent on-going activities funded by ESA aimed to demonstrate the feasibility of successfully re-shaping antenna reflectors made of a flexible membrane whose shape can be modified by using linear actuators. Figure 1.22 is a photography of the prototype for a deformable reflector.



FIGURE 1.22: Reflector antenna with reconfiguration capabilities thanks to actuators.

Nonetheless, it is important to note that the number of actuators is a problem because of its impact on the total mass of the system. Hence, this parameter is taken into account while optimizing the antenna configuration and its RF performance.

1.3.4.2 Selectable reflector/reflectarray antennas

In 2012, Thales Alenia Space developed a passive reconfigurable antenna using a selectable sub-reflector. Four sub-reflectors were designed to provide four different radiation patterns and placed on the antenna. The radiation pattern was then dynamically modified by selecting the corresponding sub-reflector thanks to rotational actuators, as shown in Figure 1.23 (left).

Based on the same concept, a mechanically selectable reflectarray antenna was investigated. In this case, the sub-reflectors were replaced by sub-reflectarrays to reduce the total volume of the RF system. These panels are designed thanks to the pre-definition of the coverages targeted by the operator. Consequently, this solution is interesting in terms of cost but has limited flexibility. In [118], this concept is presented as in Figure 1.23.

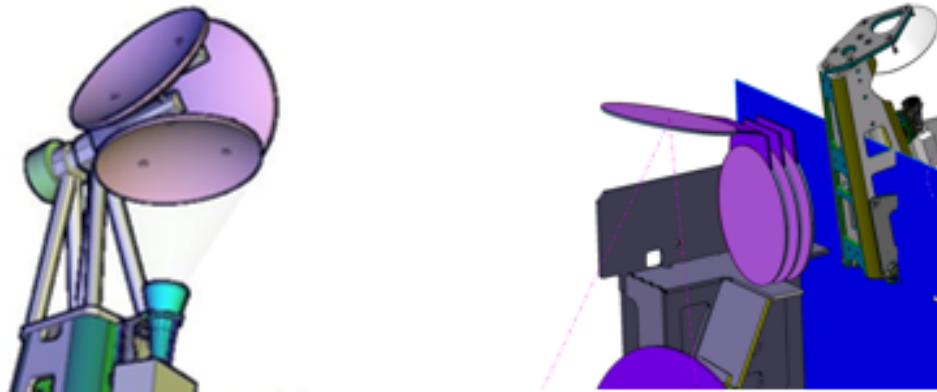


FIGURE 1.23: 3D view of a selectable sub-reflectarray (right), versus a selectable dish system (left).

1.3.4.3 Rollable reflectarray antenna

[119] proposes a rollable antenna to provide a reconfiguration of the radiation pattern. It has been studied for both transmittarray and reflectarray applications. It consists of two booms around which the panel is placed. The panel rolls by moving both mechanical axes, changing the surface illuminated by the feed. Figure 1.24 illustrates this concept.

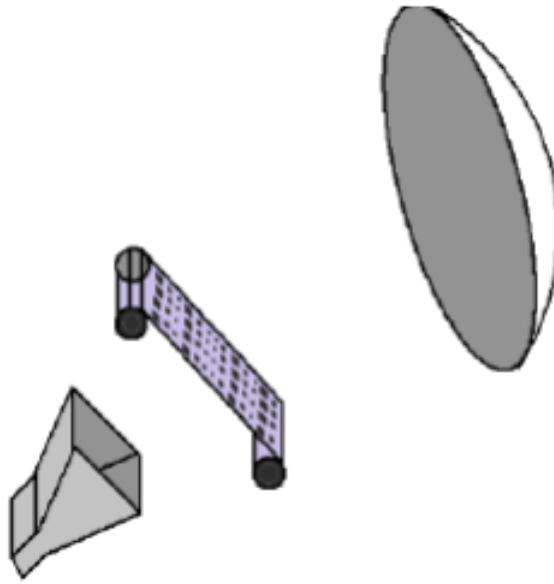


FIGURE 1.24: Concept for rollable reflectarray/transmittarray antenna.

The advantage of this concept relies on the relative simplicity of the system, but the fixed selection of cells limits the reconfiguration capability.

1.3.4.4 Motion of the ground plane

In [120], the height of patch elements is modified mechanically to vary their reflected phases. The radiating elements composing the reflectarray antenna consist of fixed upper patches and tunable slotted patches between which the height is controlled, thanks to actuators. The purpose of this article is to present a prototype of 408 cells for beam-scanning.

The reconfigurable *RA* designed presents good capability in terms of beam-scanning. Nevertheless, the height of each element is controlled individually, which leads to a complex, heavyweight, and costly solution.

In 2020, a reconfiguration concept based on the motion of the metasurface is proposed in [121]. It consists of a substrate with a periodic surface over a ground plane between which a variable cavity is formed and tuned thanks to piezoelectric actuators. Figure 1.25 schematizes the tunable piezoelectric actuated metasurfaces.

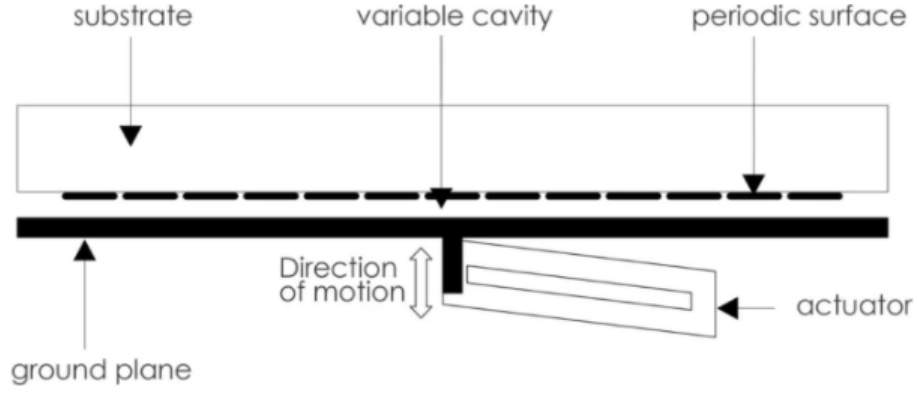


FIGURE 1.25: Schema of a piezoelectric actuator controlled by phase shifter [121].

This concept achieves a 360° or 180° phase shift at millimeter waves depending on the metasurface used. These reconfiguration possibilities present interest as they do not introduce additional losses considering that the actuators are under the ground plane (in opposition to the electronic reconfiguration presented before). The tunability of the radiation pattern is then directly dependant on the metasurface characteristics and accuracy of the piezoelectric mechanism.

1.3.4.4.1 Compensation of shape error

Hoernet and Wong [122] developed a mechanically deformable sub-reflector containing 4 actuators to correct a surface of a radio telescope at the National Radio Observatory (NRAO). Lawson and Yen in 1988 developed a deformable sub-reflector to compensate for the surface errors of a 46m radio telescope [123].

RAs could be used to compensate surface distortion of other types of antennas such as a simple reflector [124], notably for large deployable reflector antennas operating at high frequencies for which thermal effects cause surface distortions that degrade their performance. Figure 1.26 illustrates the developed concept.

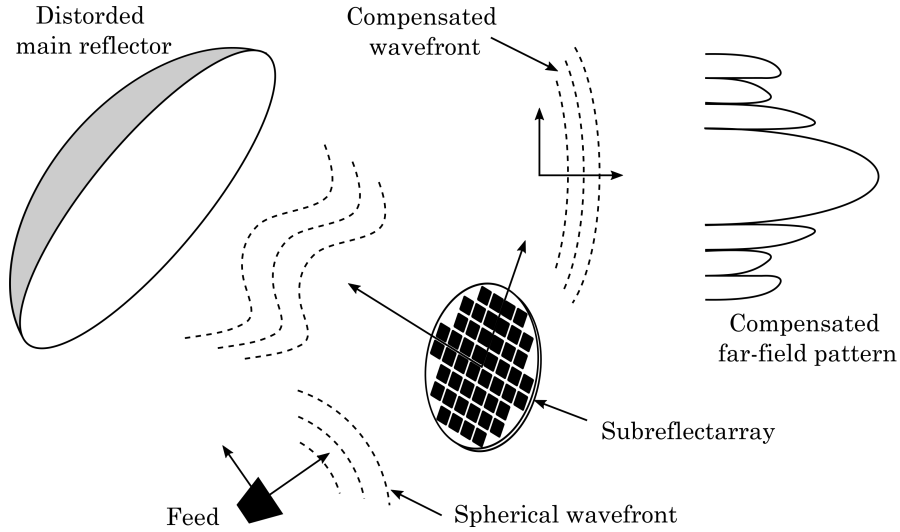


FIGURE 1.26: Concept for *RA* used for distortion compensation [124].

The *RA* can be used as sub-reflectarray in a Cassegrain configuration to adjust the phase and have a re-radiated wavefront optimized while minimizing the aperture phase errors caused by the main reflector. Compared to existing compensation techniques, the low-profile, cost-effective, and easy manufacture of the sub-*RA* make this solution interesting.

Other techniques exist using a distorted reflector or array antenna. Nevertheless, they are less interesting because of the losses, the complexity, or even the extra weight due to the number of array elements, the additional feed, and the beam-forming network.

1.3.5 Conclusion on reconfiguration techniques

Six methods of reconfiguration have been described in this section underlining the advantages and issues of each one. The main ones are the electrical and the mechanical methods, which have been the most investigated.

The main advantages of the electrical reconfigurability are the maturity of the technology and the low-loss while considering the RF-MEMs. Nevertheless, its integration is complex and shows low reliability. On the contrary, the mechanical reconfiguration does not lie on the use of switches. Thanks to that, it has lower complexity and better reliability. Nevertheless, the issues are the slow response, the cost, the size, and the weight, which depends on the many parameters such as the number of actuators and the control of the deformation.

1.3.6 Multi-objective optimization

The studies made about re-shapeable reflectors prove that enhancing the RF coverage and maintaining low levels of deformations constitute conflicting objectives, and their simultaneous improvement must deal with Multi-objective Optimization.

Running multiple optimizations and balancing the importance between mechanical and RF performance will produce a set of optimization solutions for which an improvement of RF performance necessarily conduces to a high curvature of the reflector.

In mechanical sight, the literature underlines several problems in terms of engineering aspects. The essential objective of the compound material design for a reflector morphing skin is the re-shaping ability in a relatively large magnitude with high surface accuracy. As side objectives, the required re-shaping energy shall be possibly low, the material failure and the structural instability shall also be avoided. Moreover, the re-shaping behavior of a reflector morphing skin is determined by various parameters from material properties, geometry, and boundary conditions.

The reconfiguration concept proposed in this thesis is inspired by these studies. Hence, it is based on the concept of re-shapeable reflector mixed with the good features of *RA*. By combining these two technologies, the goal is to be able to provide multiple configurations with high RF performance while minimizing the deformation and optimizing the prediction and the control of the ground plane's shape.

1.4 Reconfiguration concept proposal

1.4.1 Description

In this thesis, we propose a derived solution where the ground plane of a reflectarray is made from a flexible membrane that can be deformed thanks to mechanical actuators. The reconfiguration capability relies on the control of the reflected

phase of each reflecting element over the panel by the control of the distance between each cell and the ground plane. This distance is tuned thanks to the action of actuators (cf. Figure 1.27).

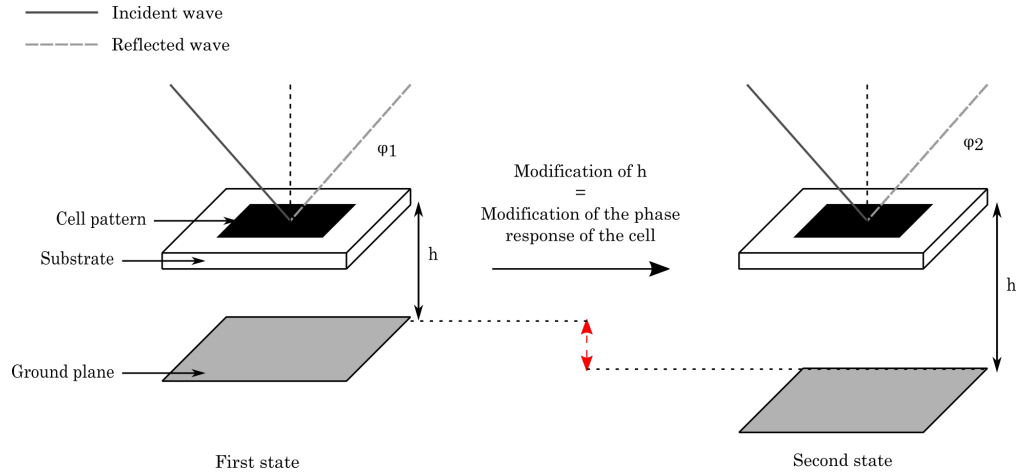


FIGURE 1.27: Schematic view of the concept at the cell level.

As illustrated in Figure 1.28, actuators are placed under the ground plane to provide specific displacements and rotation to shape the membrane to modify the radiation pattern.

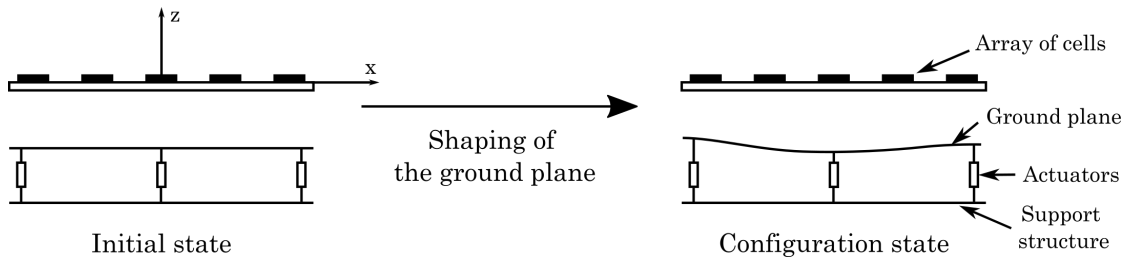


FIGURE 1.28: Concept proposal.

At the cell level, the structure considered is presented in Figure 1.29.

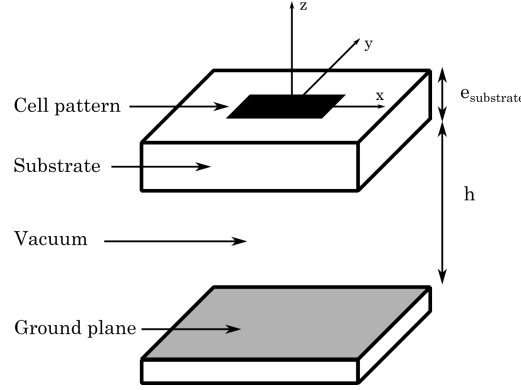


FIGURE 1.29: Structure of the radiating element.

In conclusion, the accuracy of the actuators displacements determines the performance of the flexible membrane shaping, which induces the quality of the radiation pattern. The RF performance are so not only dependent on the shaping but also on the selection of the reflecting elements. The good prediction of the phase response of the cells printed on the reflectarray versus the distance noted h is then necessary in order to design the panel correctly.

1.4.2 Study issues

The design of the mechanically reconfigurable reflectarray with a flexible ground plane is challenging considering the RF and the mechanical aspects. The main issues of the *RRA* design are the modelization of the cells versus the distance to the ground plane (noted h) and the design methodology to apply while ensuring a good balance between the RF and the mechanical requirements. To evaluate this, it is necessary to create an RF model of the reflecting elements which gives the impact of the distance to the ground on their phase response with good accuracy and a mechanical model for the prediction of the flexible ground plane shape.

Past studies on mechanically reconfigurable reflectors have shown the difficulty of finding the best compromise between the RF performance and the mechanical ones [125]. Indeed, the real impact of the actuators on the membrane and the identification of the exact shape is complex to predict with good accuracy. Consequently, the RF and mechanical simulations is essential to optimize the design.

1.5 Conclusion

This chapter introduces the notion of reflectarray antenna, which is a combination of two existing types of antennas: reflectors and arrays. A description of both technologies is presented in the first section.

RAs consist of a flat panel covered by multiple printed elements that re-radiate the incident field in a targeted direction. The goal of those elements is to compensate for the phase delays introduced by the planarity of the panel compared to the curved surface of a reflector. Hence, the selection of the elements is therefore, an essential step in the design and optimization process of the *RA*.

Considering the fast growth of the telecommunication market and the interest in dynamically modify the coverages in-orbit, reconfigurable *RA* concepts have been detailed in the literature. This thesis proposes a mechanical reconfiguration of *RA*. Indeed, the control of the reflected phase of the cells is made by tuning the distance between each reflecting element composing the panel and the flexible ground plane thanks to actuators.

As for the *RA*, the good selection of the reflecting elements is essential to ensure maximal RF performance. In Chapter 2, a semi-analytical tool is developed and detailed. It is used to create a database that makes the link between the distance to the ground plane, the geometry of the cell, and its reflection phase.

Chapter 2

Modeling and analysis of cells with tunable height

Contents

2.1	Introduction	38
2.2	Modeling tool	39
2.2.1	Objectives and hypothesis	39
2.2.2	Semi-analytical model	40
2.2.3	Full-wave validation	42
2.3	Impact of h on the reflected phase	47
2.4	Impact of an error on h	49
2.5	Impact of h on the frequency dispersion of the cells	51
2.6	Conclusion	55

2.1 Introduction

Chapter 1 introduced the Reconfigurable Reflectarray (*RRA*) with a flexible ground plane inspired by the re-shapeable reflector developed in [39] and [41]. The coverage flexibility of this re-shapeable reflector is allowed by the mechanical deformation of its shape thanks to actuators placed below it. The concept of a *RRA* with a flexible ground plane consists of a RA with a deformable ground plane controlled by actuators placed under it. Varying the distance between the substrate and the ground plane, noted h , induces the modification of the phase response of each cell composing the RA panel and so, the reconfiguration of the radiation pattern.

In the view of designing a RA based on this proposal, the modeling of a cell at a given frequency for a tunable distance h is mandatory to extract its phase response. This is possible with full-wave simulations but this can be time-consuming, especially if a complete database of reflecting elements is needed to create the RA panel.

The first section details a semi-analytical model which gives the phase response of a cell (also called the phase produced by the cell) at a given frequency for various values of h . The phase response computed using the tool must be accurate enough while reducing computation time.

The second section presents the reflecting elements' behavior, which leads to their classification regarding a variable value of h . Only the second-order Phoenix cells type is studied due to their good features reminded in Chapter 1.

The non-linearity of the phase response of the cells versus h highlighted in this chapter, associated with the non-ideal deformation of the membrane induced by the mechanical actuators, introduces the problem of the impact of a position error in the reconfiguration capability of the concept. This issue is presented in the third section while the impact of h on the frequency dispersion of the cells is detailed in the last one.

2.2 Modeling tool

2.2.1 Objectives and hypothesis

The objective of the semi-analytical modeling tool is to accurately compute the phase response of a cell while reducing the computation time compared to one full-wave simulation. The structure of the radiating elements is detailed in Figure 2.1

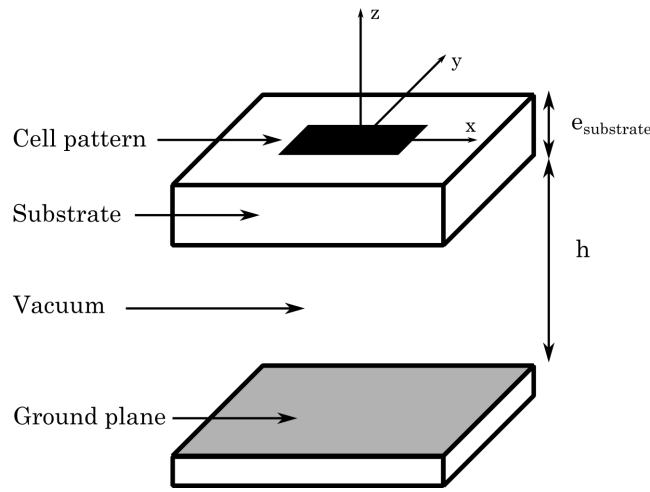


FIGURE 2.1: Structure of the radiating element.

The methodology follows two steps. First, the cell is simulated with a full-wave simulation on HFSS software, assuming periodicity and normal incidence to calculate the S matrix without considering the ground plane.

Secondly, an equivalent electrical model such as in [126] and [127] is used to compute the reflected phase analytically considering the distance h and a ground plane perfectly parallel to the plane of the cell.

The full-wave model is applied to one fixed configuration of reflecting element where h does not vary. In the case of the *RRA*, the deformation of the ground plane is the basis of the concept. Hence, the reflected phase of each cell composing the database must be computed for numerous values of h . Consequently, the semi-analytical tool primary purpose is to allow an efficient reduction of the computation time compared to multiple full-wave simulations needed to extract the reflected phase considering the desired values of h .

2.2.2 Semi-analytical model

2.2.2.1 HFSS model

For this first step of the methodology, a full-wave simulation using HFSS is done considering a reflecting element without ground plane (cf. Figure 2.1). It assumes periodicity and normal incidence. The scattering matrix (S matrix) is extracted thanks to this model at a given frequency.

The coordinate system for the model and the setup of the electromagnetic simulation applied to the structure are illustrated in Figure 2.2.

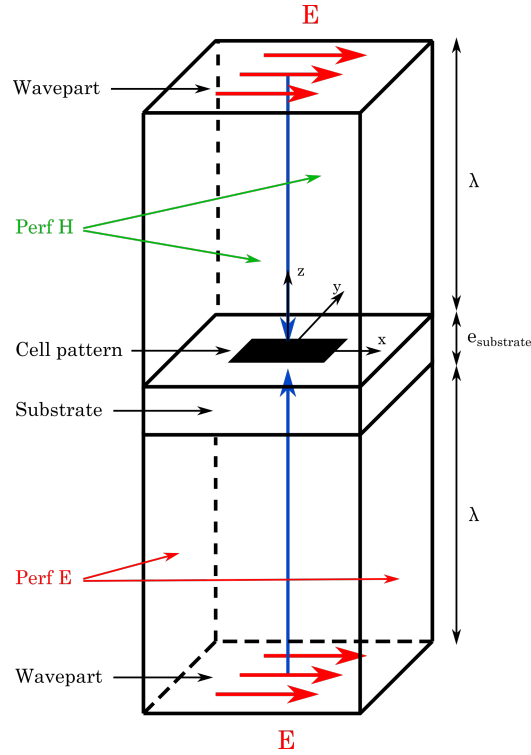


FIGURE 2.2: Representation of the Ansys HFSS Setup for the reflecting element structure. Note: PerH (Perfect Magnetic Boundary), PerE (Perfect Electric Boundary).

As shown in Figure 2.2, the model aims to extract the scattering matrix of the substrate with the printed pattern placed in an airbox with periodic boundaries and illuminated with a plane wave under normal incidence. The boundary conditions are assimilated to perfect electric and magnetic conductors.

Two waveports are placed at the extremities of the simulated environment and correspond to the excitation of the incident wave transmitted through the structure. The reference planes are the surface of the substrate on which the cell pattern is printed and the bottom of the substrate.

Moreover, two waveports are placed at a distance equal to λ_0 over the structure so that they are far enough to neglect higher order evanescent modes in the near field of the cell. By exciting each wave port individually to solve the model, S-parameters are extracted from the HFSS simulation.

2.2.2.2 Equivalent electrical circuit model

Once the S-parameters of the substrate and the printed pattern are extracted from full-wave simulation, the second step of the methodology uses an equivalent Electrical Circuit (*EC*) model to represent the structure illustrated Figure 2.1. The objective is then to determine the phase response of the cell for a given distance h at one frequency.

Figure 2.3 illustrates the *EC* of the radiating element considering the S-matrix. The air between the substrate and the ground plane is assimilated to a transmission line of a length equal to the distance h . Moreover, the ground plane is represented by a short-circuit at the distance h which loads the transmission line.

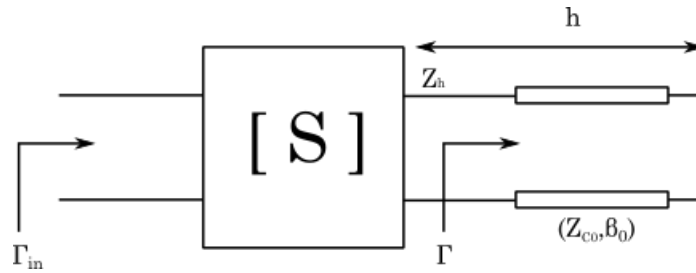


FIGURE 2.3: EC of the radiating element with S matrix.

In Figure 2.3, Γ_{in} is the global reflection coefficient, and Γ is the reflection coefficient at the input of the transmission line corresponding to the air between the ground plane and the substrate. The characteristics of the transmission line are Z_0 its characteristic impedance, β_0 its wave number and are computed thanks to the equations 2.1 and 2.2 (λ_0 the wavelength, μ_0 the permeability of the air, ϵ_0

the permittivity).

$$Z_0 = \sqrt{\frac{\mu_0}{\epsilon_0}} \quad (2.1)$$

$$\beta_0 = \frac{2\pi}{\lambda_0} \quad (2.2)$$

Thanks to Figure 2.3 the relation between Γ_{in} and Γ , using the S-parameters (S_{11} , S_{12} , S_{21} , S_{22}) extracted, could be written such as in the equation 2.3 :

$$\Gamma_{in} = S_{11} + \frac{S_{12}S_{21}\Gamma}{1 - S_{22}\Gamma} \quad (2.3)$$

The reflection coefficient of the space between the substrate and the ground plane can be computed knowing the input impedance when loaded by the ground plane at h (Z_h) and the characteristic impedance Z_0 . Equations 2.4 and 2.5 show that the modification of the distance between the cell and the ground plane directly impacts the value of Γ as it is illustrated in Figure 2.3.

$$\Gamma = \frac{Z_h - Z_0}{Z_h + Z_0} \quad (2.4)$$

The input impedance when loaded by the ground plane at h could be computed with equation 2.5.

$$Z_h = jZ_0 \tan(\beta_0 h) \quad (2.5)$$

In conclusion, by changing the value of h in Equation 2.5 it is possible to compute Γ . Using equation 2.3, the global reflection coefficient Γ_{in} is computed, and the phase response as a function of h of the elements is derived.

2.2.3 Full-wave validation

The validation of the semi-analytical model developed is carried out by comparing the result with full-wave simulation. As for the first step of the developed methodology, the structure is placed in an infinite array of identical elements and illuminated with a plane wave of normal incidence. Nevertheless, the validation

model considers a ground plane assimilated to a perfect conductor and only one waveport. Figure 2.4 illustrates the setup of the HFSS simulation.

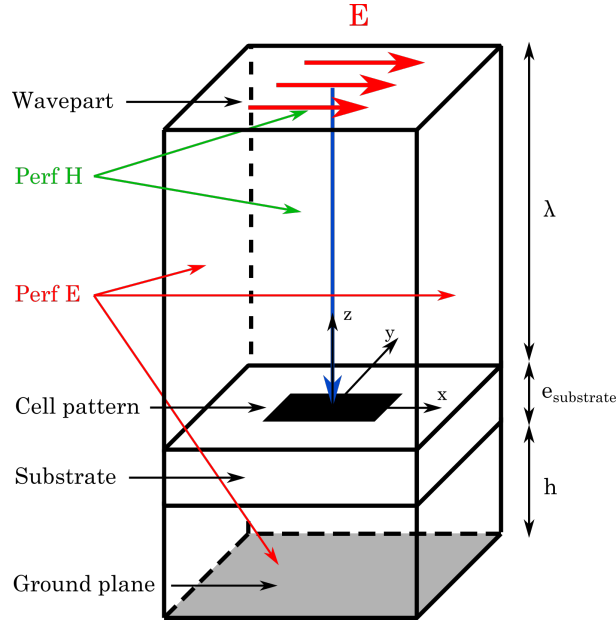


FIGURE 2.4: Phoenix cell simulation setup in Ansys HFSS.

The validation model extracts, at a single frequency, the reflected phase of the cell for various values of h between 0 and $\lambda_0/2$ with a step of $0.01\lambda_0$. Following the choice of the type of cells used, the presented test cases are applied on capacitive and inductive Phoenix cells of various orders. Figure 2.5 is a picture of the geometric parameters of the cells used [128].

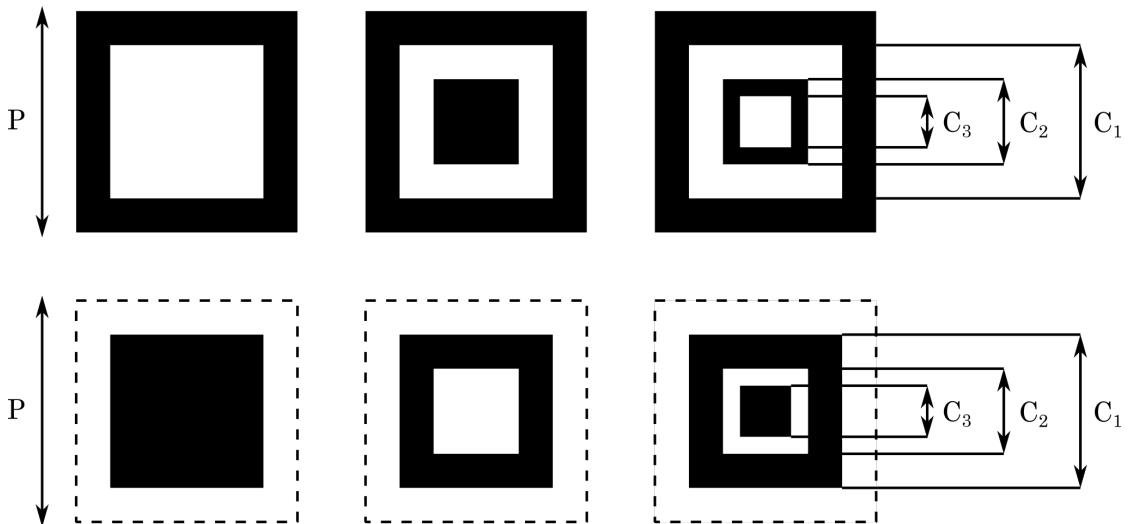


FIGURE 2.5: Phoenix cells geometrical parameter for first, second and third order (left to right) capacitive (bottom) and inductive (top).

For the sake of clarity, two validation cases are shown in this section at the frequency $f=12.5$ GHz¹. Both are second-order Phoenix cells printed on the same substrate (thickness, $e=0.5$ mm and permittivity $\epsilon_r=2.2$), but one is inductive, and the second one is capacitive. The geometrical parameters (cf. Figure 2.5) of the cells studied are reminded in the captions of the figures.

Figures 2.6 and 2.7 present the impact of the distance h on the reflected phase respectively for the capacitive and inductive cells. The Matlab results correspond to the semi-analytical tool, whereas the HFSS ones to the full-wave simulations. For both types of simulation, the same h values are tested ($h \in [0; \frac{\lambda_0}{2}]$ with a step of 0.01 mm).

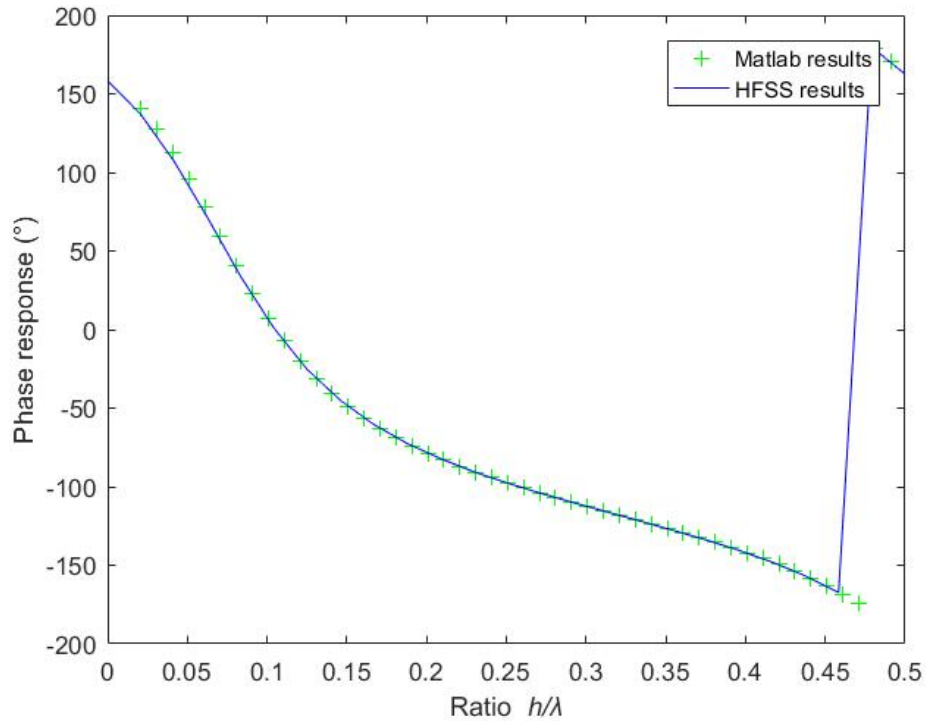


FIGURE 2.6: Capacitive 2nd order Phoenix cell: $P = 11.7mm$, $C_1 = 4.4mm$, $C_2 = 3.8mm$ at $f = 12.5GHz$.

¹This frequency has been taken as an example from Thales Alenia Space typical Ku band space applications

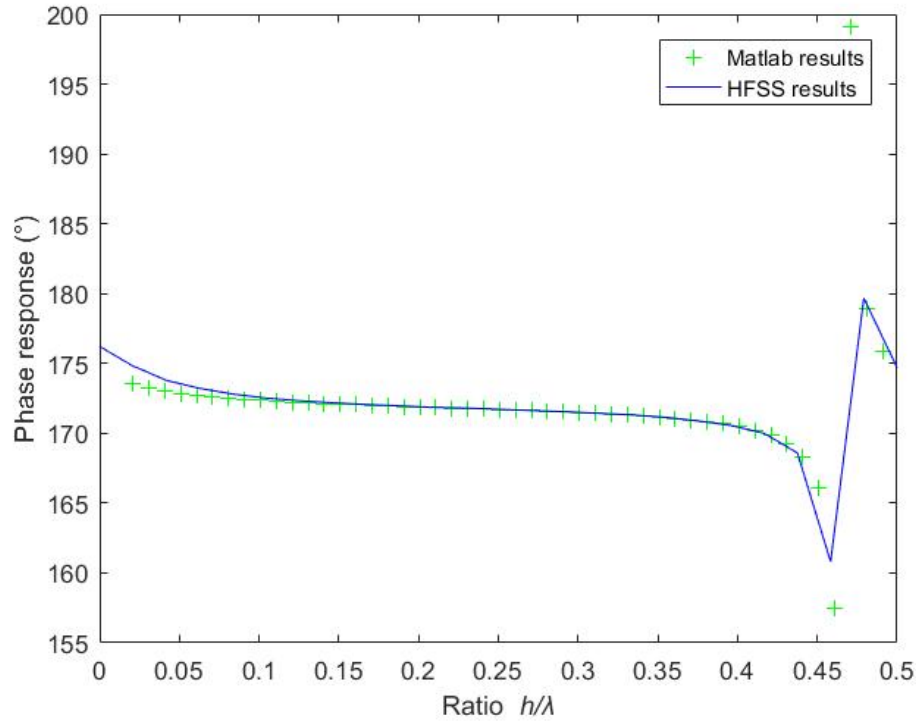


FIGURE 2.7: Inductive 2nd order Phoenix cell: $P = 11.7mm$, $C_1 = 4.4mm$, $C_2 = 3.8mm$ at $f = 12.5GHz$.

In Figures 2.6 and 2.7, the high correlation of the results obtained with the semi-analytical tool compared to the full-wave ones can be noticed. The average phase error between the Matlab results and the HFSS ones for the whole panel of h values is around 1° . We can see that the agreement gets a bit worse when the ground plane is very close to the cell (h is almost equal to zero), which is logical due to possible coupling between the cell and the ground plane.

As mentioned before, the main idea of this tool is to propose an accurate model of the reflecting element with low computation time. Figures 2.6 and 2.7 show that the developed model presents similar result to the full-wave one.

Tab A.1 gives the time consumption of each method. Tab A.1 shows that the model developed presents an important gain of time compared to the full-wave simulation.

	Full-wave	Semi-analytical
Average computation time	101 min 22 s	1 min 19 s

TABLE 2.1: Time consumption of each methodology

The modeling tool presents excellent features such as a low average phase error (inferior to 1°) and a reduced computation time compared to the full-wave simulation. Indeed, the approximation of the reflected phase for a given h at a single frequency is good, whereas the computation time is greatly reduced.

2.2.3.1 Reflecting elements database

This section aims to introduce a possible reflecting elements database that will be used in the next chapter to design the *RRR*. Consequently, the frequency is now set at 12.85GHz. The database is only composed of second-order inductive Phoenix cells modeled.

As explained in Chapter 1, Phoenix cells are the best candidates considering their rebirth capabilities and their RF performance. Using only one type of cells with various geometries is sufficient to build a strong database. Moreover, it is important to note that the limitation of the number of cells is appreciated as it reduces the number of combination possibilities for the layout.

Finally, the defined database is composed of 114 cells (with the same substrate) whose geometrical parameters are described in Figure 2.8. The thickness of the substrate is equal to 0.5 mm with a permittivity of 2.2.

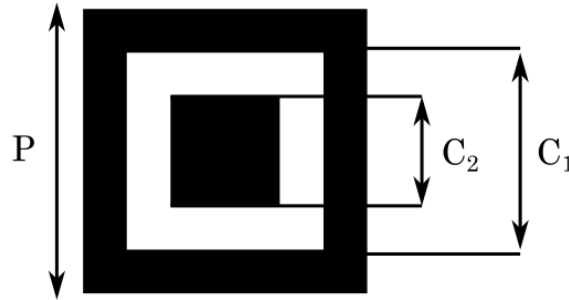


FIGURE 2.8: Geometrical parameters of the reflecting elements.

The set of cells modeled includes the following geometries (see Figure 2.8):

- $C_2=0.6$ mm and $C_1 \in [0.8; 5.8]$ mm with a step of 0.2 mm
- $C_2=6.0$ mm and $C_1 \in [6.2; 11.2]$ mm with a step of 0.2 mm

- $C_1=0.6+C_2$ mm and $C_2 \in [0.2; 5.2]$ mm with a step of 0.2 mm
- $C_1=6.0+C_2$ mm and $C_2 \in [0.2; 5.2]$ mm with a step of 0.2 mm
- $C_1=8.0+C_2$ mm and $C_2 \in [0.2; 3.2]$ mm with a step of 0.2 mm

2.3 Impact of h on the reflected phase

The knowledge of the cells' behavior for the selection of the reflecting elements of the RA panel is important in the context of our concept proposal. Three elements must be considered:

- The deformation of the membrane will not be perfect and depends on the control accuracy.
- The deformation must be smooth, and its magnitude minimized to respect the characteristics of the material.
- The deformation of the membrane must consider the inter-dependency of distances h for every cell over the panel for each configuration. Indeed, the slope of the membrane between two consecutive cells is limited by the material characteristic. Hence, it can be deduced that two consecutive cells must present similar behavior.

Equation 2.6 presents the existing relation between the distance h , the normalized admittance associated with the cell $Y_{cell} = jb$ of the cell, and its phase ϕ in the case of no substrate is considered. Equation 2.6 is deduced from the Figure 2.9 which is a representation of the EC with no substrate considered.

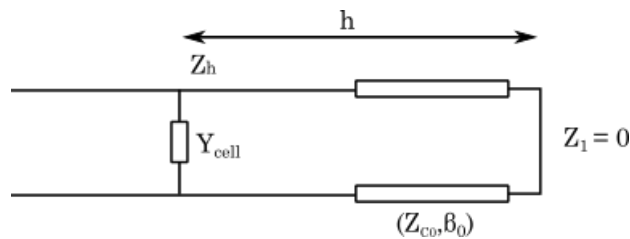


FIGURE 2.9: EC of the radiating element without substrate.

$$h = \frac{1}{\beta_0} \tan^{-1} \left(\frac{1}{b + \tan \left(\frac{\phi}{2} \right)} \right) \quad (2.6)$$

Figure 2.10 illustrates three examples of capacitive Phoenix cells modeled with the semi-analytical tool at $f=12.85$ GHz.

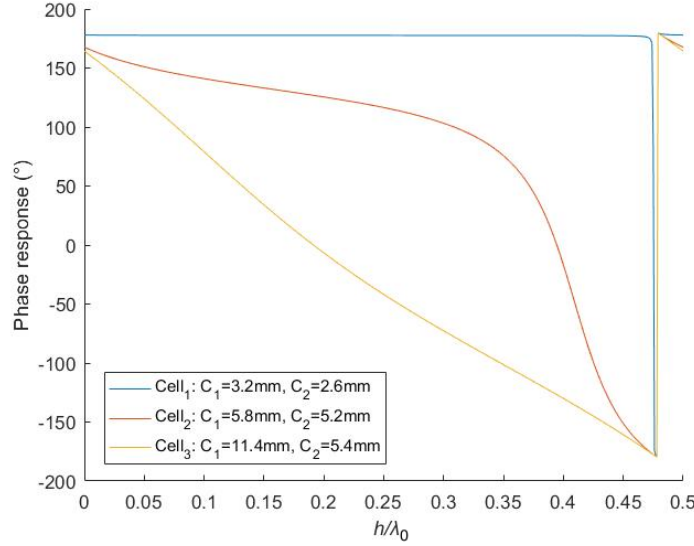


FIGURE 2.10: Capacitive 2nd order Phoenix cells: $P = \frac{\lambda_0}{2} = 11.7mm$.

Equation 2.6 presents the non-linearity between the reflected phase and the distance h . This relation between the reflected phase versus $\frac{h}{\lambda_0}$ is illustrated in Figure 2.10.

In Figure 2.10, the phase response of $Cell_1$ is constant for the quasi totality of the $\frac{h}{\lambda_0}$ values until a given distance (approx. $\frac{h}{\lambda_0}$ equals to 0.47 in this example) where an abrupt variation of the phase happens. Indeed a 360° phase cycle is realized for a $\frac{h}{\lambda_0}$ range inferior to 0.003 (approx. $h=0.07$ mm).

$Cell_2$ presents a smoother variation of phase versus $\frac{h}{\lambda_0}$. At the lower values of $\frac{h}{\lambda_0}$, the reflected phase decreases slowly with a variation of $\frac{h}{\lambda_0}$ between 0 and 0.35. After this value, the variations are much quicker.

The third cell, $Cell_3$, presents a quasi-linear variation of the reflected phase versus $\frac{h}{\lambda_0}$.

To summarize, if one cell of the RA panel does not need to provide a medium or high variation of phase, the $Cell_1$ is the best option because of its low sensitivity

to h variation. Nevertheless, it is not the case for the higher values of $\frac{h}{\lambda_0}$, typically close to 0.475 and 0.48.

On the contrary, $Cell_3$ has the main advantage of having a quasi-linear behavior versus h . The interest of using this type of cell is that the variation of h is large between two configurations or two consecutive cells. Finally, $Cell_2$ is a good compromise compared to the other cells when a medium variation of phase is needed. Indeed, $Cell_2$ presents a variable sensitivity to h variation in function of the $\frac{h}{\lambda_0}$ reference value which allows more versatility in the layout design process.

The selection of the cells is then the first important step in optimizing RF and mechanical performances for the design of a RA.

2.4 Impact of an error on h

The concept proposed in this thesis is based on the mechanical reconfiguration of the reflectarray by deforming the ground plane (or shell-membrane) mechanically with actuators. Those control the shape of the ground plane, whose deformation accuracy directly impacts the RF performance of the antenna. Indeed, in the real case the deformation is not the same as the ideal, notably due to the actuators' precision. Due to that, the impact of an error on h must be investigated.

To evaluate the impact of an error on the deformation (at a cell level, it could be considered as an error on h), a random error arbitrarily taken between $\pm 0.2\text{mm}$ is added on a reference height (noted h_0 and included in $[0; \frac{\lambda_0}{2}]$). To have a representative overview of this impact on the different types of cell, the three types of geometry tested in the last section are used.

The absolute difference between the phase response obtained with this error applied ($\phi_{h_0}^n$) and the phase response at h_0 (noted ϕ_{h_0}) is computed. For each value of h_0 , the routine is made 300 times with a new error at each iteration (noted n). For each value of h_0 , an average value of the 300 values is computed to obtain a representative average phase error using the semi-analytical tool. This average phase error at h_0 , noted $\epsilon_{h_0}^-$ is computed using Equation 2.7.

$$\epsilon_{h_0}^- = \sum_{n=0}^{300} \frac{|\phi_{h_0} - \phi_{h_0}^n|}{300} \text{mod}(2\pi) \quad (2.7)$$

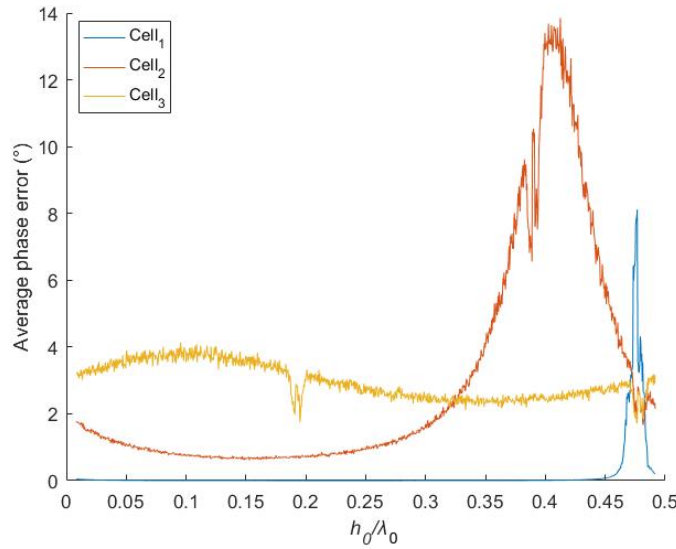


FIGURE 2.11: Impact of an error of position on the phase response versus the reference distance.

Figure 2.11 illustrates the average phase error $\epsilon_{h_0}^-$. It can be noticed that the impact of an error of position is dependent on the reference height, noted h_0 . Tab 2.2 gathers the average phase error for three reference distances between the substrate and the ground plane. These are computed with $h_1 = 1.5mm$ ($\frac{h}{\lambda_0}=0.06$), $h_2 = \frac{\lambda_0}{4}$ ($\frac{h}{\lambda_0}=0.25$), $h_3 = 10mm$ ($\frac{h}{\lambda_0}=0.41$) (cf. Tab 2.2) .

	$Cell_1$	$Cell_2$	$Cell_3$
h_1	0°	1°	4°
h_2	0°	1°	3°
h_3	0°	12°	3°

TABLE 2.2: Impact of a position error on the phase response of a cell

Figure 2.10 and Tab 2.2 show that the impact of an error of position on the phase response of the cell is not constant for all values of h , but it is also dependent on the geometry of the reflecting element.

As the last section shows, the reflected phase of $Cell_1$ is constant for most of the h values and suddenly sensitive to a variation of h . This explains the quasi-null average phase error and the peak around a specific value of h . The correlation between the behavior and this peak can be noticed in Figure 2.10 and Figure 2.11 for $\frac{h}{\lambda_0}$ or $\frac{h_0}{\lambda_0}$ equal to 0.47.

The overall constancy of the average error for $Cell_2$ is explained by the low variation of its phase compared to the variation of h . In Figure 2.10, this behavior changes around $\frac{h}{\lambda_0}=0.35$ mm where the cell becomes more sensitive to a variation of h . Figure 2.11 shows a low sensitivity of an error of h up to this value.

The quasi-linearity of $Cell_3$ illustrated in Figure 2.10 explains the approximated constancy of the average phase error shown in Figure 2.11.

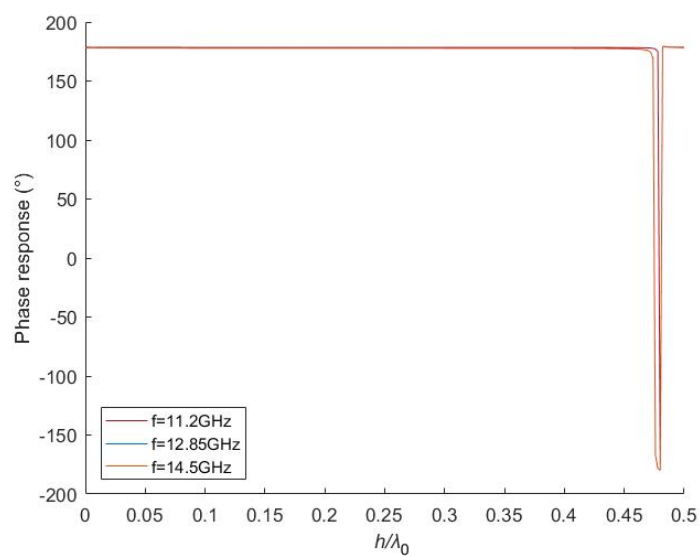
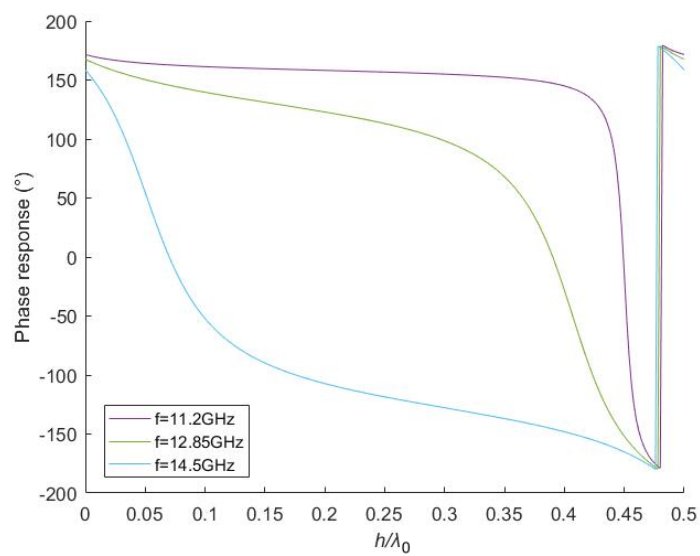
Finally, cells with the same behavior versus h as $Cell_1$ are interesting to minimize the deformation because a big phase variation is provided by a low distance variation. Nevertheless, while its sensitivity to the variation of the distance is high, an error on h leads to an important phase error and so to a degradation of the RF performances. In the contrary, $Cell_3$ needs a big variation of h for an high phase variation. Consequently, $Cell_2$ seems to be the best compromise if the problematic values of h are avoided.

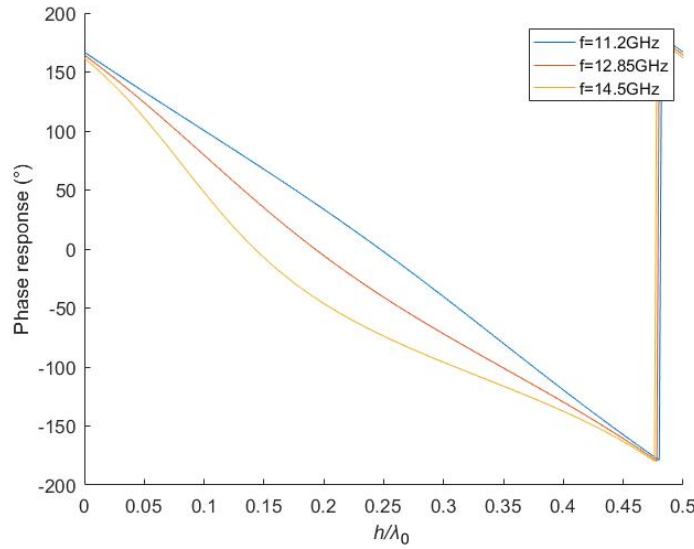
2.5 Impact of h on the frequency dispersion of the cells

The application of the mechanically *RRA* presented in this thesis considers a frequency band. The impact of the distance between the cell and the ground plane, noted h , on the frequency dispersion of the cells is important to investigate. As presented in Chapter 1, the Phoenix cells are supposed to have low dispersion. In this section, this characteristic of the reflecting element will be studied when h is varying.

The same cells' geometries, as for the last sections, are used in this analysis. The values of each geometrical parameters are reminded in the caption of the figures, and the wavelength is computed for the central frequency 12.85 GHz. The behavior of each cell is simulated at 11.2 GHz, 12.85 GHz, and 14.5 GHz using the semi-analytical tool.

Figures 2.12, 2.13 and 2.14 illustrate the phase response of each cell studied in function of the distance h at three frequencies.

FIGURE 2.12: Impact of the frequency on the phase for $Cell_1$.FIGURE 2.13: Impact of the frequency on the phase for $Cell_2$.

FIGURE 2.14: Impact of the frequency on the phase for $Cell_3$.

Figures 2.12, 2.13 and 2.14 show a similar effect of the frequency on the phase for all values of h . The phase response decreases with the frequency for a given $\frac{h}{\lambda_0}$. $Cell_1$ and $Cell_3$ present the same profile versus h for all frequencies whereas it is not the case for $Cell_2$.

The average frequency dispersion over the frequency band is the ratio of the absolute value of the difference between the phase response at the maximum frequency and the phase response at the minimum frequency of the cell (noted ϕ_{max} and ϕ_{min}) over the frequency range.

$$\frac{\Delta\phi}{\Delta f} = \frac{|\phi_{max} - \phi_{min}|}{f_{max} - f_{min}} \quad (2.8)$$

In this case, $f_{max}=14.5$ GHz, whereas $f_{min}=11.2$ GHz. Figures 2.12, 2.13 and 2.14, show that the dispersion is dependent on the distance h and on the behavior of the cell.

$Cell_1$ is the less dispersive cells studied except close to 0.47 where it is the contrary. As in Figure 2.12, the phase response of the cell is not sensitive to a variation of h or to the frequency. Nevertheless, the phase response of $Cell_2$ and $Cell_3$ varies with h but also with the frequency. Moreover, $Cell_2$ is the most dispersive one and seems to present its maximum at low or high values of h (or $\frac{h}{\lambda_0}$).

Figure 2.15 illustrates the frequency dispersion modulo 2π computed for $\frac{h}{\lambda_0} \in [0; 5]$, so for $h \in [0; \frac{\lambda_0}{2}]$

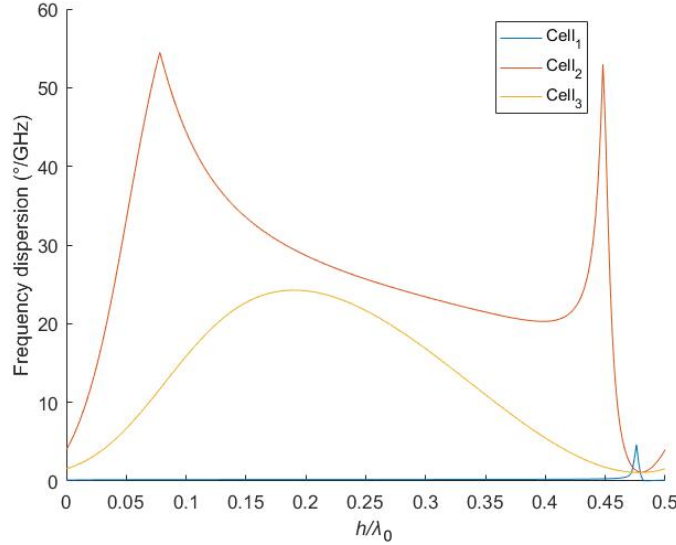


FIGURE 2.15: Impact of h on the frequency dispersion.

Tab 2.3 gathers the maximal average frequency dispersion over the frequency band of each type of cell tested considering the whole range value of h .

$Cell_1$	$Cell_2$	$Cell_3$
5°	55°	24°

TABLE 2.3: Maximal frequency dispersion for $h \in [0; \frac{\lambda_0}{2}]$

The information given Tab 2.3 and Figure 2.15 confirms the comments made before on the high dispersivity of $Cell_2$ compared to $Cell_1$ or $Cell_3$. Hence, Δf at a given h must be a new parameter to consider for the design of the panel and the identification of the needed deformations. Indeed, if the selected cell has the same behavior as $Cell_2$ and needs a deformation at low or high h to achieve the wanted phase at the central frequency, it leads to an important phase error in other frequencies, degrading the RF performances.

Gathering the information given in Figures 2.10, 2.11 and, 2.15, the importance of three parameters are underlined by the three behaviors associated with the examples: the geometry of the cell, the reference h and the Δf at a given h .

- *Cell*₁ has a constant phase response versus h up to a specific value of h , which makes it not particularly interesting in the case of a deformable ground plane. Indeed, even though the phase variation is low sensitive to an error on the distance, it gives few degrees of freedom in terms of deformations and phase response. Nevertheless, this cell has the advantage of being low-frequency dispersive.
- *Cell*₂ has a smooth variation of its phase response compared to the h one, but it is more dispersive. It also presents the highest average phase error in the case of position error at a given h . Nevertheless, big phase variations could be achieved with low distance shifts, which is an advantage. Figure 2.11 shows that even it has the biggest average phase error at a wide range of h values, this error is acceptable.
- *Cell*₃ presents a quasi-linear variation of its phase response versus h and its maximal frequency dispersion is a good compromise between the ones of *Cell*₁, and *Cell*₂. Moreover, its average phase error over all possible values of h stands around 4° , however big phase variation will need big h shifts. The constraints applied to the flexible membrane would then be important.

Finally, each element composing the reflectarray panel needs to be selected considering the pros and cons derived from their behavior versus the distance h .

2.6 Conclusion

The concept proposal presented in this thesis is based on the mechanical reconfiguration of reflectarray antenna by modifying the ground plane's shape. Hence, the first issue to design the reflectarray panel is to understand how the reflecting elements react when the distance between the substrate and the ground plane (h) is modified.

To model the impact of h on the phase response at a single frequency for a given cell, full-wave simulations can be used even if they are time-consuming. This section aims to develop an accurate semi-analytical tool which reduces the computation time of a reflecting element simulation at a given frequency.

The validation of the tool reveals an average phase error compared to the full-wave simulations inferior to 1° for a time cost highly reduced.

The understanding of the cells' behavior is useful for the selection of the cells in the design methodology of a final RA panel. The impact of h on the phase response and the frequency dispersion have been studied. The analysis of the behavior of the cells leads to the classification of the reflecting elements in three categories represented by three examples $Cell_1$, $Cell_2$ and, $Cell_3$.

In conclusion, this chapter underlines the importance of the good selection of the cells for the design of the RA. Indeed, the distance between the cell and the ground plane has a significant impact on its phase and its frequency dispersion. Moreover, those are also dependant on the geometry of the cell. A compromise between the RF and the mechanical performances to avoid significant phase error or too high distance variation is then necessary.

Using this tool and the knowledge offers by the analysis of the results, a database of cells, and a methodology for the design of the RA panel is presented in the next Chapter.

Chapter 3

Design methodology of a mechanically reconfigurable reflectarray with two configurations

Contents

3.1	Introduction	58
3.2	Objectives and constraints of a mechanically reconfigurable reflectarray	58
3.3	Methodology for a linear reflectarray	60
3.3.1	Development of the methodology	60
3.3.2	Application case	65
3.4	Proposal for improvements	74
3.4.1	Mechanical control and prediction of the ground plane-shape	75
3.4.2	Iteration on the possible set of deformations	84
3.4.3	Final methodology proposal for a linear <i>RRA</i>	89
3.4.4	Validation of the methodology by comparison with full-wave simulations	90
3.5	Conclusion	91

3.1 Introduction

The reconfiguration of a reflectarray antenna (*RRA*) with a flexible ground plane presented in this thesis relies on the principle that it is possible to control the phase response of the reflecting elements by modifying the distance between the substrate and the ground plane (noted distance h in Chapter 2).

In the previous chapter, the modeling and the analysis of reflecting elements behavior versus h were presented. This analysis was performed using the semi-analytical tool developed in the same chapter. The information gathered about the cells helps to define a design methodology for the proposed Reconfigurable ReflectArray (*RRA*).

This chapter aims to step by step develop a design methodology of *RRA* with two radiation pattern configurations, at one frequency, that provides an optimized layout associated with two ground plane shapes. This method is first developed for a linear array antenna considering an ideal control of the ground plane deformations. It is then applied to a test case corresponding to a linear array extracted from a 2D array which will be used in the next chapter.

The developed methodology is discussed to identify its limitations and to propose some improvements. These modification proposals are tested using the same test case of the linear array. The validation of the defined design methodology is carried out thanks to full-wave simulations performed with HFSS software.

3.2 Objectives and constraints of a mechanically reconfigurable reflectarray

The design methodology aims to identify, at one frequency, the optimal layout associated with two ground plane shapes that provide two different configurations (equivalent to two radiation patterns). Figure 3.1 schematizes this principle.

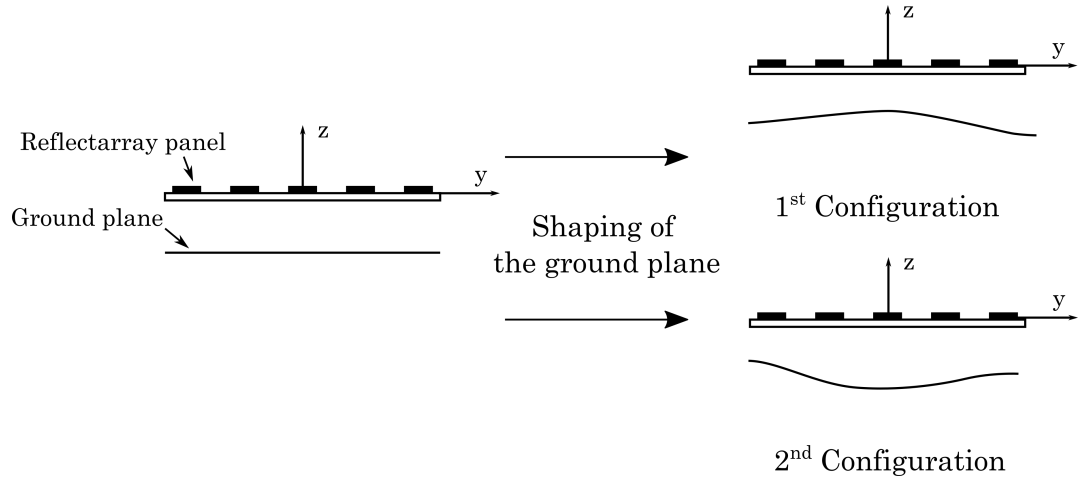


FIGURE 3.1: Concept of the two-configuration *RRA*.

The modification of the ground plane shape could be defined, at the cell level, as a local change of the distance between one cell and the ground plane. This modification of the ground plane shape aims to control the phase response of the cells printed over the *RRA* panel to provide reconfigurability.

Chapter 2 has presented the analysis of the reflecting elements, (*ie.* Phoenix cells [2]). The information deduced from this study of the cells gives a starting point for the creation of a design methodology for *RRA* with a flexible ground plane. The difficulty of implementing this design methodology relies on the existence of various simultaneous and interdependent constraints (RF and mechanical) to take into account.

As introduced in Chapter 1, the control and the prediction of the ground plane shapes are directly linked with the RF performances of the antenna. In other words, the accuracy of the ground plane deformation is linked with the quality of the phase response achieved by the cell.

The principal concerns for the *RRA* design are the initialization of the panel in terms of radiating elements selection, the control, and the prediction of the ground plane shape. Moreover, the solution must minimize the magnitude of the two deformations and the antennas's weight while ensuring acceptable RF performances in terms of directivity patterns for both coverages.

In this chapter, the two targeted configurations are respectively noted S_1 and S_2 and the cells used are the ones composing the database presented in Chapter 2.

Therefore, the local planarity hypothesis of the ground plane under the cell is taken.

3.3 Methodology for a linear reflectarray

The design methodology is developed for a linear array. This section presents the cells selection process and the deformation identification for a linear array composed of M reflecting elements in the case of a two-configuration *RRA*.

3.3.1 Development of the methodology

3.3.1.1 First cell selection

The panel consists of a flat dielectric layer supporting $M = 21$ printed reflecting elements with an inter-element spacing equal to $P = \frac{\lambda_0}{3}$ at a frequency f of 12.85 GHz. The cells could be associated with a normalized admittance $y_m^{S_i}$ for each coverage noted S_i with $i \in [1; 2]$ and m the index of the cell along the panel ($m \in [1; 21]$).

The distance between $Cell_m$ and the ground plane for a given coverage is noted $h_m^{S_i}$. Figure 3.2 illustrates the configuration of the linear panel studied.

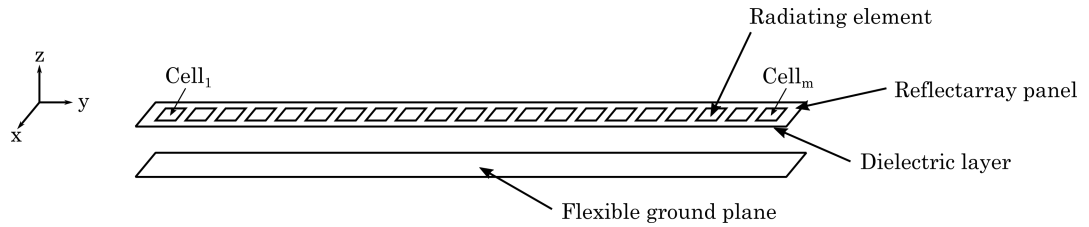


FIGURE 3.2: Linear array configuration.

The Electrical Circuit (*EC*) of the radiating element with no substrate considered is illustrated in Figure 3.3. $\Gamma_{Total}^{S_i}$ is the global reflection coefficient, while $h_m^{S_i}$ is the distance between the cell and the ground plane, and $Z_{lm}^{S_i}$ is the input impedance of the free space transmission line separated $Cell_m$ and the ground plane. Moreover, β_0 is the wavenumber while Z_{c0} is the characteristic impedance of this transmission line.

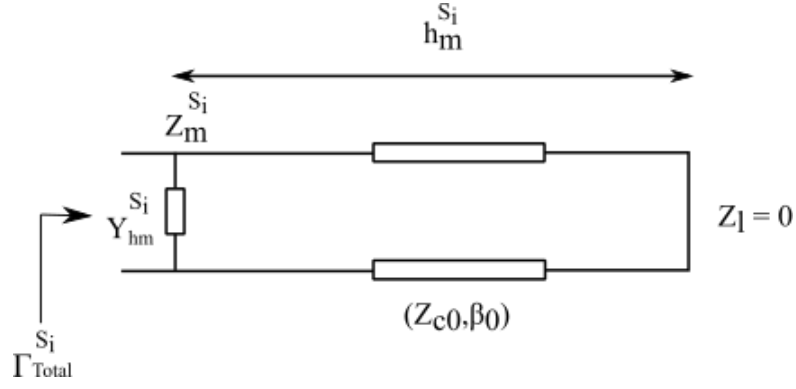


FIGURE 3.3: EC model of the cell without substrate.

Equation 3.1 gives the total normalized admittance $y_{total}^{S_i}$ considering the cell without substrate and a ground plane placed at $h_m^{S_i}$ from it.

$$y_{total}^{S_i} = j[b_m^{S_i} - \cotan(\beta_0 h_m^{S_i})] \quad (3.1)$$

The associated reflection coefficient, noted $\Gamma_{total}^{S_i}$, can be described by Equation 3.2.

$$\Gamma_{total}^{S_i} = \frac{1 - y_{total}^{S_i}}{1 + y_{total}^{S_i}} \quad (3.2)$$

The phase produced by $Cell_m$ can then be deduced (cf. Equation 3.3).

$$\phi_m^{S_i} = 2\tan^{-1}(\cotan(\beta_0 h_m^{S_i}) - b_m^{S_i}) \quad (3.3)$$

The value of the admittance corresponding to one configuration S_i can then be derived from Equation 3.3 considering a ground plane placed at $h_m^{S_i} = \frac{\lambda_0}{4}$. Indeed, Equation 3.4 could be used while $h_m^{S_i} = \frac{\lambda_0}{4}$ as it is considered as the initial state of the ground plane (without deformation).

$$b_m^{S_i} = -\tan(\phi_m^{S_i}/2) \quad (3.4)$$

Then,

$$b_m^{S_i} = \cotan[\beta_0 h_m^{S_i}] - \tan(\phi_m^{S_i}/2) \quad (3.5)$$

with $\phi_m^{S_i}$: the phase response of $Cell_m$ in the configuration S_i .

Deduced from Equations 3.5, the expression of the distance versus the phase response of a cell and its admittance, $h_m^{S_i}$, can be written as follows (see Equation

3.6). Before computing the ideal phase $\phi_m^{S_i}$ of the $Cell_m$, the cell admittance $b_m^{S_i}$ appearing in Equation 3.5 must be found.

$$h_m^{S_i} = \frac{1}{\beta_0} \tan^{-1} \left(\frac{1}{b_m^{S_i} + \tan(\phi_m^{S_i}/2)} \right) \quad (3.6)$$

Considering Equation 3.6 and due to the periodicity of the tangent function, the value of $h_m^{S_i}$ is included between $[0; \frac{\pi}{\beta_0}]$ as it can not be negative. The value of the wavenumber is computed using Equation 3.7.

$$\beta_0 = \frac{2\pi}{\lambda_0} \quad (3.7)$$

This range of $h_m^{S_i}$ values induces possible problematic jumps of $+or - \frac{\lambda_0}{2}$ between two consecutive cells as they represent a significant local magnitude of deformations. This constraint is due to the fact that the magnitude of deformation constrains the choice of the possible material to use. If the magnitude of deformation is too high, it will be complex to find a suitable material.

Furthermore, each cell over the panel must provide a set of two phases $\phi_m^{S_i}$ associated with two distances $h_m^{S_i}$ to provide the two targeted configurations. This variation between $h_m^{S_1}$ and $h_m^{S_2}$ could lead to significant variation of $h_m^{S_i}$ for the reconfiguration. Moreover, as reconfiguration capability is provided considering a deformation of the ground plane, a unique layout for S_1 and S_2 must be found. The proposed solution is then to find a cell with an admittance equal to the average of the two admittances needed for both coverages, $b_m^{S_1}$ and $b_m^{S_2}$, at $h_m^{S_1} = h_m^{S_2} = \frac{\lambda_0}{4}$. Both admittances are given from Equations 3.8 and 3.9 using Equation 3.6.

$$b_m^{S_1} = -\tan \left(\frac{\phi_m^{S_1}}{2} \right) \quad (3.8)$$

and,

$$b_m^{S_2} = -\tan \left(\frac{\phi_m^{S_2}}{2} \right) \quad (3.9)$$

The average admittance b_m^{ave} is given by Equation 3.10.

$$b_m^{ave} = \frac{b_m^{S_1} + b_m^{S_2}}{2} \quad (3.10)$$

For each position m , the reflecting element presenting the closest admittance to b_m^{ave} included in the database is selected. As a reminder, the cells database is detailed in the previous chapter. At this stage, M cells composing the layout are identified. The next step consists in finding the two ideal deformations for S_1 and S_2 .

3.3.1.2 Identification of the ideal deformations

Once a first selection of cells is done, it is possible to derive from Equation 3.6 the ideal distance $h_m^{S_i}$ associated with the phase produced by each selected cell, $\phi_m^{producedS_i}$, at the given frequency.

Using the Equation 3.6 and the value of b_m^{ave} , the derived deformations for S_1 and S_2 can be written as:

$$h_m^{S_1} = \frac{1}{\beta_0} \tan^{-1} \left(\frac{1}{b_m^{ave} + \tan(\phi_m^{producedS_1}/2)} \right) \quad (3.11)$$

$$h_m^{S_2} = \frac{1}{\beta_0} \tan^{-1} \left(\frac{1}{b_m^{ave} + \tan(\phi_m^{producedS_2}/2)} \right) \quad (3.12)$$

By substituting the Equation 3.10 in these equations:

$$h_m^{S_1} = \frac{1}{\beta_0} \tan^{-1} \left(\frac{2}{\tan(\phi_m^{producedS_1}/2) - \tan(\phi_m^{producedS_2}/2)} \right) \quad (3.13)$$

and,

$$h_m^{S_2} = \frac{1}{\beta_0} \tan^{-1} \left(\frac{2}{\tan(\phi_m^{producedS_2}/2) - \tan(\phi_m^{producedS_1}/2)} \right) \quad (3.14)$$

A possible solution is:

$$h_m^{S_1} = -h_m^{S_2} \quad (3.15)$$

Equation 3.15 shows that using the average admittance b_m^{ave} is interesting to select the cells as it leads to two opposite phases for S_1 and S_2 . This symmetry allows the alignment of the peaks of deformations of both curves. This may be advantageous to initialize the distribution of the control points for the ground plane deformation.

3.3.1.3 Reduction of the ideal deformations magnitude

Equation 3.6 can lead to positive and negative values because of the tangent function, whereas only positive ones are correct for the distance $h_m^{S_i}$. The periodicity of the tangent function is then used to find other solutions that are positives. Hence, it is possible to add a distance shift equal to $\frac{\lambda_0}{2}$ to $h_m^{S_i}$ without modifying the phase response of $Cell_m$.

Note that this hypothesis could be taken, but the real impact of this distance shift is not well known in reality and needs further investigations. Nevertheless, jumps can still occur. This could sometimes be canceled thanks to the additional distance shift used previously if it is possible. If it is not, one solution is then to deduce an average phase for the cells printed over the panel.

Indeed, using an average phase, which is the average of the two phases deduced with 3.6 for each coverage for all cells, allows to minimize the phase shift between the two configuration cases. The reduction of this phase shift leads to decrease the variation of h between both configurations, and consequently to avoid high sensitive cells.

Moreover, the average phase is noted $\phi_m^{average}$ for $Cell_m$ and clipped to reduce the magnitude of the deformation and so to reduce the phase range. Indeed, as shown in the previous chapter, huge variations of $h_m^{S_i}$ happen for phase response around $\pm 180^\circ$. Moreover, limited the range of the average phase reduces the possible values of $h_m^{S_i}$. Hence, the limited phase range needs to be wide enough to let flexibility in the selection process and sufficiently small to avoid significant distance variation.

As a first approximation and considering the behavior of the cells presented in Chapter 2, the average phase range value taken is between $\pm 150^\circ$. Indeed, considering the three examples of cells presented in Chapter 2 noted $Cell_1$, $Cell_2$, and $Cell_3$, a big variation of the distance $h_m^{S_i}$ does not necessarily lead to a huge variation of phase $\phi_m^{S_i}$.

Moreover, clipping the average phase sorts the cells to avoid problematic cells which are too sensitive to a significant variation of $h_m^{S_i}$. The analysis developed in Chapter 2 underlines the complexity to control the phase response of some cells ($Cell_1$, Figure 2.12) thanks to the distance $h_m^{S_i}$. These cells are difficult to control with $h_m^{S_i}$ as they partially hide the effect of the ground plane due to being pure

reflecting ones. They are recognizable notably because their phase response is close to $\pm 180^\circ$ for $h_m^{S_i} \in [0; \frac{\lambda_0}{2}]$, this is also why the range is restricted to $\pm 150^\circ$.

Finally, the cells selected are the ones presenting the closest phase response at $h_m = \frac{\lambda_0}{4}$ to the clipped average phase.

3.3.2 Application case

In this section, the developed methodology is applied to a linear array antenna example. This panel is extracted from an existing 2D array, which is described in the next part. The linear array, also called 1D array, corresponds to the central line of this 2D panel.

3.3.2.1 Antenna characteristics

The *RRA* is composed of one offset feed illuminating a square panel of $M \times M$ cells with $M = 21$. The feed is placed at $(0,0,F)$ in (x,y,z) and oriented in the direction of the center of the *RRA* with an angle equal to approximately 17.0° from the z -axis, as Figure 3.4 illustrates it. The coordinates of each cell printed over the panel are written as $(x_{lm}, y_{lm}, 0)$ with l the index of the cell along the x -axis and m along y -axis.

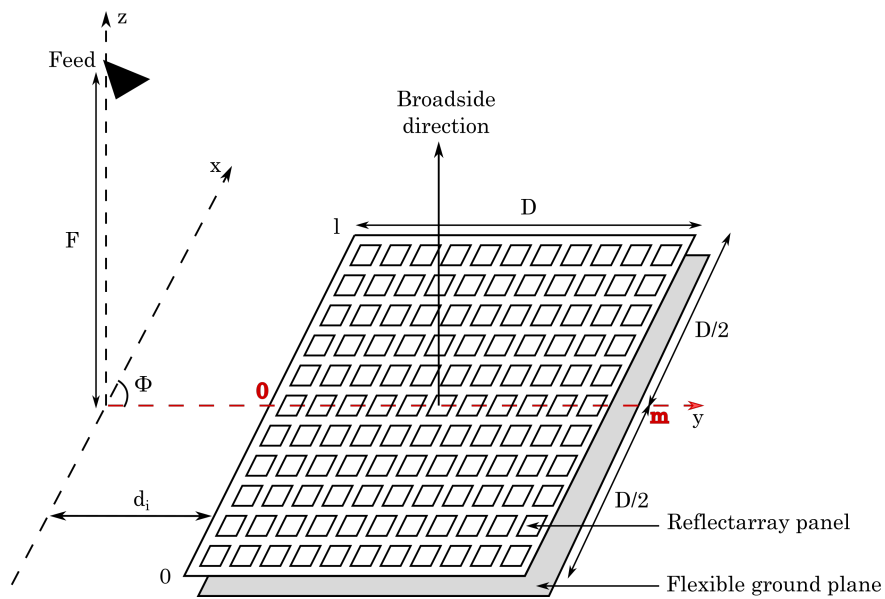


FIGURE 3.4: Antenna configuration.

The array aperture is equal to $D \times D$ whereas $D=21 \times P$ with P the cells lattice ($P=0.5\lambda_0$, λ_0 the vacuum wavelength at f the frequency $f=12.85$ GHz). Finally, $D=245.14$ mm, $P=11.67$ mm, $F=429$ mm, and $d_i=8.37$ mm.

The dimensions of the ground plane are $P \times D \times e_m$ (11.67 mmx245 mmx0.4 mm), with e_m being the thickness of the ground plane.

3.3.2.2 Phase law specification

The methodology has been developed for a linear array. The sample presented in this chapter is extracted from a real application and therefore, only one line of the 2D *RRA* panel example is used (cf. Figure 3.4). In our case, the central line is taken ($x=0$ in our case) and the two configurations are noted S_1 and S_2 and are defined as follows:

- S_1 : a directive beam at 17° from broadside, opposite to the feed in the symmetry plane Ozx
- S_2 : a directive beam at 17° from the broadside such as S_1 with an enlarged beamwidth in the Oyz plane

Figure 3.5 presents the ideal directivity patterns associated with S_1 and S_2 .

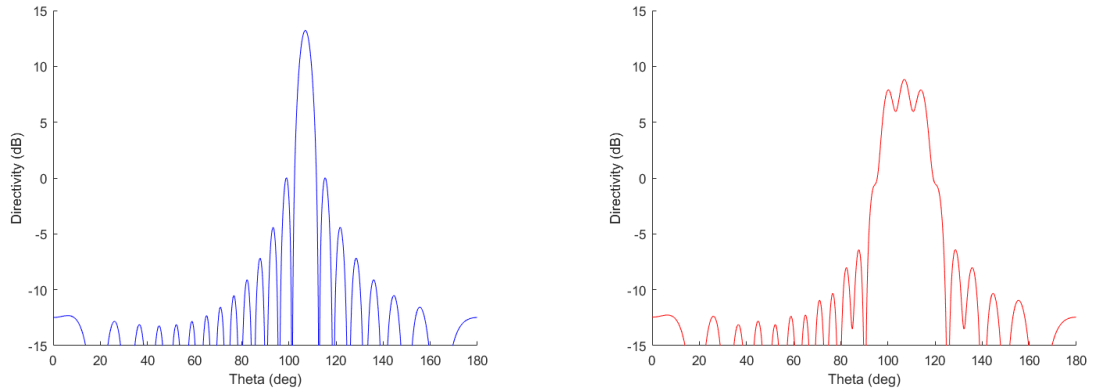


FIGURE 3.5: Ideal directivity patterns for S_1 (left) and for S_2 (right).

3.3.2.3 Identification of the phase introduced by the cells

The phase that each cell m needs to produce for S_1 is noted $\phi_m^{S_1}$. It is equal to the introduced phase 1 which compensates the incident phase ($\phi_m^{incidence}$) induced

by the feed and another phase that introduces the desired phase law S_1 . Hence, the reflected phase for S_1 is computed using Equation 3.16.

$$\phi_m^{reflectedS_1} = \phi_m^{incidence} + \phi_m^{introduced1} + \phi_m^{introduced2} \quad (3.16)$$

With $\phi_m^{introduced1}$ and $\phi_m^{introduced2}$ the phase introduced by the cell to respectively compensate the incident phase and introduce the depointing.

$$\phi_m^{introduced1} = -\phi_m^{incidence} = \beta_0 R_m \quad (3.17)$$

R_m is the distance between the source and the center of the $Cell_m$. Moreover:

$$\phi_m^{introduced2} = m\alpha = md\beta_0 \sin(\theta) \quad (3.18)$$

With:

- α : the phase difference between two consecutive cells
- d : the spacing between two elements
- β_0 : the wavenumber
- θ : the depointing angle

The second phase law, S_2 , is also a directive beam as S_1 but presents an enlarged beamwidth which is due to the introduction of a non-linear phase law in the yOz plane, $\phi_m^{introduced3}$. The reflected phase for the second configuration, $\phi_m^{reflectedS_2}$, could be computed such as in Equation 3.19.

$$\phi_m^{reflectedS_2} = \phi_m^{reflectedS_1} + \phi_m^{introduced3} \quad (3.19)$$

Figure 3.6 illustrates the phase law introduced along the y -axis to enlarge the beamwidth, of roughly 25° instead of 8° for 3 dB beamwidth for S_1 .

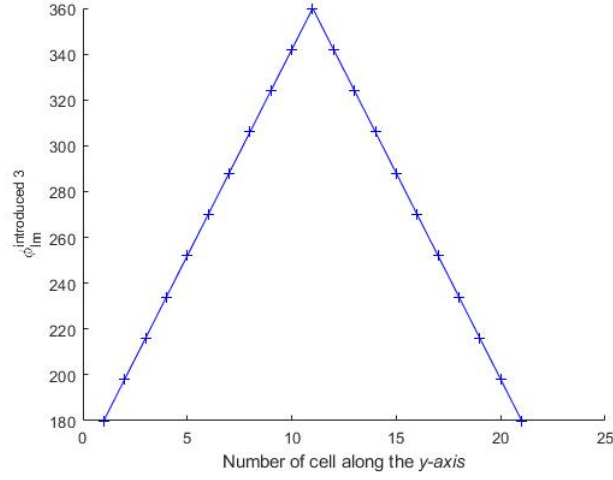


FIGURE 3.6: Introduced phase law for S_2 .

The phases that need to be introduced by the cell are written $\phi_m^{S_i}$ and can be computed using Equation 3.20 for S_1 and 3.21 for S_2 .

$$\phi_m^{S_1} = \phi_m^{\text{introduced1}} + \phi_m^{\text{introduced2}} \quad (3.20)$$

$$\phi_m^{S_2} = \phi_m^{S_1} + \phi_m^{\text{introduced3}} \quad (3.21)$$

Figure 3.7 shows $\phi_m^{S_1}$ and $\phi_m^{S_2}$ that the cells need to produce to respectively provide the desired directivity patterns for S_1 and S_2 .

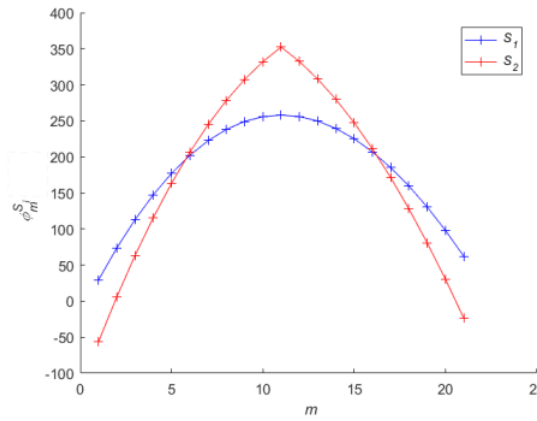


FIGURE 3.7: Phases that need to be produced by the cells at $x=0$.

3.3.2.4 Computation of the average admittance along the panel

Following the initialization of the layout process explained before, the admittances related to S_1 and S_2 along the 1D panel respectively $b_m^{S_1}$ and $b_m^{S_2}$ are computed considering $h_m^{S_1} = h_m^{S_2} = \frac{\lambda_0}{4}$ as the average admittance, b_m^{ave} is calculated to make the first selection of cells. Then, Figure 3.8 presents the admittance values computed for each $Cell_m$ over the panel.

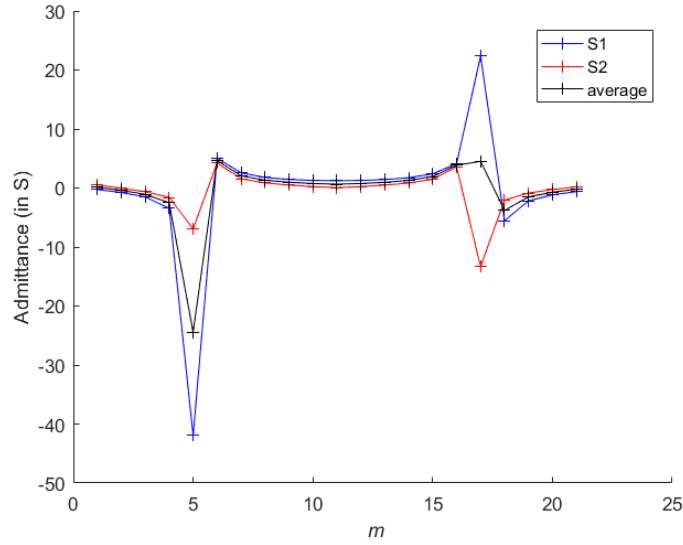


FIGURE 3.8: Admittances $b_m^{S_1}$, $b_m^{S_2}$, and b_m^{ave} for the 1D panel considering $h = \frac{\lambda_0}{4}$.

In Figure 3.8, significant variations can be noticed for the cell n°5 and 17. These big variations of the admittances are linked with the intersection of the phase laws required for S_1 and S_2 and happen around the cells n°5, 6, 16 and 17 (cf. Figures 3.7 and 3.8). This phenomenon can be explained by the fact that their phase is close to 180° .

Indeed, as mentioned in Chapter 2 while analyzing the impact of the distance h on the phase response of a cell, most of the cells produce a reflected phase near $+180^\circ$ when $h_m^{S_i}$ is around 0 mm. They produce a phase close to -180° while $h_m^{S_i}$ is near $\frac{\lambda_0}{2}$. By applying a modulo on the phase introduced by the cell to have values between $+$ and -180° , the $Cell_m$ with $m \in [0, 4] \cup [17, 21]$ have to introduce a phase between 0 and 180° for both coverages. Therefore, the big variations of the average admittance are due to the phase jump around $+/-180^\circ$.

3.3.2.5 Computation of the average phase

The average phase is deduced from $b_m^{average}$ using Equation 3.6 and noted $\phi_m^{average}$. The values of the average phase are then clipped to be included in the range of $\pm 150^\circ$.

Note that clipping the average consists in considering that all values not included in the range $\pm 150^\circ$ is redefined to be equal to the closest value between $\pm 150^\circ$. Figure 3.9

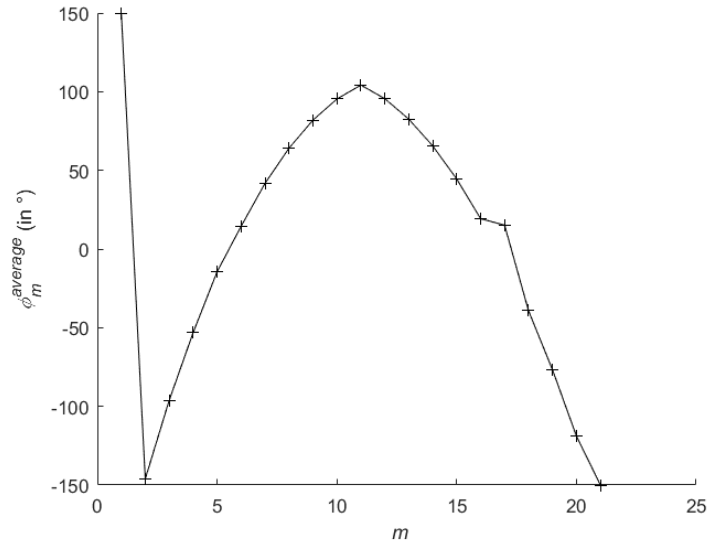


FIGURE 3.9: Average phase along the panel.

In Figure 3.9, the clip of the average phase could be noticed as the extremum are equal to $\pm 150^\circ$.

3.3.2.6 First selection of cells

Once the average phase is clipped, the first layout of the linear panel is deduced. This selection takes as the database, the clipped average phase, and a flat ground plane placed at $h_m^{S_i}$ equal to $\frac{\lambda_0}{4}$ as inputs. Figure 3.10 illustrates this first layout.

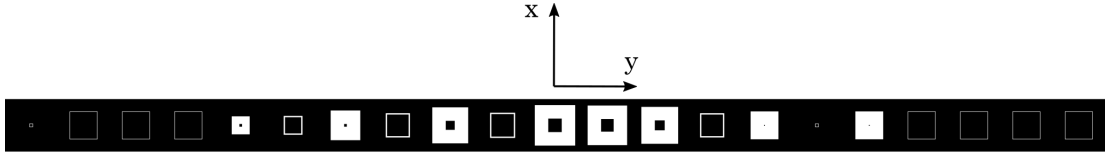


FIGURE 3.10: First cells selection for the linear array.

Using the information of the database and the first layout illustrated in Figure 3.10, the actual phase produced by the cells considering a flat ground plane placed at $\frac{\lambda_0}{4}$ is presented in Figure 3.11. The ideal average phases are the ones targeted while the produced ones are the ones deduced considering the first cells selection.

Figure 3.11 shows a good correlation between the produced average phase and the ideal one with the first layout identified. The remaining differences between the ideal average phases targeted and the phase response finally obtained are due to a limitation induced by the database.

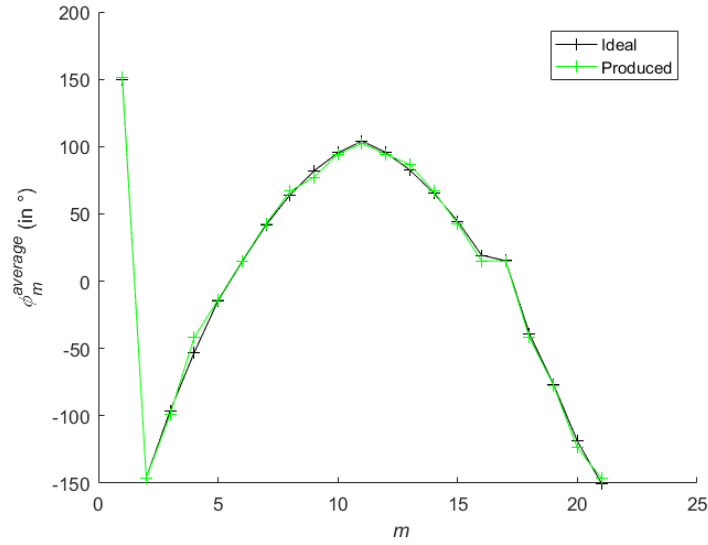


FIGURE 3.11: Ideal and produced average phase along the panel.

3.3.2.7 Identification of the ideal deformation

Starting from the layout obtained previously, associated to a flat ground plane at $\frac{\lambda_{da0}}{4}$, the ground plane is deformed to modify the phase response of each cell in order to provide the first configuration S_1 . Then, in a second time, it will be deformed in a second way to provide the second configuration S_2 .

The set of ideal deformations are deduced using Equation 3.6 and the ideal phase $\phi_m^{S_i}$ that the cell has to produce (cf. Figure 3.6). It is done using the set of phase laws, the database, and the cells selection made and presented in Figure 3.10.

Figure 3.12 presents the ideal set of deformations deduced. These deformations are smooth over the panel except around several cells where a big variation between two consecutive cells could be observed (n°2, 5, 17). As regards of Figure 3.8, those variations are close to the cells n° 5 and 17 and could be explained by the relation between the admittance and the phase response of the cell (see Equation 3.6).

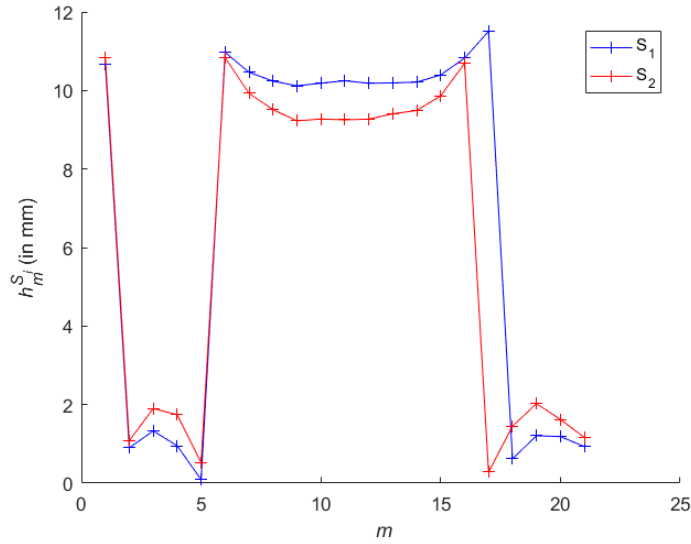


FIGURE 3.12: Ideal deformations associated with S_1 and S_2 .

These big variations of distance $h_m^{S_i}$ between two consecutive cells must be avoided notably due to the existing material's properties [41] and the hypothesis of local planarity of the ground plane under the cell. Indeed, these sharp variations of the $h_m^{S_i}$ imply quasi-perpendicular deformations.

To avoid this variation of $h_m^{S_i}$, an additional distance shift equal to $\frac{\lambda_0}{2}$ is could be added to the initial value of $h_m^{S_i}$ while it is useful to smooth the deformation. Figure 3.13 presents the ideal deformation with this additional distance shift. Note that this distance shift is only used while it is necessary to reduce the variation of $h_m^{S_i}$ between two consecutive cells.

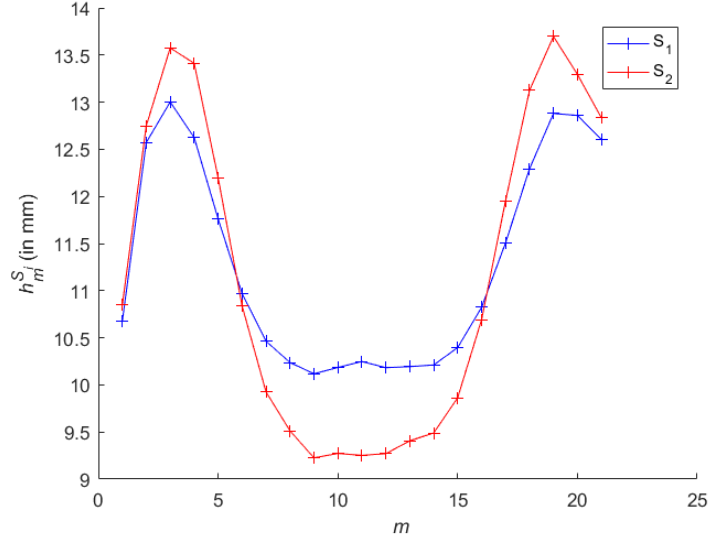


FIGURE 3.13: Ideal deformations associated with S_1 and S_2 .

By comparison between the Figures 3.13 and 3.12, the interest of the additional distance shift is clearly underlined. The membrane slope between consecutive cells is reduced as expected, as well as the maximum magnitude of deformations. For example, the ideal deformation associated with S_1 in Figure 3.12 has a magnitude around 12 mm whereas in Figure 3.13 it is around 5 mm.

3.3.2.8 Results: directivity patterns

Considering the first layout and the ideal deformations associated with S_1 and S_2 , the directivity patterns are computed thanks to the array factor for the cut-plane ($\Phi=90^\circ$). Figures 3.14 presents the directivity patterns wanted (ideal) and the provided ones (with the set of phase laws produced while considering the cells selection and the set of ideal deformations) for the linear array.

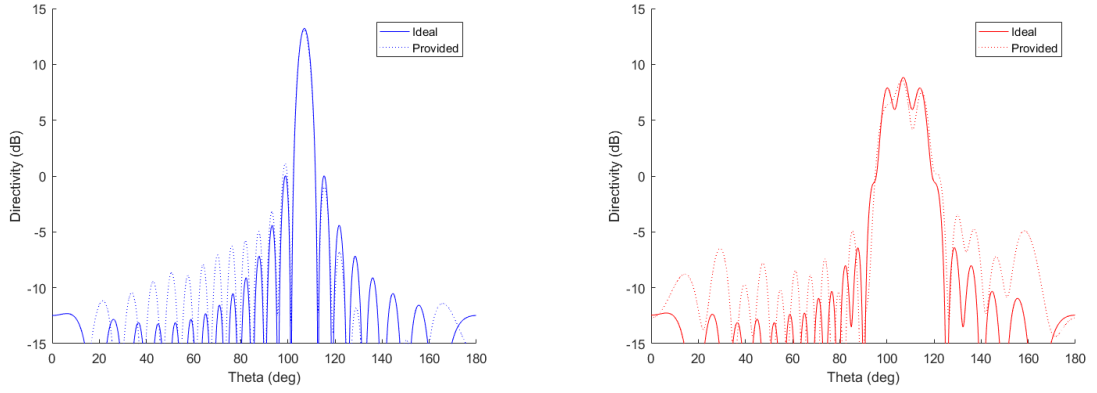


FIGURE 3.14: Ideal phase distribution over the panel for S_1 (left) and for S_2 (right).

In Figures 3.14, some differences could be noticed between the ideal and the computed curves. Those are due to the cells database which doesn't include every possible set of couples $(h_m^{S_i}; \phi_m^{reflected S_i})$ for S_1 and S_2 . Indeed, the cells are selected while they present the closest reflected phase to the clipped average phase at $h_m^{S_i} = \frac{\lambda_0}{4}$, which induces some phase errors.

3.4 Proposal for improvements

Chapter 1 introduce the multi-objective optimization issue, mentioned in the literature [125]. The studies figure out that enhancing the RF coverages while maintaining the magnitude of deformation at a low-level constitutes conflicting objectives.

The resulting coverages depend on the ground plane (also called membrane) shape accuracy which is induced by the mechanical control accuracy made using actuators. The quality of the obtained directivity pattern relies on this control, and also on the behavior of the cells selected while encountering an error of the distance $h_m^{S_i}$.

This section aims to develop a methodology that considers realistic constraints for the prediction and the control of the ground plane shape to optimize the *RRA* RF performance. Indeed, as it has been discussed before, the quality of the *RF* performance is directly dependent on the deformation accuracy as it controls the reflection phase of each radiating element composing the panel.

This section introduces several solutions to limit the magnitude of the deformations and to minimize the number of actuators (to limit the mass of the antenna). These improvements are tested using the same sample case as the previous section.

3.4.1 Mechanical control and prediction of the ground plane-shape

In the sample case studied in the last section, the control of the ground plane is supposed perfect which is impossible in reality due to technical constraints. The closest configuration would theoretically be the one that considers one cell per actuator. Unfortunately, the space needed between two consecutive actuators and the limited weight of the antenna discard this possibility. Moreover, the number of actuators also impacts the cost of the antenna.

The existing mechanically *RRA* used various types of actuators, such as piezoelectric or linear actuators. In our case, linear actuators are best suitable because of their high stroke capability and high accuracy. Moreover, the mechanically reconfigurable reflector studied in [39] on which our concept is based also used linear actuators. Hence, it will be useful to benchmark the concept of *RRA* presented in this work with existing reconfigurable antennas in terms of the number of actuators and the magnitude of deformation. In [39], the prototype tested is a 500 mm diameter reflector equipped with 19 actuators.

Furthermore, in [39], the prediction of the reflector shape has been made using simulations, and a model has been developed taking into account the action of the actuators, the characteristics of the material, and the boundary conditions to consider to let the membrane free of constraints. The same requirements need to be considered in our case.

3.4.1.1 Distribution of the actuators for the control of the ground plane shape

In the context where the *RRA* aims to be low-profile, flexible, light-weight, and accurate, a limited number of actuators must be defined. Their distribution is also a constraint to take into account while optimizing the control and the prediction of the ground plane shape.

Two types of distributions are distinguished: the uniform and the adjusted one presented in Figure 3.15. Note that both have to follow the same constraint, which consists of having one actuator at each border and at least one between in the case of a linear array panel.

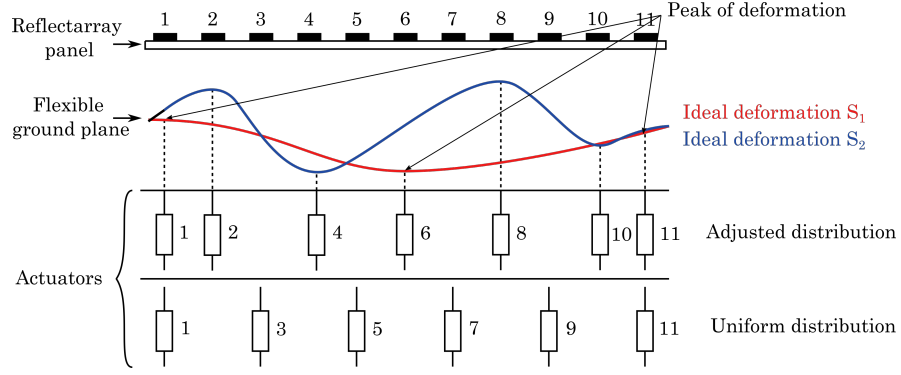


FIGURE 3.15: Homogeneous and adjusted actuators' distribution.

As Figure 3.15 illustrates, the adjusted distribution consists of placing the actuators at every peak considering the set of ideal deformations. Nevertheless, it is directly dependent on the set of radiation patterns as it is defined by the targeted phase laws.

The uniform distribution allows standardization of the solution as the actuators are regularly distributed under the panel as it is reminded in [39] and it is preferred. This distribution is consequently preferred as the adjusted one.

As the uniform actuators' distribution is preferred and considering that three actuators are already placed, only a few possibilities exist. Once the first design is defined for the ideal case, the next steps aim to introduce error in the ground plane deformation by implementing points of control which will be associated with the location of the actuators. At a first instance, one actuator is considered for one cell under which it is located. The number of actuators is reduced from M to 3 step by step while still considering a regular distribution.

3.4.1.2 Approximation and prediction of the ground plane shape for a linear array

3.4.1.2.1 Setup of the ground plane deformation model

As a first approximation, the deformation of the ground plane between two consecutive actuators is considered linear. We consider that the approximated values of the displacements provided by the actuators are considered as the displacements to apply in the mechanical model for the prediction of the ground plane shape without considering a actuator/membrane interface. This model is developed using the Ansys Mechanical software and a 3-layers CFRS (*carbon fiber-reinforced silicone*) [39] as it has been advised by the experts from *LSS*. This model is then called Ansys Mechanical model. The material characteristics of the flexible membrane, or ground plane, are given in Table 3.1.

Density	1.378g.cm ⁻³
Young modulus - x-axis	3200 MPa
Young modulus - y-axis	3200 MPa
Young modulus - z-axis	3200 MPa
Poisson coefficient - XY	0.8
Poisson coefficient - YZ	0.2
Poisson coefficient - XZ	0.2
Shear modulus - XY	8.85 MPa
Shear modulus - YZ	10 MPa
Shear modulus - XZ	10 MPa

TABLE 3.1: Material characteristics of the flexible ground plane used for the Ansys Mechanical model.

Two test cases are presented in this section with a various number of actuators to illustrate the first approximation and the setup of the ground plane deformation model. The number of the cell as the actuators index over the panel, as shown in Figure 3.16.

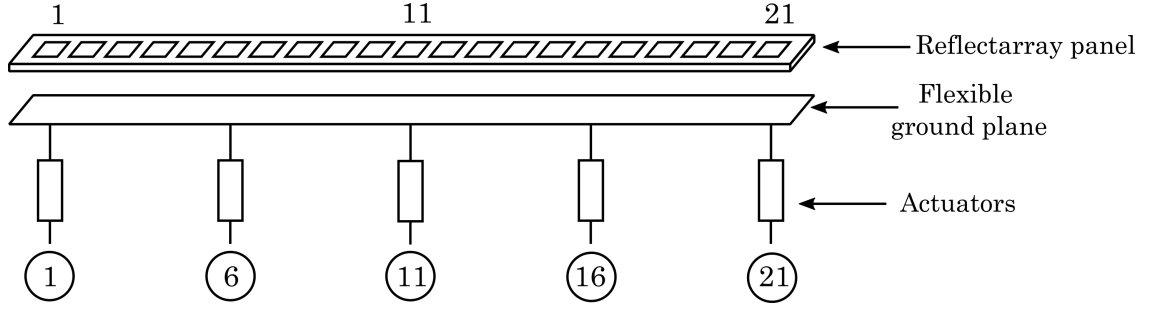


FIGURE 3.16: Application of the actuators' action on the ground plane considering the *RRA* panel.

The actuators' distributions tested are :

- case 1, 5 actuators: (1, 6, 11, 16, 21)
- case 2, 3 actuators: (1, 11, 21)

Figure 3.17 shows the approximation of the ideal deformations for Case 1 and Case 2. S_1 and S_2 correspond to the ideal deformations and $S_1 - linear$ and $S_2 - linear$ are the linear approximations associated with.

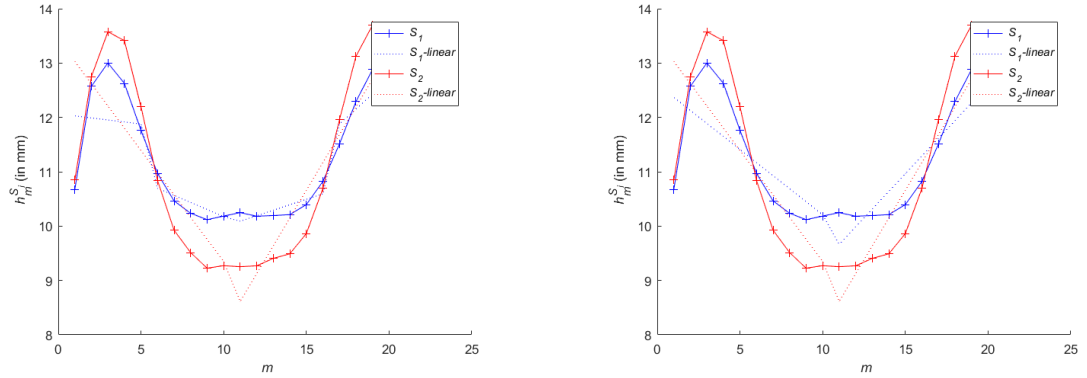


FIGURE 3.17: Ideal and linear approximation of the deformations for S_1 and S_2 for the case 1 (left) and the case 2 (right).

The average distance error for each m location over the panel, noted $\bar{\epsilon}_m^{S_i}$, can be deduced from Equation 3.22 and Figure 3.17.

$$\bar{\epsilon}_m^{S_i} = \sum_{i=1}^M \frac{|h_m^{S_i} - h_m^{S_i-linear}|}{M} \quad (3.22)$$

The average distance errors along the panel given for Case 1 and Case 2 are shown in Table 3.2.

	S_1	S_2
Case 1	0.33 mm	0.63 mm
Case 2	0.48 mm	0.55 mm

TABLE 3.2: Average error distance along the panel.

Using the database and the linear approximation of the ideal deformations, it is possible to compute the directivity pattern obtained with these linear deformations thanks to array factor computation. Figures 3.18 and 3.19 illustrate these directivity patterns.

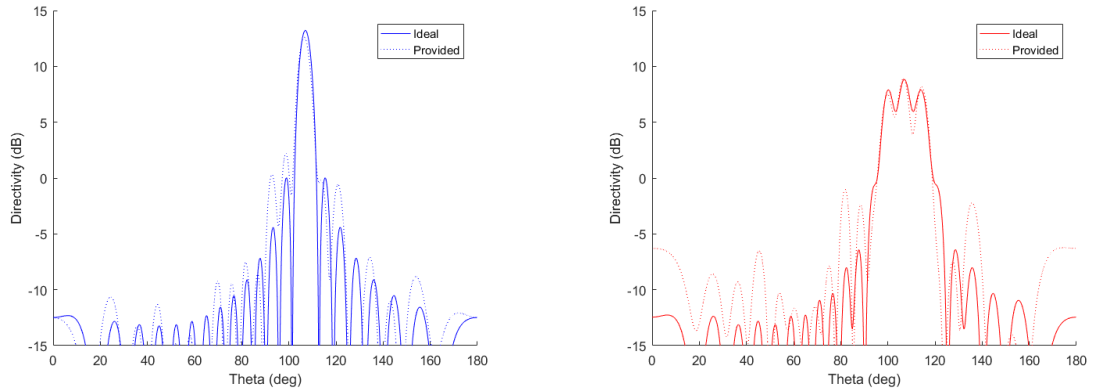


FIGURE 3.18: Directivity patterns for the linear array for the case with 5 actuators uniformly distributed for S_1 (left) and for S_2 (right).

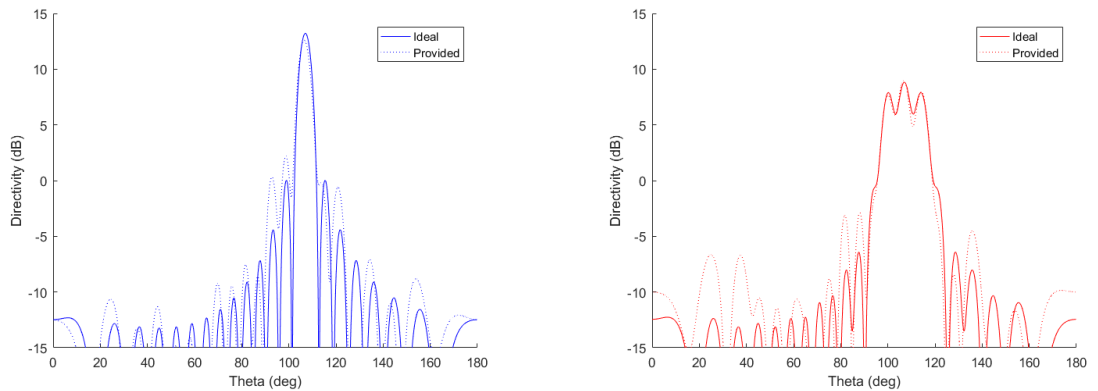


FIGURE 3.19: Directivity patterns for the linear array for the case with 3 actuators uniformly distributed for S_1 (left) and for S_2 (right).

In Figures 3.18 and 3.19, some differences between the ideal and the directivity patterns obtained with the linear deformations can be noticed. These differences can be explained by the difference between the ideal distance $h_m^{S_i}$ and the linear one.

Figures 3.18 and 3.19 show the difficulty to predict the optimized number and distribution of actuators without having information concerning the ideal deformation. Indeed, intuitively the phase error decreases while increasing the number of actuators. However, it is not always true because of the non-linearity of the phase versus the distance between the cell and the ground plane, as it could be noted in Figures 3.18 and 3.19.

Case 2 is preferred as the number of actuators is reduced at the maximum while ensuring acceptable directivity patterns compared to Case 1.

3.4.1.2.2 Boundary conditions for the ground plane deformation model

As the case of three actuators has been chosen, the displacements are applied in the center of the cells 1, 11 and 21, as shown in Figure 3.20. The value are the ones deduced from the linear approximations of the ideal deformations. Tab. 3.3 gathers the value of $h_m^{S_i-linear}$ considered for S_1 and S_2 . Hence, the displacements applied to the actuators are now equal to $h_m^{S_i-linear}$ taking the bottom of the substrate as a reference.

	Actuator 1	Actuator 11	Actuator 21
S_1	12.40 mm	9.08 mm	12.83 mm
S_2	13.07 mm	8.80 mm	13.71 mm

TABLE 3.3: Displacements applied to the actuators taking the bottom of the substrate as a reference.

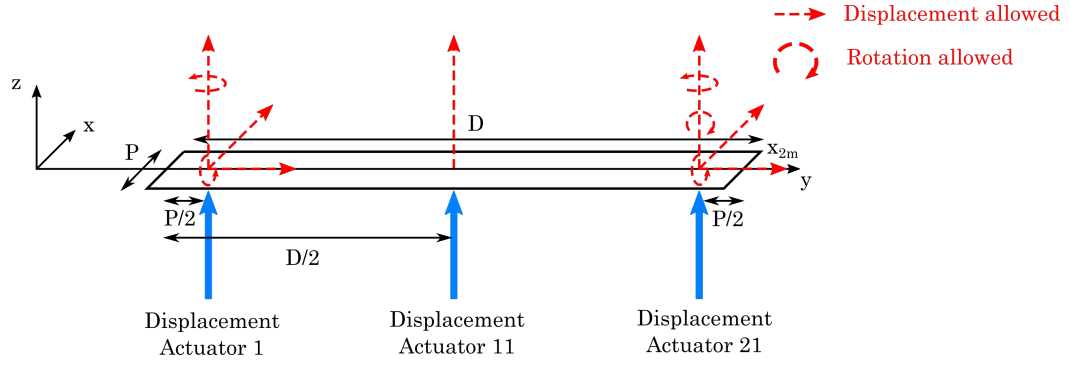


FIGURE 3.20: Setup of the mechanical model.

Figures 3.21 and 3.22 give the simulation results for S_1 and S_2 . The dimension of the linear panel is $M \times P$ with a thickness equal to 0.5 mm.

Note that the displacements are computed considering that the reference displacement applied is equal to the actuator 11 one for each coverage (cf. Table 3.3). Therefore, the set of displacements values respectively for S_1 and S_2 for Actuator 1 is (3.32, 4.9) mm and for Actuator 21 is (3.75, 4.91) mm.

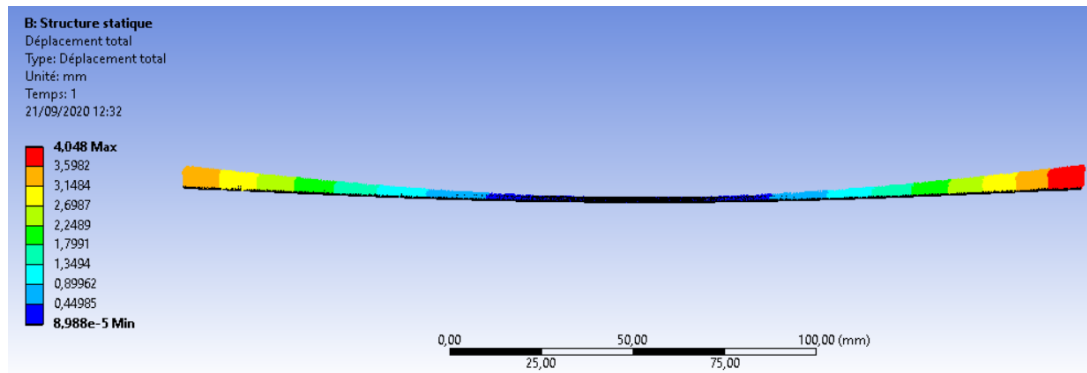


FIGURE 3.21: Result of the mechanical model for S_1 .

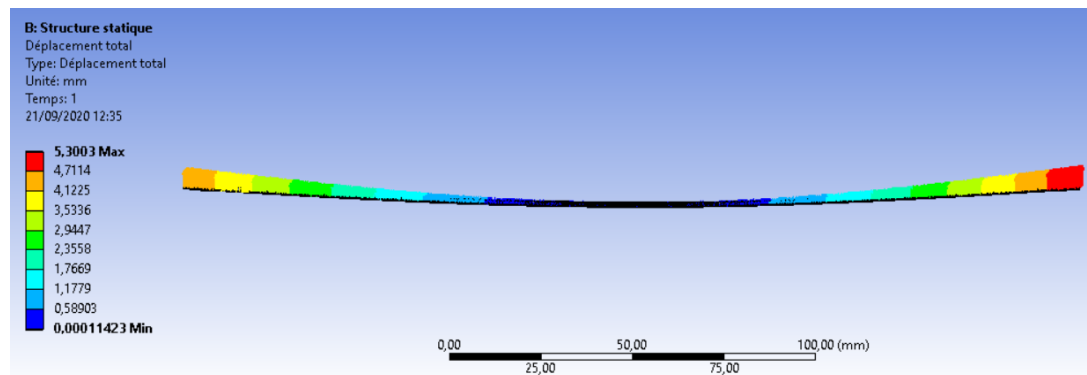


FIGURE 3.22: Result of the mechanical model for S_2 .

For each configuration, the simulation gives the predicted ground plane shape while applying the actuators displacement. Therefore, the profile of the ground plane shape is extracted and scattered in 21 parts associated with the M cells composing the panel.

The central node of each part is considered aligned with the center of one reflecting elements. Hence, a set of two profiles is obtained.

Note that the predicted deformation, noted $S_i - Ansys$ on Figure 3.23, is the sum of this deformation extracted, scattered, and normalized with the reference displacement value (in our case, the displacement value of the central actuator). Figure 3.23 presents the ideal deformations, the linear and the predicted ones.

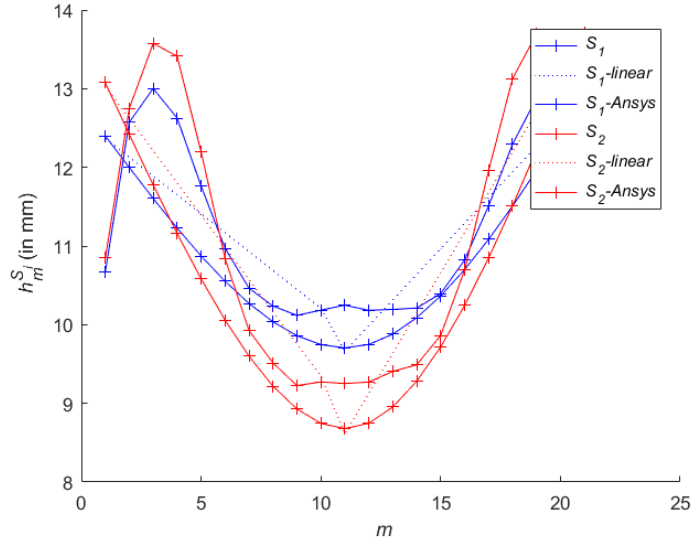


FIGURE 3.23: Ideal, linear and predicted deformations for S_1 and S_2 .

3.4.1.3 Results

The directivity patterns provided considering the deformations predicted with the Ansys Mechanical model are presented in Figure 3.24

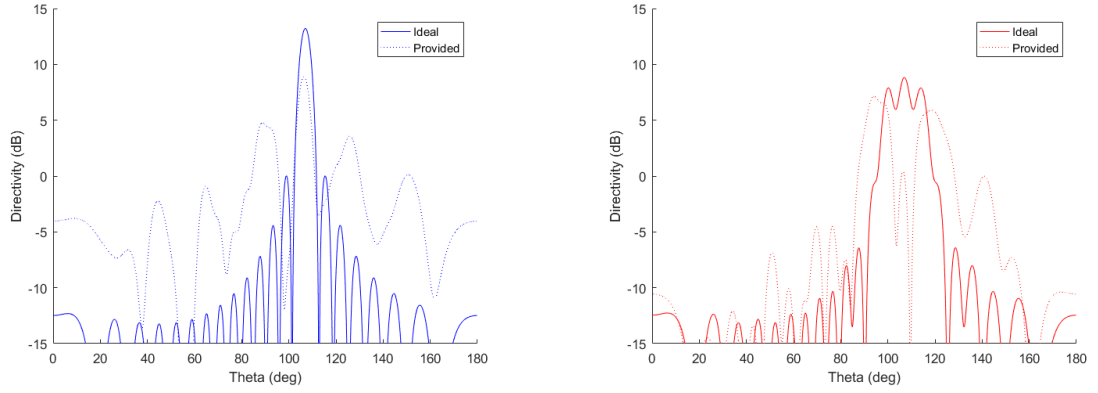


FIGURE 3.24: Directivity patterns for S_1 (left) and for S_2 (right).

The directivity patterns provided and computed for the linear array using the array factor computation show significant differences with the ideal ones which is unacceptable. In order to improve these result another step is proposed which consists in a second selection of cells.

3.4.1.4 Solution proposal to improve the layout

To improve the performances of the design considering an established *RRA* configuration in terms of number and distribution of actuators, a second selection of cells is proposed. This second selection takes as input the ideal phase that the cells have to produce and the set of predicted distances $h_m^{predictedS_i}$ extracted from the Ansys Mechanical simulation. Using this information, its goal is to select the cells composing the database that minimizes the phase error for both coverages.

For each $Cell_m$, a set of two predicted distances $h_m^{predictedS_i}$ is considered and extracted from the previous Ansys Mechanical simulation ($h_m^{predictedS_1}, h_m^{predictedS_2}$). Each cell of the database provided for these set of predicted deformations a couple of phases $(\phi_k^{predictedS_1}, \phi_k^{predictedS_2})$ with k the number of cells composing the database.

Therefore, for each value of $m \in [1, 21]$, k sets of phase can be provided thanks to the cells included in the database. By comparison with a couple of ideal phases that $Cell_m$ must produce noted $(\phi_m^{S_1}, \phi_m^{S_2})$, the cell presenting the lowest average phase error is selected for the second distribution. This average phase error, noted $\bar{\phi}_k^m$, is computed thanks to Equation 3.23.

$$\bar{\phi}_k^m = \frac{|\phi_m^{S_1} - \phi_k^{predictedS_1}| + |\phi_m^{S_2} - \phi_k^{predictedS_2}|}{2} \quad (3.23)$$

The second layout of the 1D panel is illustrated in Figure 3.25.

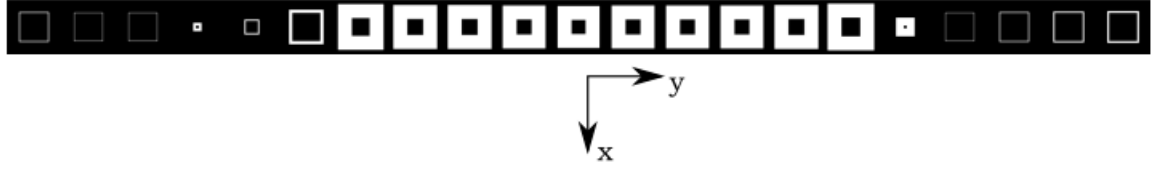


FIGURE 3.25: First cells distribution for the 1D panel after a second cell selection.

The directivity patterns computed using this second selection are illustrated in Figure 3.26.

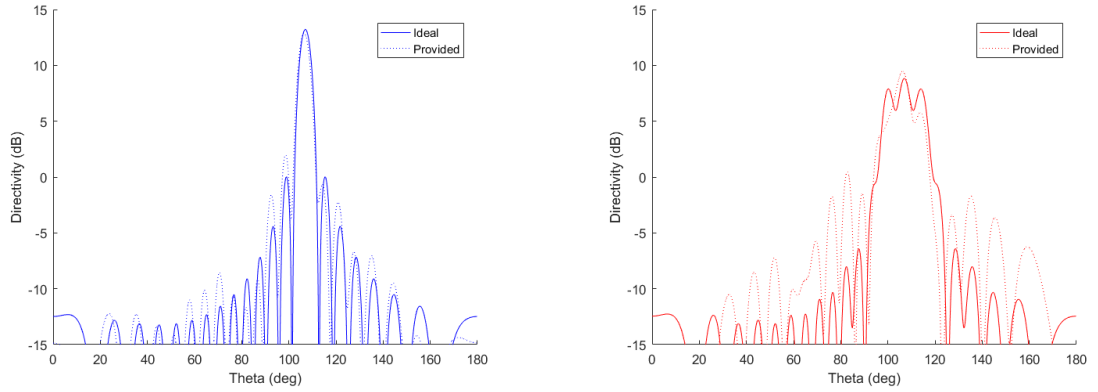


FIGURE 3.26: Directivity patterns for S_1 (left) and for S_2 (right) with the second layout.

As expected, the comparison between the Figures 3.24 and 3.26 shows the interest of the second selection of the cells. Indeed, the directivity patterns provided with this new layout are overall good. As a reminder, Figures 3.24 present the directivity patterns obtained with the first selection of cells which are unacceptable, while Figures 3.26 show the results with the second layout.

3.4.2 Iteration on the possible set of deformations

The solution proposed in the application case presented deformations for which $h_m^{S_i}$ is between 8.80 mm and 13.7 mm (approximately $0.38\lambda_0$ and $0.57\lambda_0$). To find

a better set of deformations, one solution is to modify the phase laws targeted without changing the directivity patterns. This could be done using phase offsets.

As it could be noticed in Figures 2.15 using the behavior of the cells detailed in the previous chapter, in the intervals $[0;0.15\lambda_0]$ and $[0.44\lambda_0;0.5\lambda_0]$ most of the cells have a reflected phase in the range of $[180^\circ;140^\circ]$ or $[-140^\circ;-180^\circ]$. Hence, adding a phase offset to each phase law targeted allows modifying them to have most of the phases to provide by the cells in the interval $[-140^\circ;+140^\circ]$. Hence, the principal idea is to center the phase laws around 0° .

Figure 3.27 illustrates the phase laws targeted with the consideration of phase offsets.

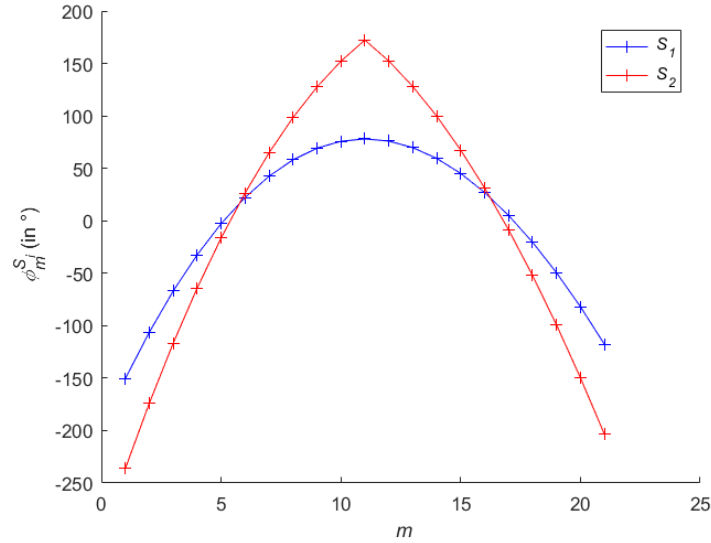


FIGURE 3.27: Ideal phase laws with phase offsets.

The new ideal phase laws are then used as input to derive the ideal deformations and then the predicted ones. The prediction of the ground plane shape is carried out with the same model on Ansys Mechanical while taking the new values of actuators displacements. These values are derived from the linear approximation of the ideal deformations in the case of three actuators distributed uniformly over the panel.

Figure 3.28 presents the set of ideal deformations, the linear, and predicted ones.

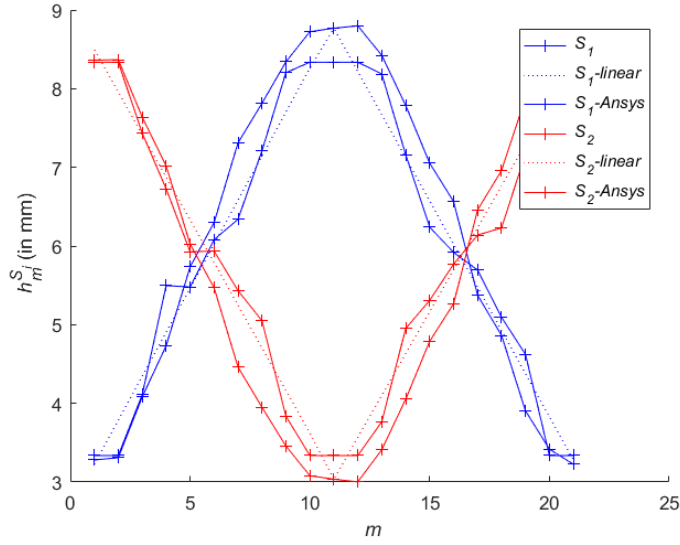


FIGURE 3.28: Ideal, linear and predicted deformations for both coverages.

Due to the new set of ideal phase laws, most of the phases that the cells have to produce are between $\pm 140^\circ$. Therefore, it could be deduced that the deformations are centered around $\frac{\lambda_0}{4}$. Consequently, it is not necessary to add a distance shift to reduce the membrane slope between two consecutive cells.

The design of the linear array is then derived following the same procedure as the previous one. Therefore, the cells selected provide the closest phase considering both coverages simultaneously. The displacements applied to the actuators are now equal to $h_m^{S_i-linear}$ taking the bottom of the substrate as a reference are gathered in the Table 3.4 .

<i>Number of the actuator: m</i>	1	11	21
Displacement for S_1	3.23 mm	8.77 mm	3.28 mm
Displacement for S_2	8.50 mm	3.04 mm	8.36 mm

TABLE 3.4: Displacements applied to the actuators for each configuration for the 2D panel.

After the second selection of cells, the 1D panel obtained is presented Figure 3.29.

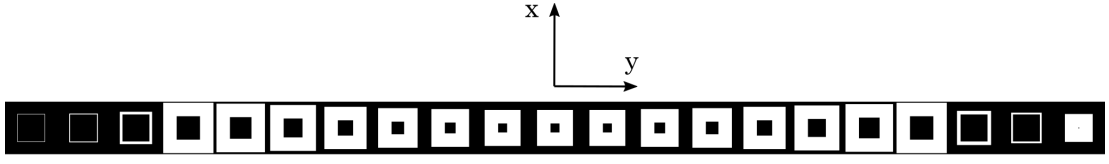


FIGURE 3.29: Selection of cells for the new layout.

Figure 3.30 illustrates the ideal and predicted radiation patterns considering this second layout and the set of predicted phase laws.

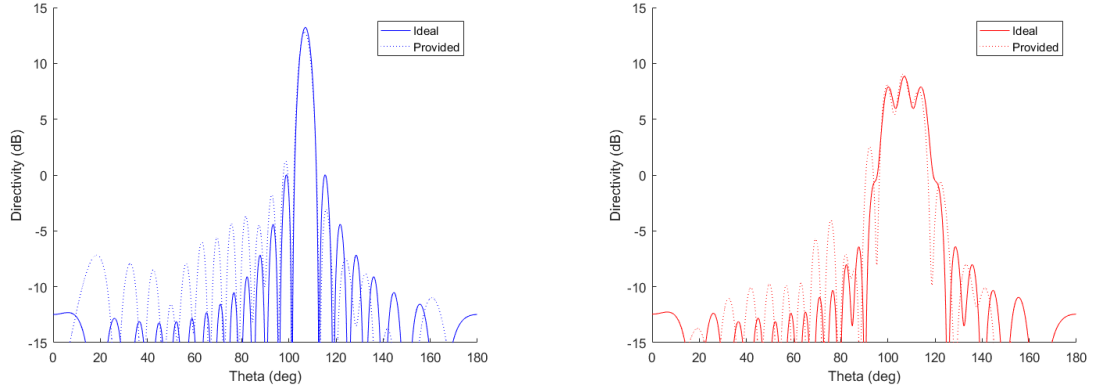


FIGURE 3.30: Ideal and predicted directivity pattern for S_1 (*left*) and for S_2 (*right*).

Figure 3.26 shows that the results obtained with the new layout are as good as the ones presented with the first one. The first layout and the second ones are tested in frequency to verify if both are acceptable. The frequency range tested is [12.35 GHz; 13.35 GHz].

At 12.35 GHz

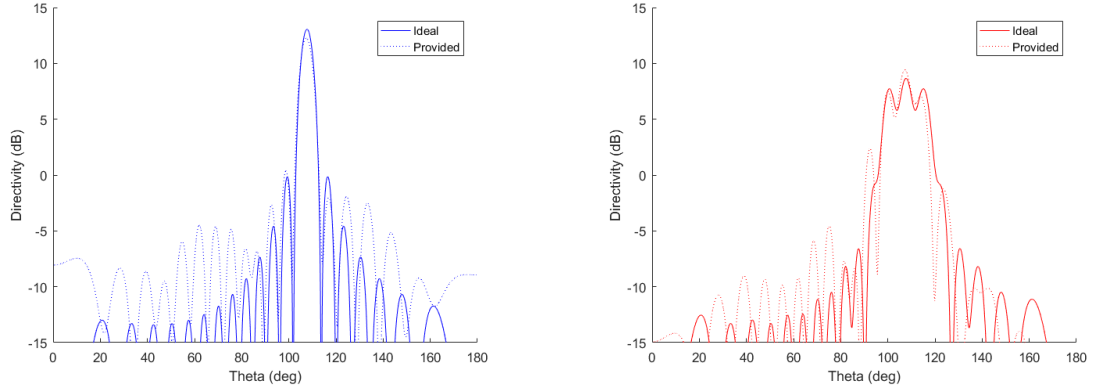


FIGURE 3.31: Ideal and predicted directivity pattern for S_1 (*left*) and for S_2 (*right*) at 12.35 GHz.

At 13.35 GHz

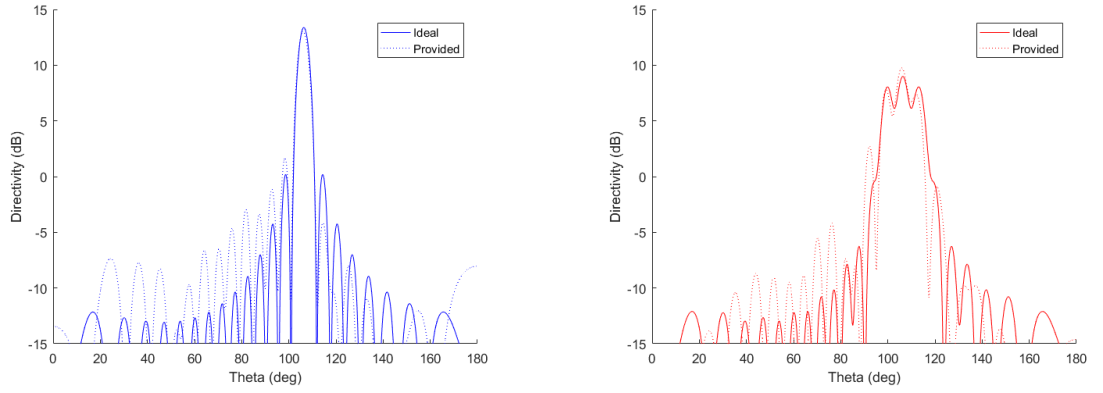


FIGURE 3.32: 2D Directivity patterns for S_1 , test case (*left*) and for S_2 (*right*) at 13.35 GHz.

The second layout is preferred compared to the first one because it is not necessary to add a distance shift to smooth the deformation, and also because the frequency dispersion is acceptable. Moreover, the magnitude of predicted deformations is less important than for the first layout. Furthermore, it avoids the use of the additional distance whose impact is not known.

3.4.3 Final methodology proposal for a linear *RRA*

Figure 3.33 presents the final methodology proposal, which takes into consideration all the way of improvements presented in the last sections.

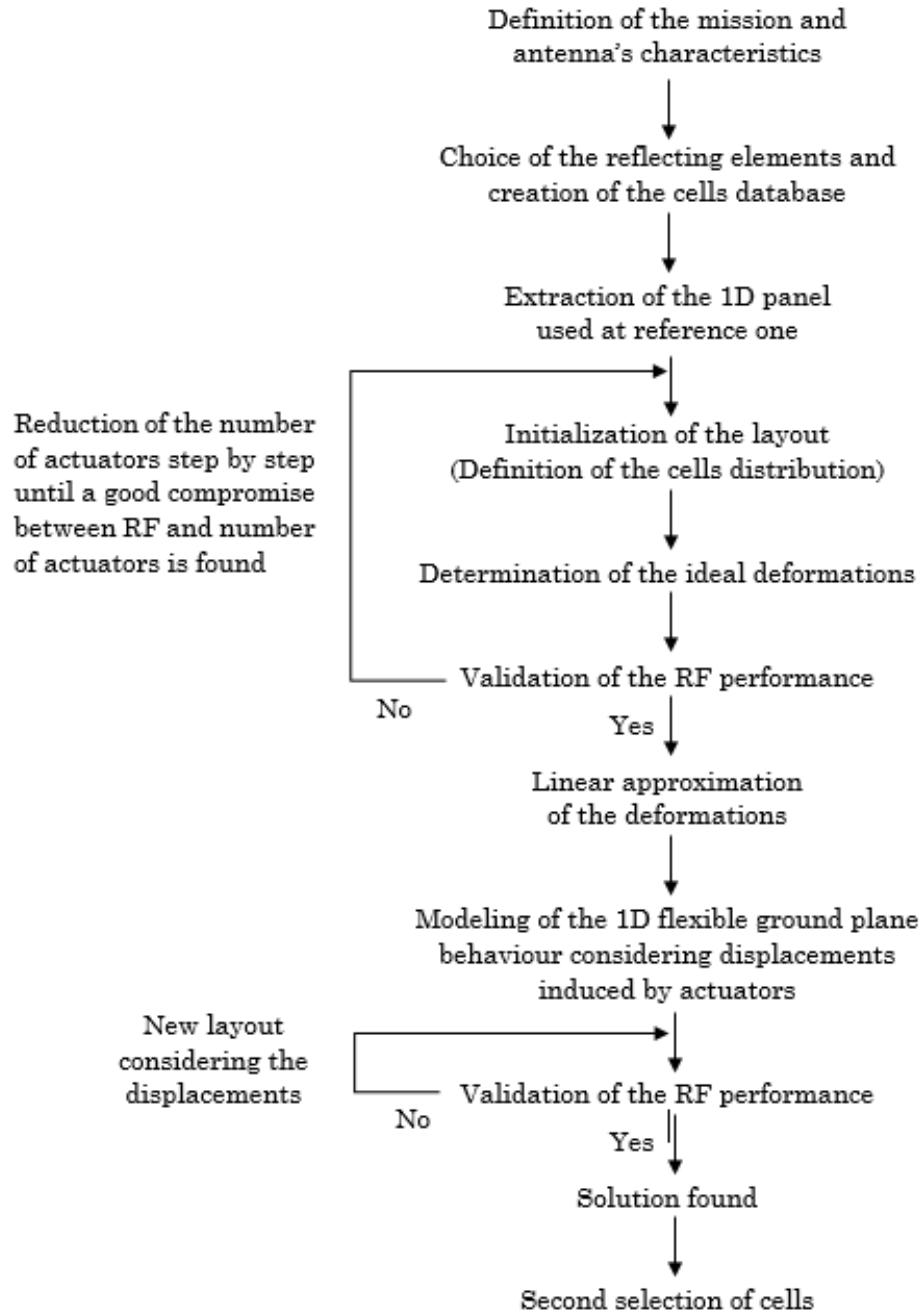


FIGURE 3.33: Flowchart of the final design methodology for a linear array with a two-configuration capabilities.

The design methodology is easy to follow while simplifying it by considering only a few parameters such as the number and distribution of actuators. Nevertheless, some improvements can still be done notably for the frequency dispersion for which the layout is not optimized.

3.4.4 Validation of the methodology by comparison with full-wave simulations

A full-wave simulation is used to validate the design deduced from the methodology developed for the linear array sample. This simulation considered the last layout presented and the ground plane after deformation extracted from the Ansys Mechanical model. Therefore, the full-wave simulation considers the most realistic membrane's shape without approximation.

Figure 3.34 presents the setup of the HFSS simulations. The structure made of the array panel and the ground plane is supposed to be excited by an x -polarized plane wave under normal incidence.

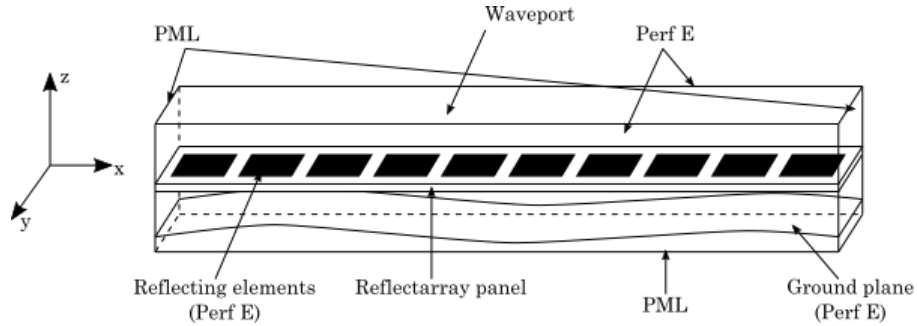


FIGURE 3.34: Setup configuration of the HFSS simulation

The full-wave simulation is important to evaluate the impact of the coupling effect, which exists between the cells of *RRA* panels and which could be increased by the deformation of the ground plane. This phenomenon could affect the quality of the obtained directivity patterns.

Moreover, this model will improve the performance prediction compared to the computed one with the array factor. Indeed, the methodology relies on the semi-analytical tool presented in Chapter 2. Hence, the cells' phase response assumes periodicity and parallelism between the cells and the ground plane.

The layout defined previously is designed thanks to HFSS software on a substrate of a permittivity equal to 2.2, as it has been used for the database. The 1D model extracted from the ANSYS model is used and imported in HFSS.

For each configuration, once the deformed ground plane is imported and placed at the good distance from the substrate, it is possible to obtain the directivity pattern.

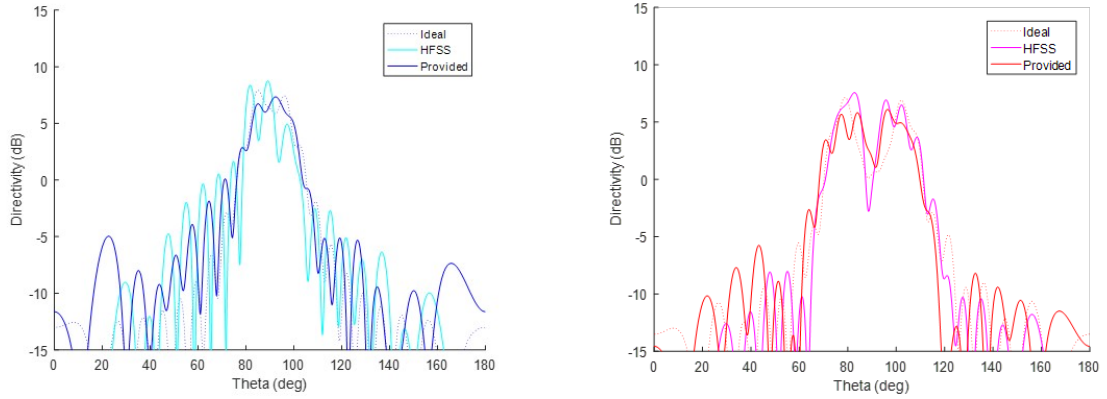


FIGURE 3.35: Comparison between ideal, computed and full-wave simulations of the 1D directivity patterns obtained for S_1 (left) and for S_2 (right).

Figure 3.35 are satisfactory considering the realistic radiation patterns that uses the Ansys predicted shape compared to the ideal and provided ones. The main lobes are overall respected and the level of the secondary lobes are the same between the provided directivity patter with the array factor computation and the HFSS Results. Hence, the design methodology is validated.

3.5 Conclusion

This chapter presents the design methodology developed for a two-configuration linear reflectarray antenna. A reconfiguration capability is added by modifying the ground plane shape made in a flexible membrane. In the case studied, the *RRA* must provide two different coverages, and therefore two deformations are applied on the ground plane. These are performed thanks to actuators distributed uniformly under the panel.

In the literature, the complexity of a mechanical reconfiguration has been investigated [39] and underlines its multiple-objective nature. These objectives, both RF

and mechanical, could be in opposition, as presented in this chapter. For example, reducing the number of actuators impacts the correlation level between the ideal and the obtained deformations, which influences the quality of the directivity patterns. To manage all of these parameters and find the best compromise, a design methodology has been proposed.

The application of the methodology is applied on a test case considering a two-configurations linear *RRA* of 21 cells extracted from a real 2D sample. The targeted directivity patterns consist of both a directive beam and an enlarged one for the same depointing angle.

The first approach to simplify the methodology is to consider one cell per actuator and only one frequency. Then, the number of actuators is reduced while verifying the acceptable performance of the design. To improve the design methodology some predictive models for the ground plane shape are developed notably using Ansys Mechanical software and used for an iteration for the cells distribution. The first design identified needs 3 actuators distributed homogeneously over the panel and leads to a maximal magnitude of deformations around 5 mm. Nevertheless, this design presents some limitations notably the necessity to add a distance shift to smooth the deformations. Hence, some proposals are tested as the set of phase offset or the second selection of cell to improve the methodology.

Finally, the methodology has been validated thanks to fullwave simulations using HFSS software. Hence, it will be the starting point for the design methodology applicable to a 2D panel. In the next chapter, the methodology is extended to a 2D sample from which the linear panel has been extracted. It is then tested using a prototype. The design, the manufacture, and the tests are also further explained.

Chapter 4

Extension of the methodology for a 2D case and breadboard testing

Contents

4.1	Introduction	95
4.2	Methodology for a 2D <i>RRA</i>	95
4.2.1	Application case definition	95
4.2.2	Application of the extended design methodology	98
4.3	Breadboard	105
4.3.1	Preliminary remarks	105
4.3.2	Objectives and inputs of the breadboard	106
4.3.3	Identification of the new ground plane shapes	107
4.3.4	Identification of the actuators displacement	109
4.3.5	Prediction of the ground plane shape	110
4.3.6	Predicted RF results	111
4.3.7	Outputs of the breadboard definition	113
4.4	Design and fabrication of the breadboard	113
4.4.1	Constraints of integration	113
4.4.2	Rear-structure	113
4.4.3	Actuators and surface-to-actuator interface	115
4.4.4	Ground plane	117
4.4.5	<i>RA</i> panel and its support system	118

4.5 Control and prediction tests of the ground plane shape119

4.5.1 Photogrammetry tests definition 119

4.5.2 Photogrammetry tests results 121

4.6 RF performance 122

4.7 Conclusion 127

4.1 Introduction

Chapter 3 presents a design methodology for a linear two-configuration *RRA* with a flexible ground plane. This design procedure is applied to a linear array sample extracted from a 2D panel and validated by fullwave simulations. This fourth chapter aims to extend this methodology to a 2D *RRA* case without changing the main objectives. Indeed, the design procedure consists in finding the optimized layout associated with a set of two predicted deformations, at one frequency, which provides the two targeted configurations S_1 and S_2 . Then, it is applied to the full 2D case presented in Chapter 3.

The design methodology extension leads to a modification of the constraints to consider, especially for the control and the prediction of the ground plane shape. Hence, the mechanical model of the ground plane deformations, which is used for the second selection of cells (cf. Chapter 3) needs to be updated.

In the first section, the design methodology is identified and applied to the 2D case. It is then tested through the manufacturing and measurement of a prototype. This developed breadboard, presented in the second section, has been assembled at Large Space Structures and tested for the RF measurements at IETR.

Two series of tests are carried out. The first one is mechanical and aims to validate the prediction of the ground plane shape using Ansys Mechanical software for each configuration and its repeatability (between prediction and measurements). The second series of tests deals with the RF measurements with the objective to assess predictions provided by the semi-analytical and fullwave analysis for both coverages.

4.2 Methodology for a 2D *RRA*

4.2.1 Application case definition

The test case used to extend the design methodology, is the one presented in Chapter 3 with the objectives reminded in the next paragraphs. For the sake of simplicity, the 2D case is considered as an assembly of 21 linear arrays. As

presented in Figure 4.1, the cells are noted $Cell_{lm}$ with $l \in [1, 21]$ (along the x -axis) and $m \in [1, 21]$ (along y -axis). Each linear array is composed of cells with the same l value.

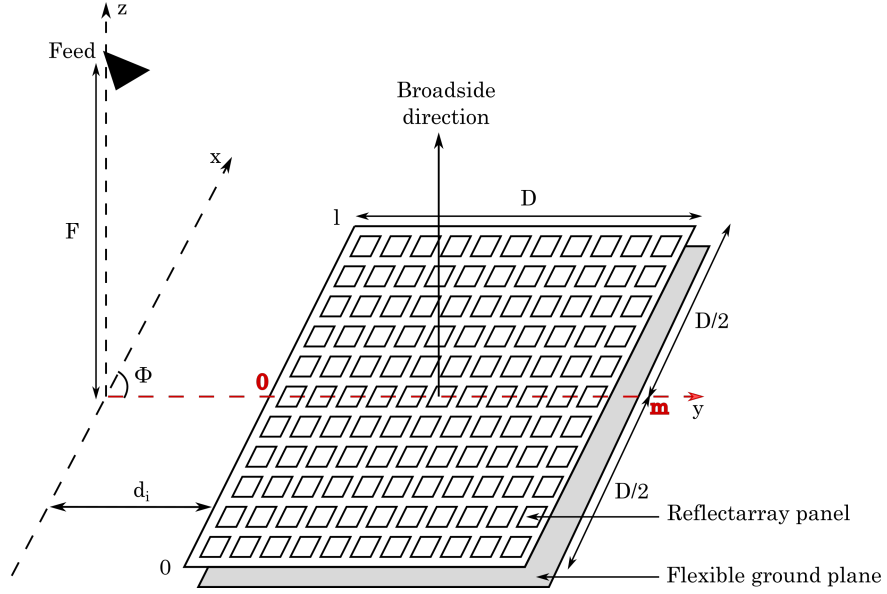


FIGURE 4.1: Antenna configuration.

RF requirements

As a reminder, S_1 is a directive beam at 17° from broadside, while S_2 is the same directive beam as S_1 with an enlarged beamwidth. Figure 4.2 presents the ideal directivity patterns associated with these two configurations for the whole panel composed of 21×21 cells.

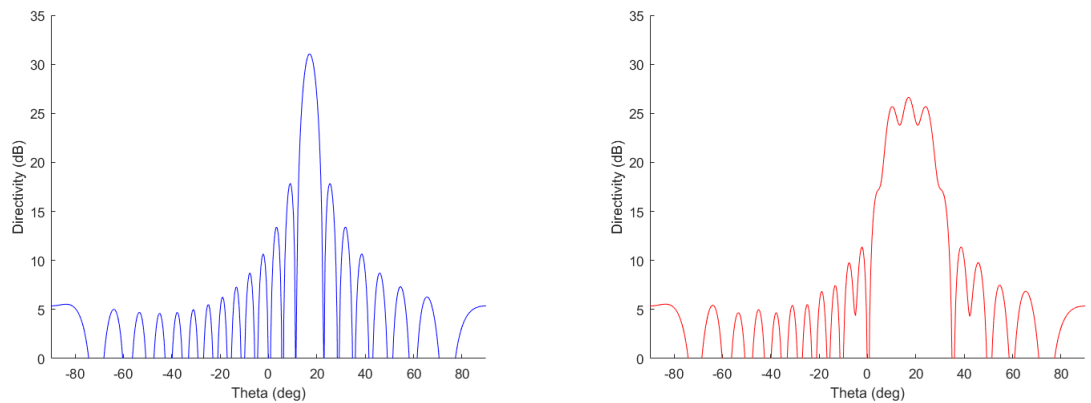


FIGURE 4.2: Ideal directivity patterns, Cut-plane $\Phi = 90^\circ$ for S_1 (left) and for S_2 (right).

Figure 4.3 presents the ideal phase distribution that the cells need to provide ($\phi_{lm}^{S_i}$).

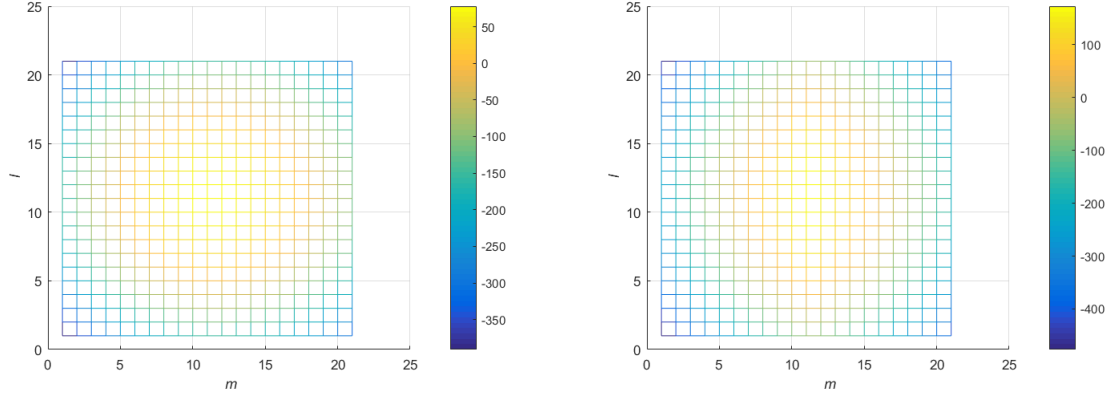


FIGURE 4.3: Distribution of the ideal cells phase response for S_1 (left) and for S_2 (right).

Control of the ground plane

As the linear array designed in Chapter 3 is extracted from the 2D case developed in this Chapter, some preliminary assessments can be taken. Indeed, considering the previous linear array case, the ground plane is deformed thanks to three actuators distributed uniformly (one is placed under the center of the border cells and the last one under the middle reflecting element). Therefore, by extending this principle to the 2D case, 9 actuators are distributed under the 2D array. They are placed under the cells $Cell_{l,1}, Cell_{l,11}, Cell_{l,21}$, for $l = [1, 11, 21]$.

Considering that only 9 actuators are used to control the ground plane deformation, the prediction model detailed in the previous chapter cannot be applied to every line. Hence, a specific model for the 2D case must be specified, and it is detailed in the next section.

Hypotheses and primary assessments

The hypotheses are the same as the ones for the linear array. The ground plane is then considered locally plane under each cell and the cells composing the database are the ones presented in Chapter 2.

For the sake of simplicity, some hypothesis have been taken to initialize the definition of the design methodology. Hence, as the linear array previously presented was extracted from the case studied in this section, it is used as the starting point to extend the methodology. Indeed, it has been decided that all actuators with the same value of m will have the same displacements. Therefore, the ground plane shape could be considered to a wavy sheet.

Thanks to this, the actuators distribution and their applied displacements are known which allows an easier cells selection as the one presented before for the initialization of the *RRA* panel. Indeed, the cells selection will be done considering as inputs the database, the known deformations, and the ideal set of phases to choose the cells with the lowest average phase error while considering both coverage S_1 and S_2 . This type of selection is similar to the second cells selection made previously.

4.2.2 Application of the extended design methodology

As explained in the previous section, the extension of the methodology is made considering the same ground plane shape profile for each linear array composing the 2D panel. Even if same actuators displacements are used, new boundary conditions have to be defined and considered for the mechanical model of the ground plane deformation. The predicted shapes will then be used to select the cells.

Boundary conditions definition

According to [39], the different types of mechanical boundaries used for this new prediction model of the ground plane shape are:

- Fixed rim
- Partially fixed rim with free radial displacement
- Free rim with one fixed in rotation and translation. Another one is fixed for one rotation

Moreover, the existing re-shapeable reflector tested in [39] assumes a surface-to-actuator interfaces rotation free. This interface is produced in reality thanks to two spherical hinges, which could be blocked in rotation or translation thanks to a specific part integrated on it, linked with a rod of a certain length. Figure 4.4 illustrates the concept of this interface between the flexible ground plane and the actuator. Note that the longer the rod is, the less interferences of the actuators strokes will be felt.

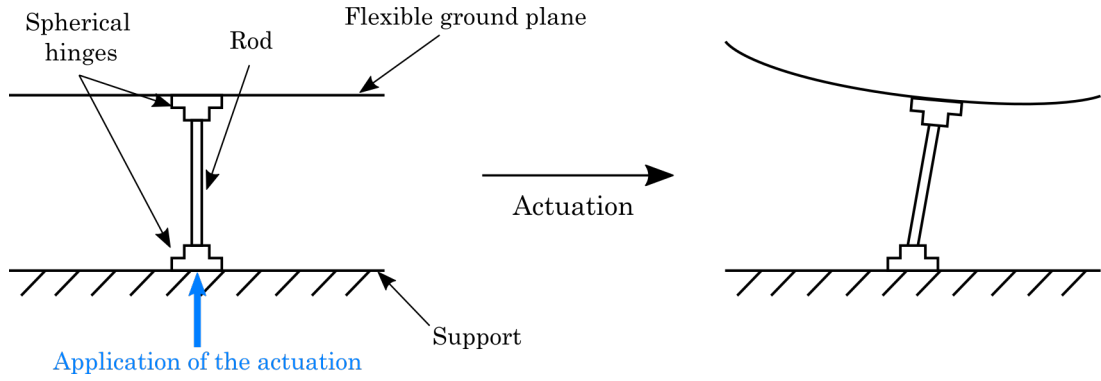


FIGURE 4.4: Representation of the interface between the surface and the actuators.

The new model for the prediction of the ground plane shape considers these surface-to-actuators interfaces, the rods, and the same boundary conditions as in [39]. Nevertheless, the length of the rod is unknown. Hence, on the advice of specialists from *Large Space Structures* the rods length has been set to 80 mm. Figure 4.5 illustrates the boundary conditions applied for this new model.

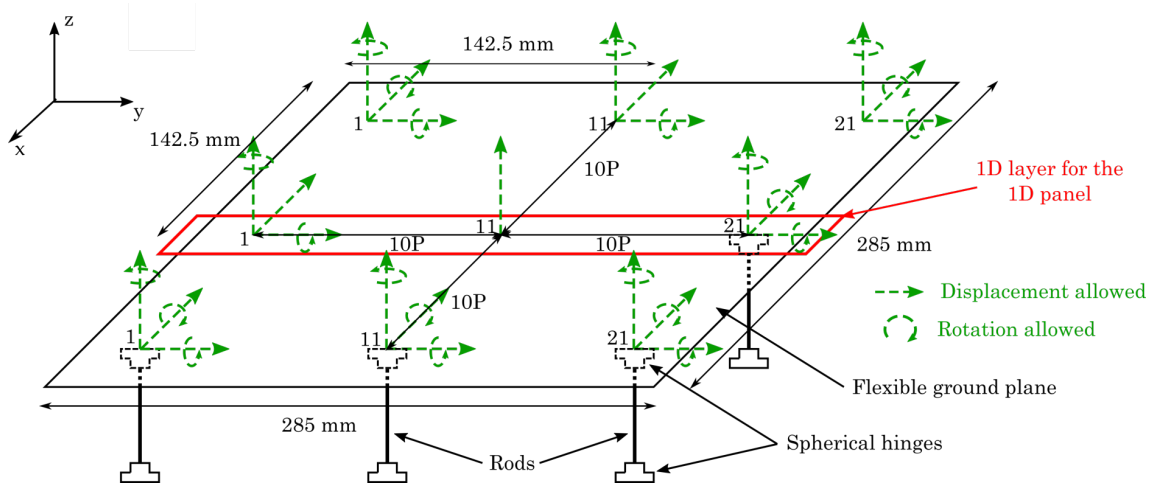


FIGURE 4.5: Boundary conditions of the ground plane shape prediction model for the 2D array.

Actuators displacements identification

According to the linear array design methodology, the displacements which must be applied to each actuator are deduced from the linear approximation of the ground plane ideal deformations. As explained previously, they are initially known as they are extracted from the linear array design defined in Chapter 3. Moreover, it is important to note that 9 actuators are considered but gathered three per three as n° 1, 11, and 21 in Table 4.1.

<i>Number of the actuator: m</i>	1	11	21
Displacement for S_1	3.23 mm	8.77 mm	3.28 mm
Displacement for S_2	8.50 mm	3.04 mm	8.36 mm

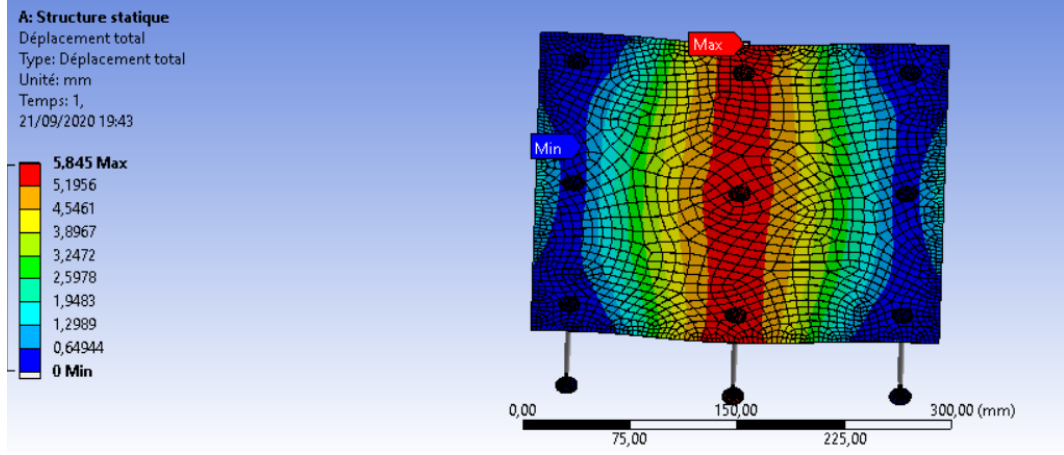
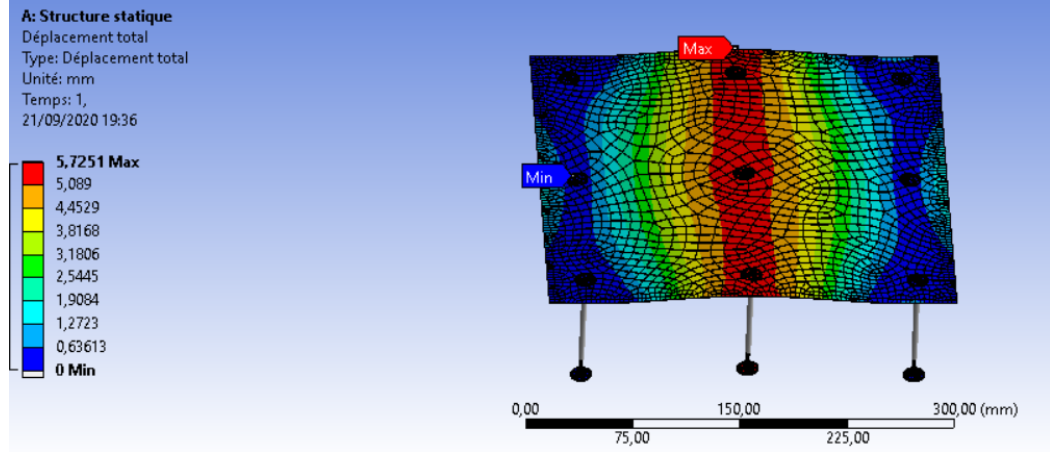
TABLE 4.1: Displacements applied to the actuators for each configuration for the 2D panel.

Prediction of the ground plane shapes and cells distribution

Figures 4.6 and 4.7 illustrate the ground plane shapes for S_1 and S_2 while applying the displacements gathered in Table 4.1 to the actuators. In these figures, the displacements of each membrane node are computed relatively to the rest position of the membrane h for $l = 11$ and $m = 21$ (noted $h_{11,21}^{S_i}$, with S_i the coverage targeted). Table 4.2 presents the actuators displacement normalized relatively to $h_{11,21}^{S_i}$ for each coverage considering the reference actuator displacement.

Number of the actuator	1	11	21
Displacement for S_1	-0.05 mm	+5.49 mm	0 mm
Displacement for S_2	0.14 mm	-5.32 mm	0 mm

TABLE 4.2: Displacements applied to the actuators for each configuration for the 2D panel

FIGURE 4.6: Predicted ground plane shape for S_1 .FIGURE 4.7: Predicted ground plane shape for S_2 .

As in Chapter 3, an approximation of the predicted shape profile for each linear array composing the 2D panel is extracted. Then, using this set of predicted deformations, the cells database, and the set of ideal phase laws, the cells are selected. As for the second selection of cells done for the linear array design, the cell selected for each location is the one which minimizes the phase error considering both coverages S_1 and S_2 . Figure 4.8 presents the deduced layout for the 2D array.

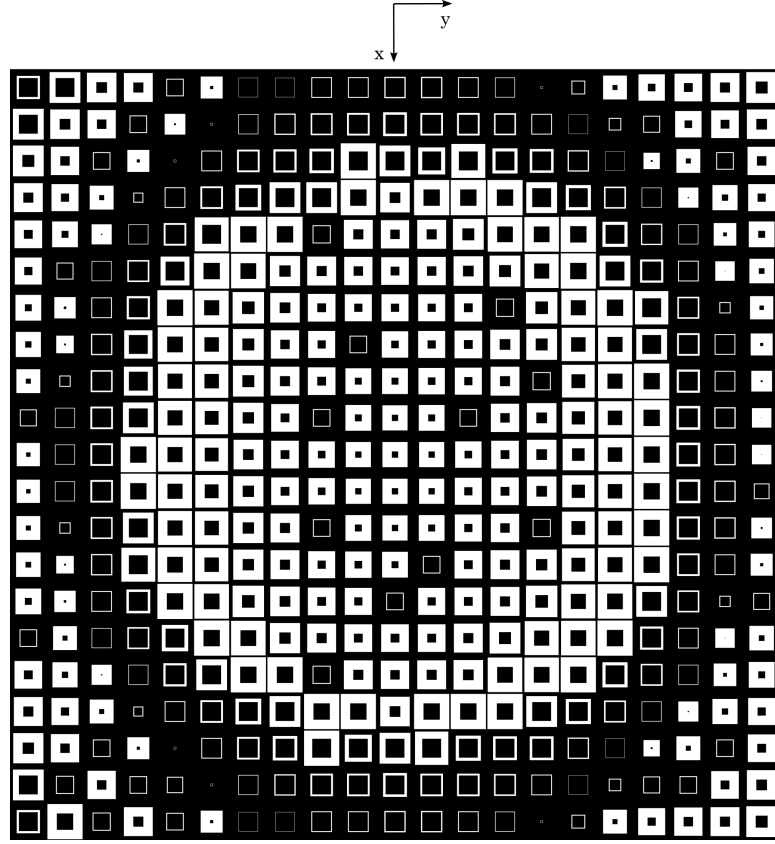


FIGURE 4.8: Design of the 2D panel deduced using the predicted ground plane shapes.

The layout illustrated Figure 4.8 does not present the expected symmetry around the y -axis induced by the ideal phase distribution over the panel. This is explained by the mechanical boundary conditions which are not symmetrical. Hence, for example, the predicted shape profiles extracted for linear arrays $l = 1$ and $l = 21$ are not identical in both S_1 and S_2 configurations.

Using the layout and the set of predicted deformations, it is possible to determine the predicted directivity patterns and to compare it to the ideal ones. This comparison is assessed in the next section.

Directivity patterns computation

The ideal and predicted directivity patterns derived from the array factor computation using the designed layout, the cells database, and the set of predicted deformations are presented in Figure 4.9.

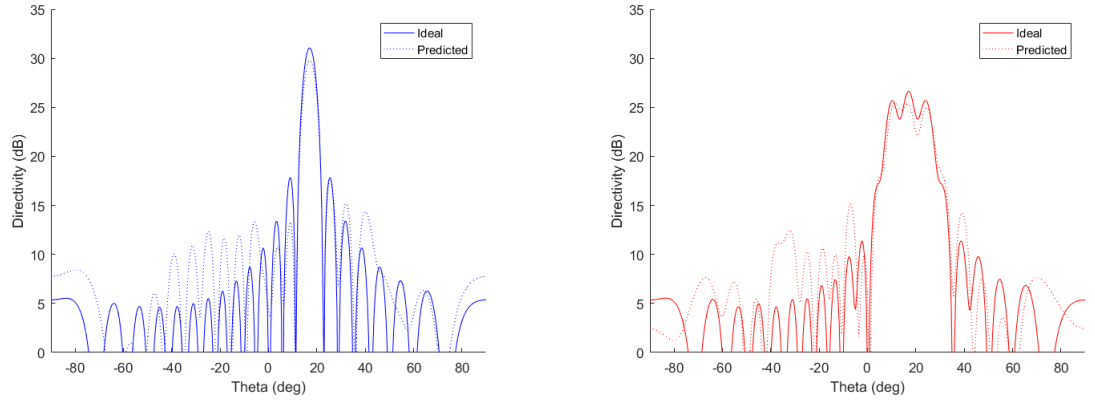


FIGURE 4.9: Predicted directivity patterns obtained, Cut-plane $\Phi = 90^\circ$ for S_1 (left) and for S_2 (right).

Figure 4.9 presents good correlation between the predicted and the ideal directivity patterns. The difference between the main lobes and the secondary lobes in the case of ideal and provided directivity patterns for both coverages could be explained by the cells selection done. Indeed, the cells are selected in order to provide the minimum average phase error considering both coverages. Nevertheless, considering the cells database and the set of predicted deformations and ideal phases targeted, an error of phase might exist. Figure 4.10 illustrated the distribution of phase error for both coverages.

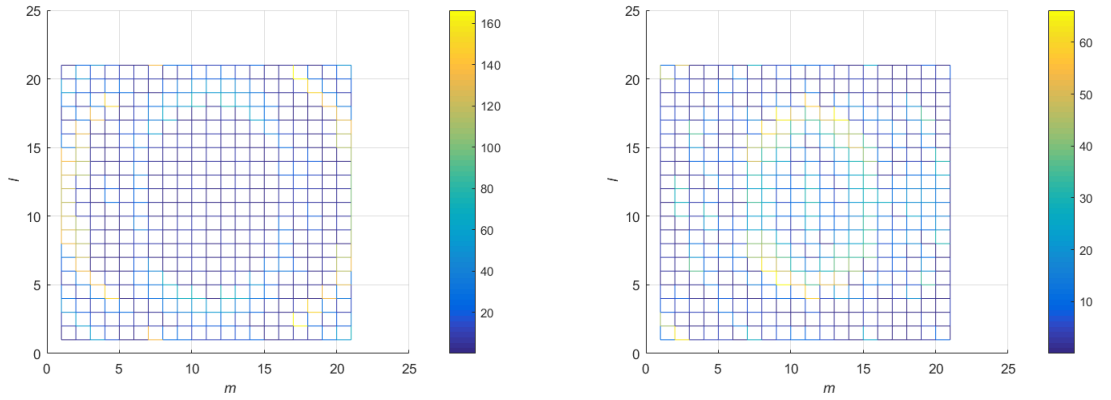


FIGURE 4.10: Distribution of the average phase error for S_1 (left) and for S_2 (right).

This average phase error can have a variable impact on the directivity patterns as it could be noticed in Figure 4.9 and Figure 4.10. Figures 4.11 and 4.12 illustrate the predicted radiation patterns attributed to this layout for both coverages. With u et v defined respectively with the Equation 4.1 and 4.2.

$$u = \sin(\theta)\cos(\phi) \quad (4.1)$$

$$v = \sin(\theta)\sin(\phi) \quad (4.2)$$

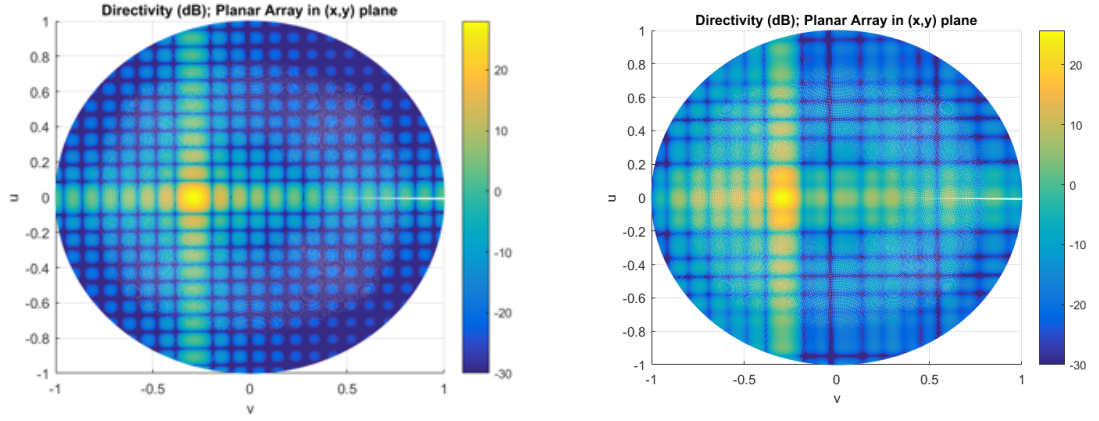


FIGURE 4.11: Radiation patterns obtained for the ideal case of S_1 (left) and the predicted one (right).

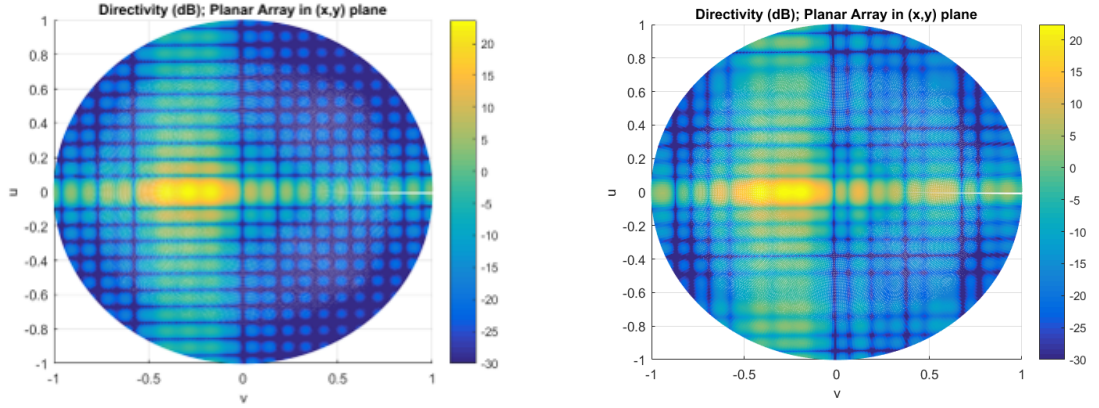


FIGURE 4.12: Radiation patterns obtained for the ideal case of S_2 (left) and the predicted one (right).

Figures 4.11 and 4.12 show higher secondary lobes than the ideal radiation patterns and a low loss of directivity. Nevertheless, these results and the validation of the linear array design methodology using fullwave simulation shows enough interest to prove this concept thanks to a breadboard.

4.3 Breadboard

4.3.1 Preliminary remarks

The first measurements campaign revealed a mistake in the followed design methodology of the breadboard when passing from the 1D to the 2D. The results in the previous sections are the ones we obtain once this error is corrected (i.e. using the optimal layout). Unfortunately, it was not possible to account for this correction in the breadboard since the *RA* was already fabricated when it was discovered. Hence, the results presented in this section have been obtained with a non optimal layout. Figure 4.13 shows the cells distribution used for the measurements.

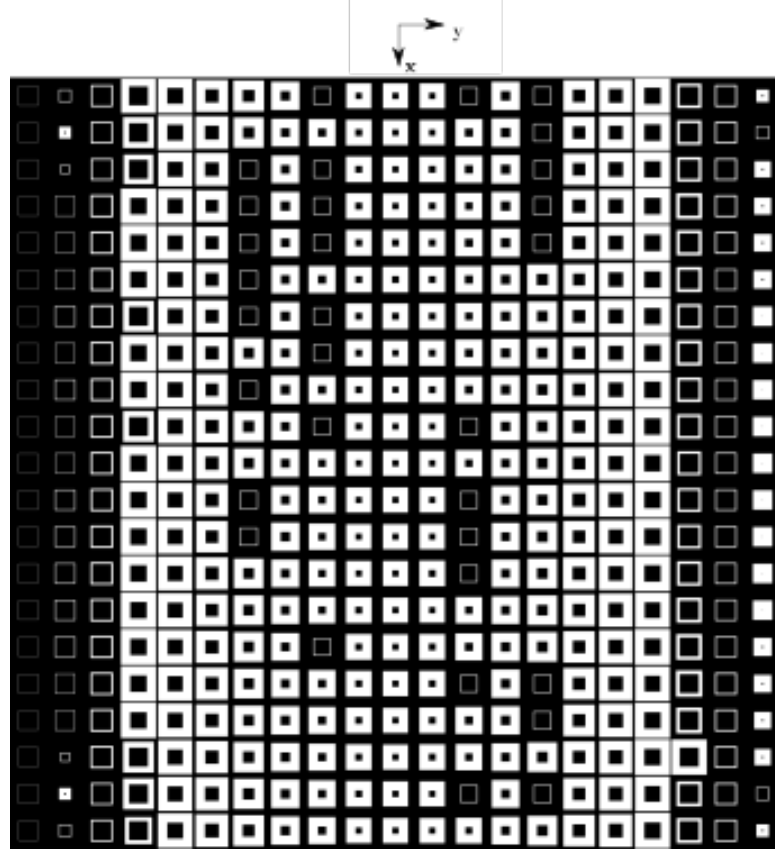


FIGURE 4.13: Cells distribution for the 2D panel.

The main principle of this concept is the reconfiguration thanks to the modification of the ground plane's shape. Therefore, we decided instead to try to compensate for the error by applying the appropriate displacement on each actuator depending on

the configuration targeted S_1 and S_2 . We believe it is enough for a proof of concept, even if it doesn't allow, of course, to reach optimal performance. Moreover, it is an additional demonstration of the interest of such a reconfiguration technique as it means that fabrication tolerances may be corrected easily by re-computing the predicted ground plane shapes.

4.3.2 Objectives and inputs of the breadboard

The breadboard testing aims to validate the concept of a reconfigurable reflectarray based on modifying its ground plane shape. It also helps to evaluate the design methodology developed in this thesis.

Finally, this section considers that the demonstrator can be divided into several parts illustrated in Figure 4.14:

- The rear-structure: it is the plate which supports the actuators and the whole antenna
- The reflectarray panel: it is composed of a substrate with printed reflecting elements
- The ground plane
- The interfaces between the actuators and the ground plane
- The support of the reflectarray panel that ensures good stretching of the substrate, also called frame
- The feed and its tower

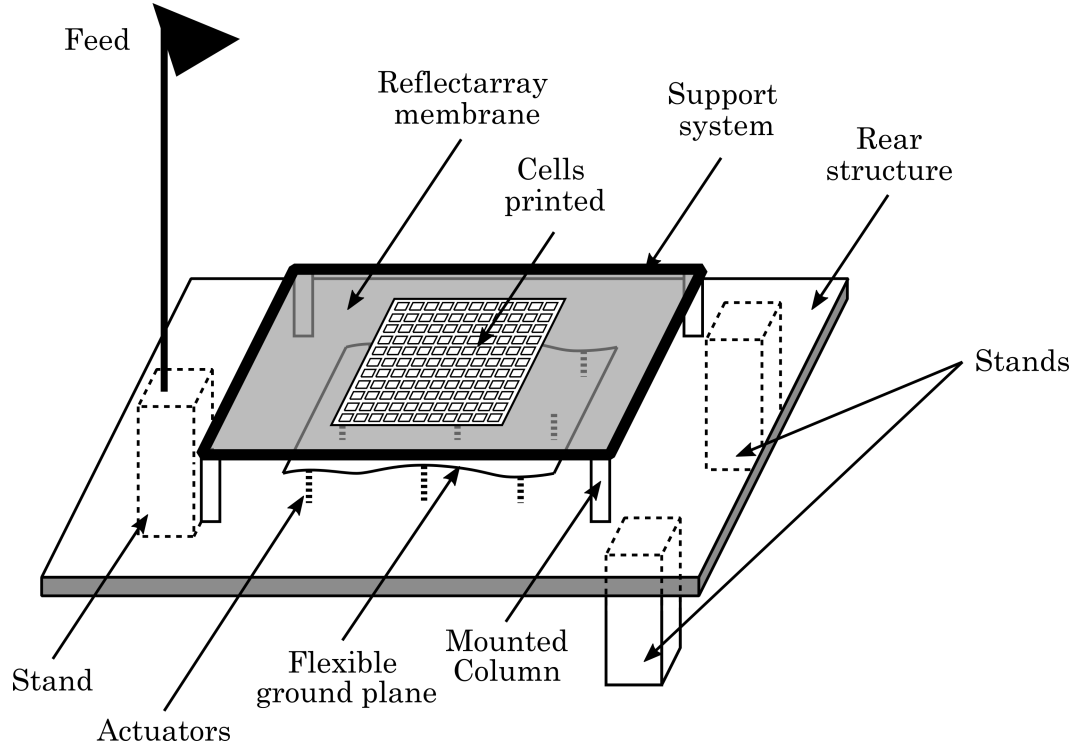


FIGURE 4.14: Scheme of the whole structure.

The parts need to be assembled with respect to the integration constraints induced by the necessity to ensure correct distance between the cells composing the panel and the ground plane.

4.3.3 Identification of the new ground plane shapes

The identification of the two ground plane shapes has been made considering the cells distribution. Due to the limited number of actuators (only 9), only few possibilities of ground plane shapes exist.

To identify the new ground plane shapes for each coverage, the first step is to identify the ideal deformation for each line (along the x -axis) under which the actuators are placed.

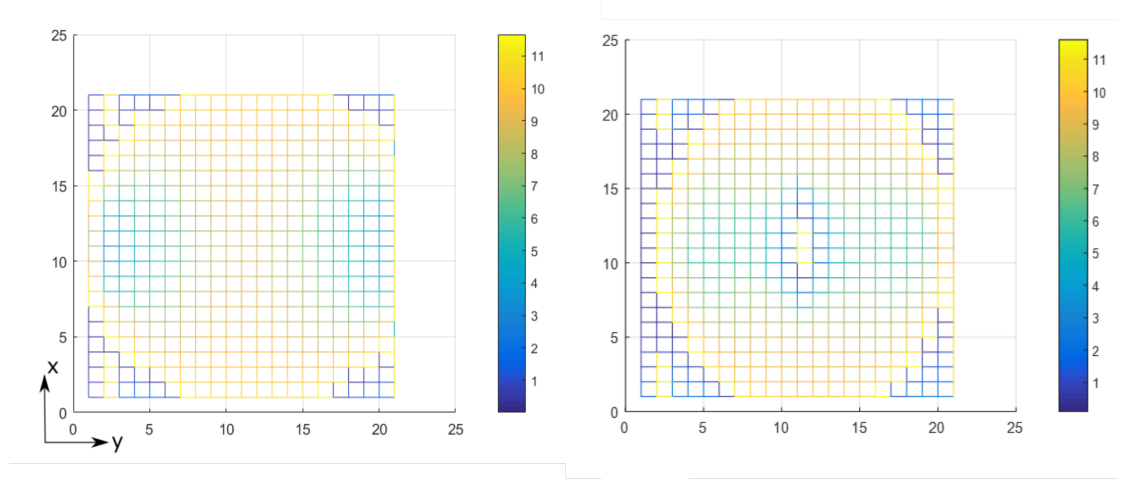
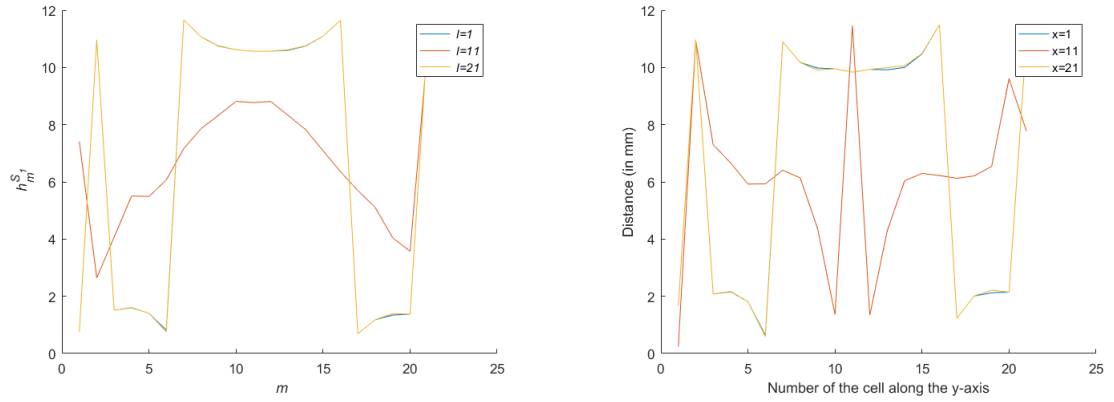
FIGURE 4.15: Ideal deformations for S_1 (left) and S_2 (right).

Figure 4.16 presents the ideal value of $h_{lm}^{S_i}$ for $l = [1, 11, 21]$ which are the ideal distance for the $Cell_{ml}$ considering the coverage S_i .

FIGURE 4.16: Ideal deformations for the lign n° 1, 11, and 21 extracted from the 2D panel for S_1 (left) and S_2 (right).

In Figure 4.16, the symmetry of the antenna configuration along the y -axis is highlighted by the identical ideal deformation identified for the lines n°1 and 21 for both coverages.

Figure 4.17 presents the ideal value of $h_{lm}^{S_i}$ considering a possible additional distance shift equal to $\frac{\lambda_0}{2}$ while it is possible to smooth the ground plane deformations. Indeed, as it can be noticed in Figure 4.17 for the central cell in the configuration S_2 , the additional distance is not applied due to some technical constraints with the maximal motion applicable whereas it could be interesting. Hence, it was not

possible to achieve a distance higher than 15 mm from the model in the case of our prototype.

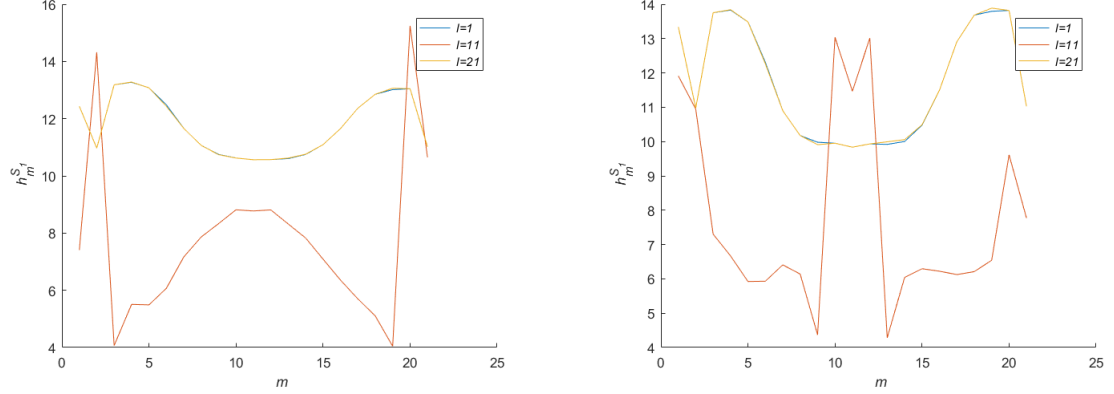


FIGURE 4.17: Ideal deformations considering the additional distance technique for S_1 (left) and for S_2 (right).

4.3.4 Identification of the actuators displacement

The ideal deformations (cf. Figure 4.17) are then linearly approximated to identify the displacement values of each actuator to apply in the 2D model on Ansys Mechanical. The predicted deformations issued by the 2D model are then imported and used to compute, with the array factor, the directivity patterns attributed to this set of predicted deformations applied and the cells distribution established.

As the predicted deformation of each configuration does not perfectly correspond to the ideal deformation targeted, an iteration is made on the displacement of each actuator to find the best compromise between the RF and the mechanical performance.

For the sake of clarity, only the final set of displacements applied for each configuration considering the bottom of the substrate as a reference height are noted in Table 4.3 for S_1 and Table 4.4 for S_2 .

S_1	$y=1$	$y=11$	$y=21$
$x=1$	12.07 mm	10.02 mm	12.07 mm
$x=11$	1.50 mm	8.77 mm	1.50 mm
$x=21$	12.07 mm	10.02 mm	12.07 mm

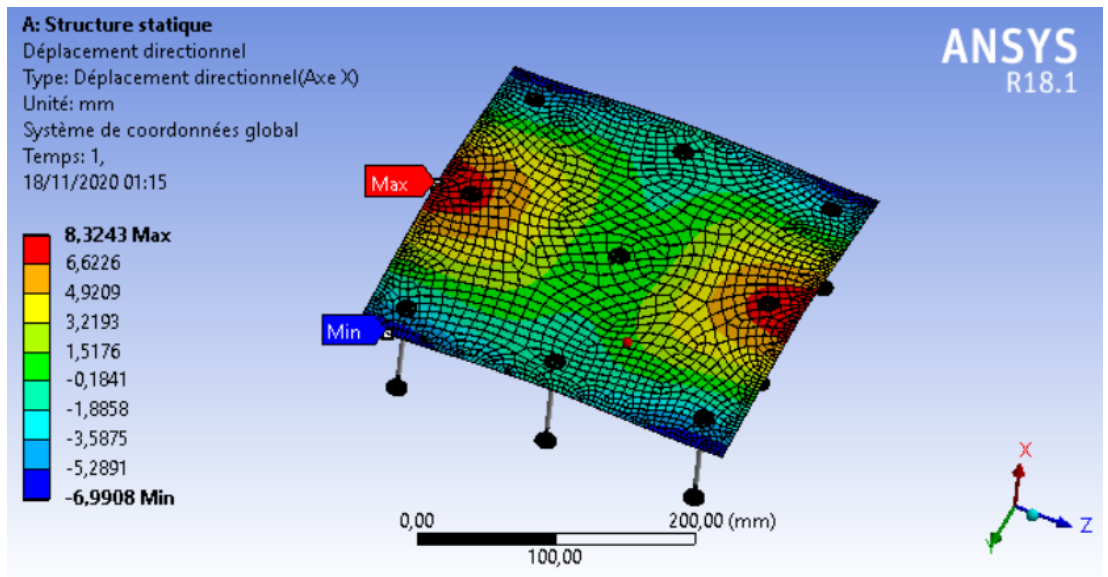
TABLE 4.3: Displacements applied to the actuators for configuration S_1 .

S_2	$y=1$	$y=11$	$y=21$
$x=1$	12.56 mm	7.84 mm	12.56 mm
$x=11$	9.76 mm	4.00 mm	9.76 mm
$x=21$	12.56 mm	7.84 mm	12.56 mm

TABLE 4.4: Displacements applied to the actuators for configuration S_2 .

4.3.5 Prediction of the ground plane shape

Figure 4.18 and Figure 4.19 illustrate the results of the 2D model while applying the displacements given in Tables 4.3 and 4.4 and the same mechanical boundary conditions as the ones presented previously. The displacements are applied to the actuators in the prediction model for both coverage considering that the reference $h_{lm}^{S_1}$ is $h_{11,11}^{S_1}$.

FIGURE 4.18: Simulation of the ground plane shape for S_1 , also called predicted deformation.

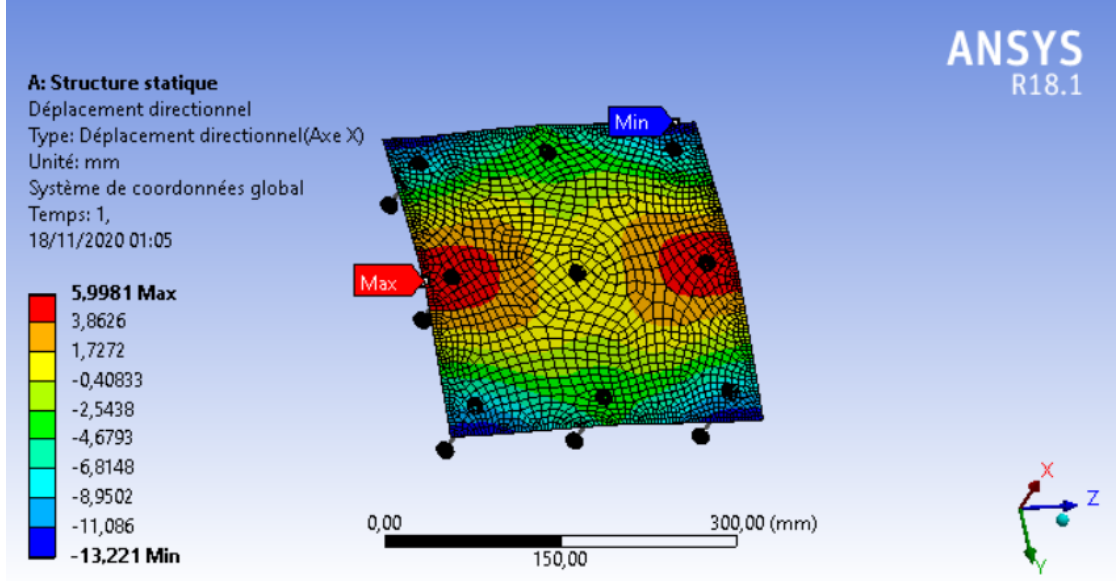


FIGURE 4.19: Simulation of the ground plane shape for S_2 , also called predicted deformation.

4.3.6 Predicted RF results

Figure 4.20 presents the directivity patterns computed with the designed RA panel (cf. Figure 4.13), the predicted deformations and the information extracted from the database. These are deduced using the deformations presented in the previous section.

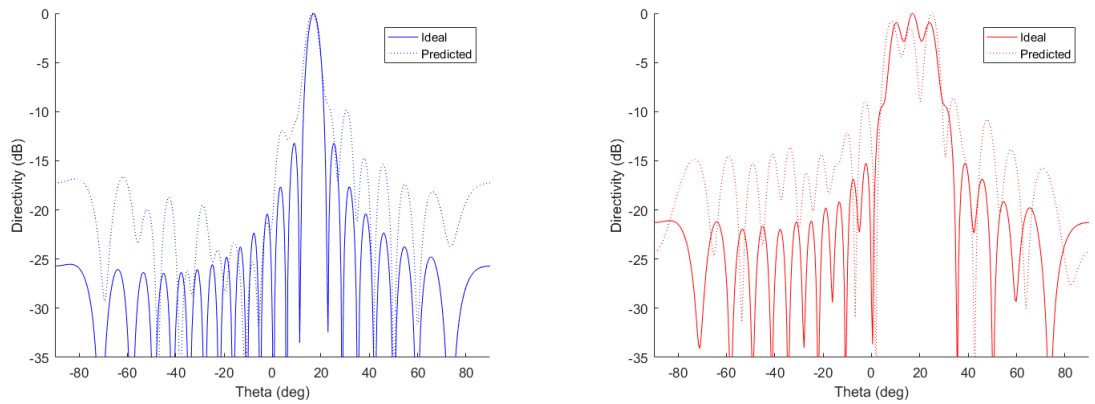


FIGURE 4.20: Radiation patterns, Cut-plane $\Phi = 90^\circ$ for S_1 (left), and S_2 (right) with the realistic deformations.

In Figure 4.20, the predicted and ideal directivity patterns seem to have good correlation for the first configuration S_1 while presenting a degradation of the

main lobe for S_2 . For S_1 , the main lobe and its aperture are comparable to the ideal ones while the second configuration presents more discrepancies, notably around $\theta=30^\circ$.

Finally, the (u, v) patterns are shown in Figure 4.21 and 4.22 for respectively S_1 and S_2 .

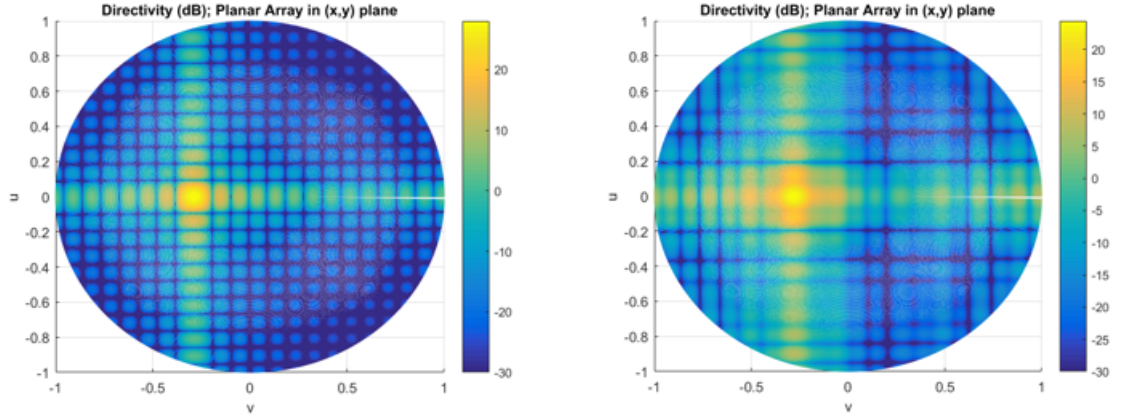


FIGURE 4.21: Radiation patterns obtained for the ideal case of S_1 (left) and the computed one (right).

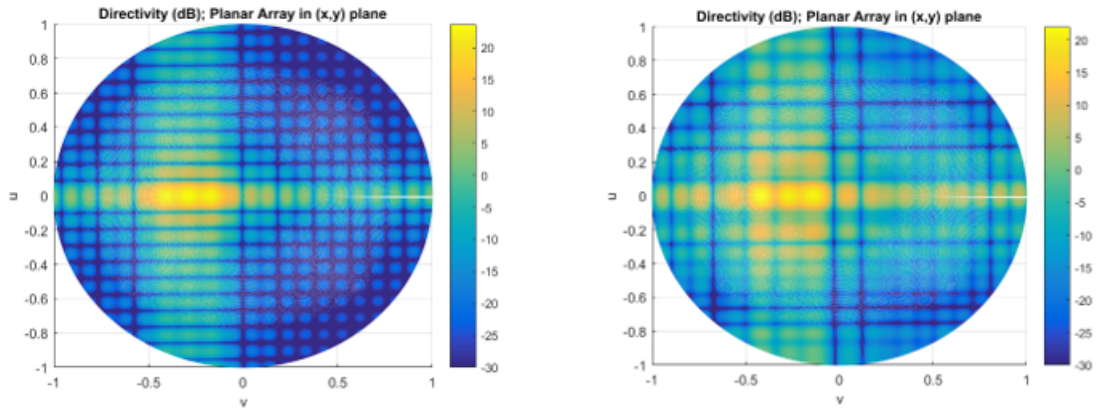


FIGURE 4.22: Radiation patterns obtained for the ideal case of S_2 (left) and the computed one (right).

The radiation patterns computed for S_1 gives acceptable results (cf. Figure 4.21), even if it presents higher secondary lobes than the ideal one. For S_2 in Figure 4.22, the identified deformation does not give satisfactory results. Indeed, Figure 4.22 shows the enlarged lobe as targeted, but big ripples are observed. Nevertheless, the difference of maximal directivity between the ideal and predicted values could be explained as the deformation is not optimized [129].

4.3.7 Outputs of the breadboard definition

Considering the previous results, it has been decided that only the first configuration will be studied further in this chapter. Nevertheless, it must be underlined that the RF performance in the case of the second configuration would have been better if it had been possible to apply a higher distance between the cell and the ground plane.

4.4 Design and fabrication of the breadboard

This section details the technical requirements that the demonstrator must complete to be coherent with the developed models. Each part of the prototype is presented to propose a global overview of the assembly.

4.4.1 Constraints of integration

The parallelism between the reflectarray panel, the rear-structure, and the membrane must be ensured. Indeed, the rear-structure supports most of the parts, such as the actuators. Hence, it is necessary to ensure good planarity of this part with the reflectarray panel as it will support the actuator and so the ground plane.

Moreover, the reflectarray panel needs to be positioned at a certain distance from the support structure and the membrane. The fixation of this panel must ensure its stability during the test but also its planarity. That is why the reflectarray panel must be stretched correctly.

4.4.2 Rear-structure

The rear structure is composed of a support plate in steel of 596 mmx496 mmx10 mm and by three stands supporting it. To ensure the horizontality of the structure, two of them have adjustable height capability. The stands are bolted to the plate with nuts and bolts with a diameter of 5 mm.

The accuracy of the support plate manufacturing needs to be high to ensure good positioning of the mounting columns, the actuators, and the stands. The mounting

columns are steel parts which separate the panel and its supports from the rear-structure. These columns are also used while placing and gluing the ground plane on the interfaces to ensure parallelism.

Figure 4.23 shows the rear-structure mounted on the three stands (which will be removed during the RF measurements), and the actuators.

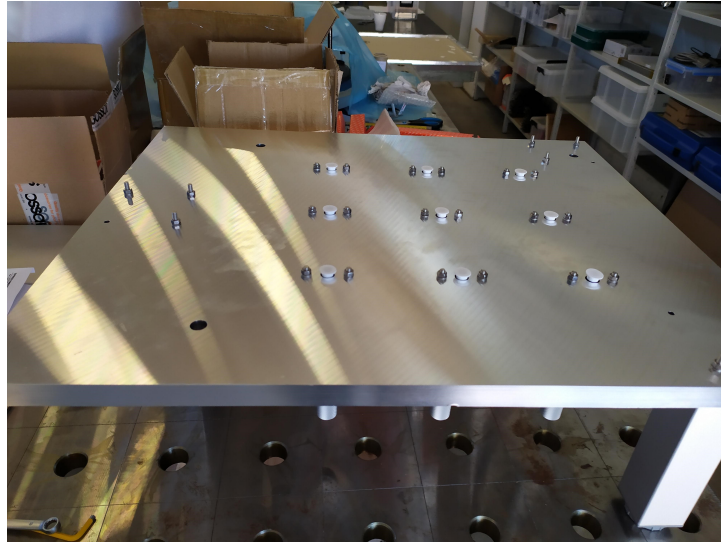


FIGURE 4.23: photo of the rear-structure with the actuators mounted.

A photogrammetry test has been realized on the support plate to ensure its planarity. Figure 4.24 is a picture of the test.

Photogrammetry tests consist of measuring and interpreting photographic images to obtain information about a targeted object. Targets are stuck on the object to reconstruct. The photogrammetry gives the coordinates of the points associated with these targets.

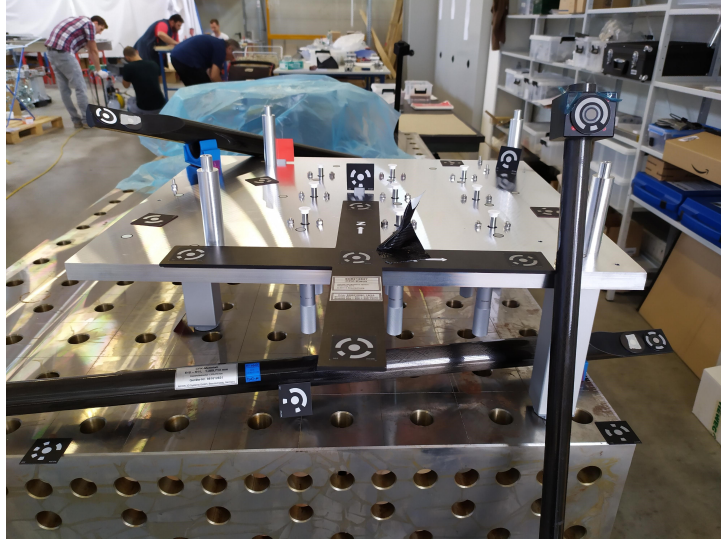


FIGURE 4.24: photo of the rear-structure prepared for the photogrammetry tests.

The surface established thanks to the photogrammetry tests is compared to a flat plane constructed by taking three reference points (targets). The average error between the surface tested and the ideal plane is computed to obtain the root-mean-square (*RMS*). This test has revealed a *RMS* which is approximately equal to 0.04 mm, ensuring good planarity of the rear-structure. It is important as it supports the whole assembly. Consequently, an error of planarity could impact the parallelism between the *RA* panel and the ground plane while it is considered as flat for the initial state of the structure.

4.4.3 Actuators and surface-to-actuator interface

Linear actuators are the most suitable for the reconfigurable reflectors because of the high required strokes. The ground plane is re-shaped thanks to 9 actuators distributed uniformly over the panel, as explained in the previous chapter. For this breadboard, the main specifications of the actuators are:

- Controllable manually
- Motion range higher than $\frac{\lambda}{2}$ (between 0 mm to 50 mm)
- A high accuracy (around 0.004 mm)

Hence, in order to respect this requirements, 9 manual micrometers "Mitutoyo" referenced "151-259" have been used as actuators for this breadboard.

To apply the good mechanical boundary conditions, some specific parts have been designed to block rotation or translation around, or along the desired axis. This system can be integrated over the spherical hinges and moved manually, which allows flexibility in the model. Hence, for each actuator, one of these parts is integrated on the spherical hinge glued on the flexible membrane (at the end of the rod) while another one is fixed on the actuator.

Note that specific ones have also been used to place the membrane and as anti-gravitational systems during the RF measurements. This was to avoid gravity effects on the deformation of the ground plane as it is not positioned horizontally but vertically during the test. Figure 4.25 is a photo of this assembly step with a blocking system to ensure the good parallelism between the rear-structure and the flexible ground plane.

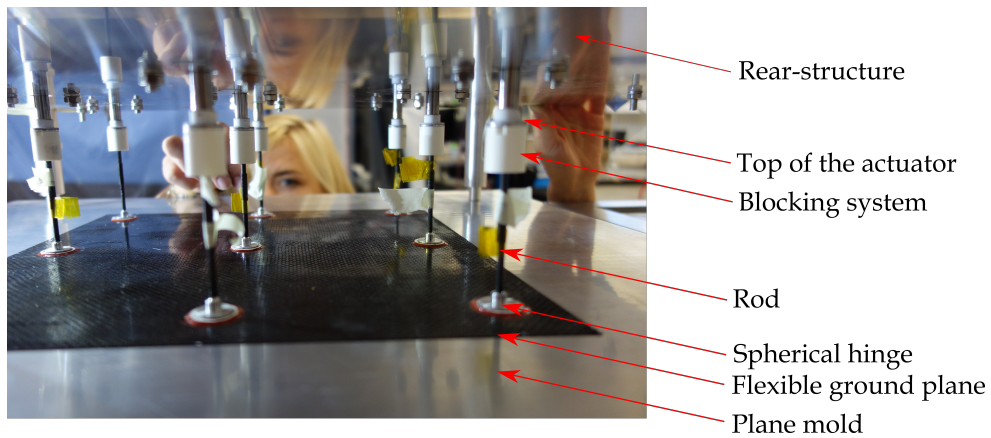


FIGURE 4.25: Assembly process of the actuators, the membrane and their interfaces.

Figure 4.26 is a picture of the final mounting of the actuators, the membrane, and the interfaces.

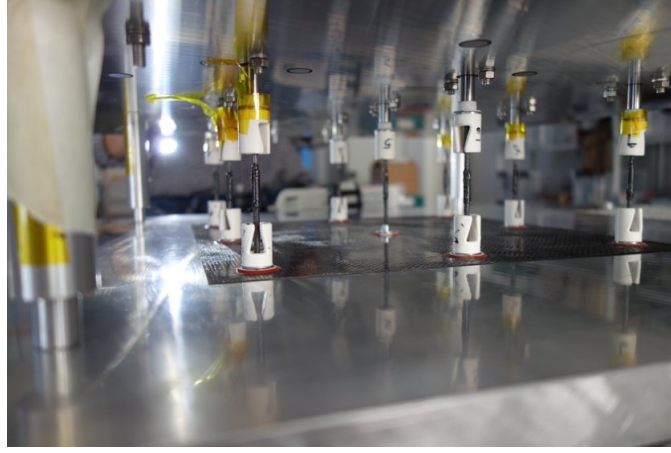


FIGURE 4.26: Assembly of the actuators, the membrane and their interfaces.

4.4.4 Ground plane

The ground plane is made of 3-layer biaxial-CFRS of $286 \times 286 \text{ mm}^2$ ($=12.25\lambda \times 12.25\lambda$). The dimensions of the shell-membrane are equivalent to the surface of the RA-membrane where the cells are printed with a margin of approximately 21 mm at each border to prevent the effect of the deformation. Indeed, this margin ensures total coverage of the RA by the ground plane when it will be deformed.

The characteristics of the material considered have been estimated to:

- Equivalent flexural modulus : $E_{xx}=E_{yy}=3200 \text{ MPa}$,
- Shear modulus: $G_{xy}=6.72 \text{ MPa}$, $G_{xz}=G_{yz}=10 \text{ MPa}$
- Poisson's ratio: $\nu_{xy}=0.8$
- Thickness: $e=0.321 \text{ mm}$

To place the shell-membrane over the actuators, a plane surface with high accuracy is needed. It is a plate on which four steel mounting columns are placed. Figure 4.27 shows the gluing process of the ground plane while using the mounting columns.

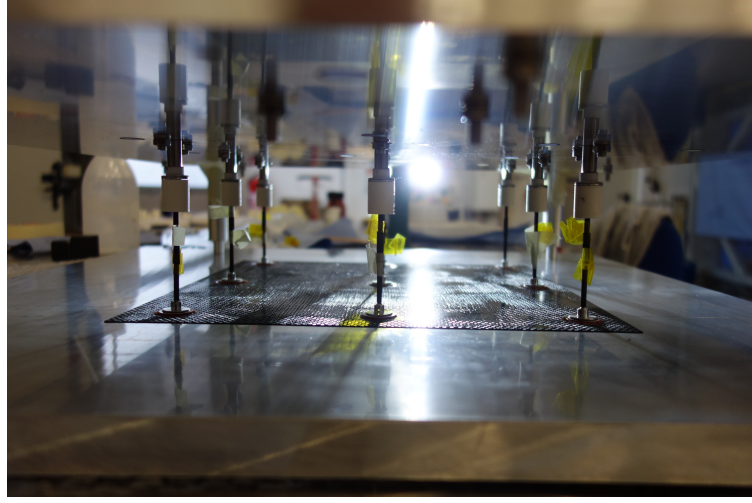


FIGURE 4.27: Photo of the ground plane assembly.

The mounting columns are inserted at one extremity into specific holes in the rear-structure and at the other extremity on the mold. The ground plane is placed on the plane surface free of constraints. Then, the interfaces which are glued on the top of the actuators are positioned and glued on the membrane by a motion of the actuator until they touch each other. This technique ensures parallelism of the rear-structure with the membrane. This is also ensured thanks to the columns manufacture accuracy.

Finally, the specific blocking systems are added on top of the actuators (integrated on the spherical hinges) depending on the desired mechanical boundary conditions. To block rotations or translations, some elements are added over the spherical hinge.

4.4.5 *RA* panel and its support system

The *RA* panel is a PTFE of $416 \times 466 \times 0.5 \text{ mm}^3$ RT5880 with a permittivity equal to 2.2. Second-order Phoenix cells are printed in copper on the dielectric substrate. The *RA* panel is aligned with the center of the shell-membrane and the actuator at the center. Moreover, the panel needs to be parallel to the shell-membrane and consequently to the rear-structure. The thin thickness of the *RA* panel leads to the necessity to stretch it in order to avoid bounding effects. Therefore, the substrate will be handled by a frame.

The frame is the support of the *RA* membrane and, consequently needs to ensure the parallelism between itself and the support structure (and the ground plane at its initial state). Hence, the mounting columns used while gluing and placing the ground plane to ensure its positioning are then used to support and to align the frame.

Figure 4.28 illustrates the assembly with the flexible membrane and its frame.

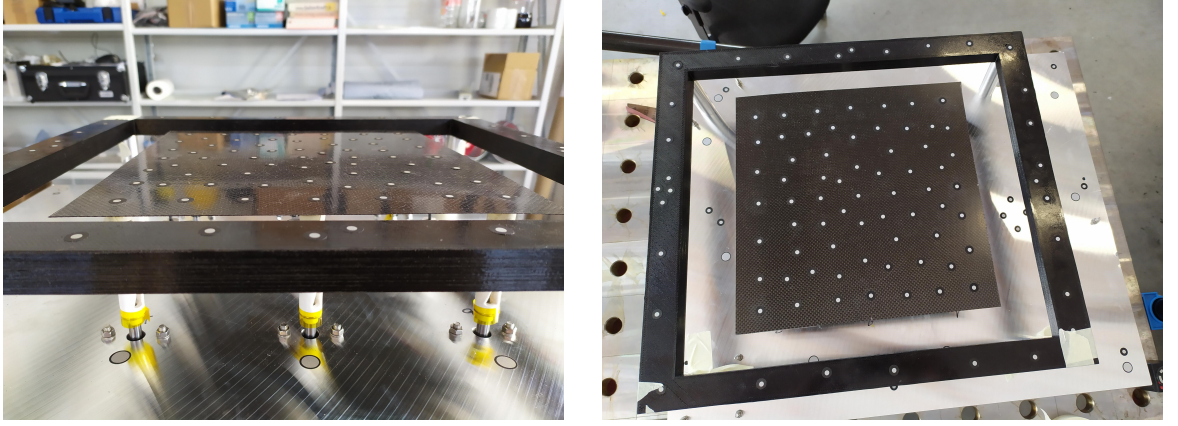


FIGURE 4.28: Assembly of the frame and the flexible ground plane.

4.5 Control and prediction tests of the ground plane shape

The uncertainties in the conception of the *RRA* with flexible ground plane rely mostly upon control and prediction of the deformation.

4.5.1 Photogrammetry tests definition

The deformation of the ground plane needs to be repeatable as the antenna must be reconfigurable. Hence, the tests made to validate the ground plane shape need to be done several times to ensure its repeatability. The photogrammetry is applied to the flexible membrane and the rear-structure to reconstruct using targets the ground plane shape.

In Figure 4.29, the targets are the white spots stuck at several locations over the antenna. These targets can be also viewed in Figure 4.28

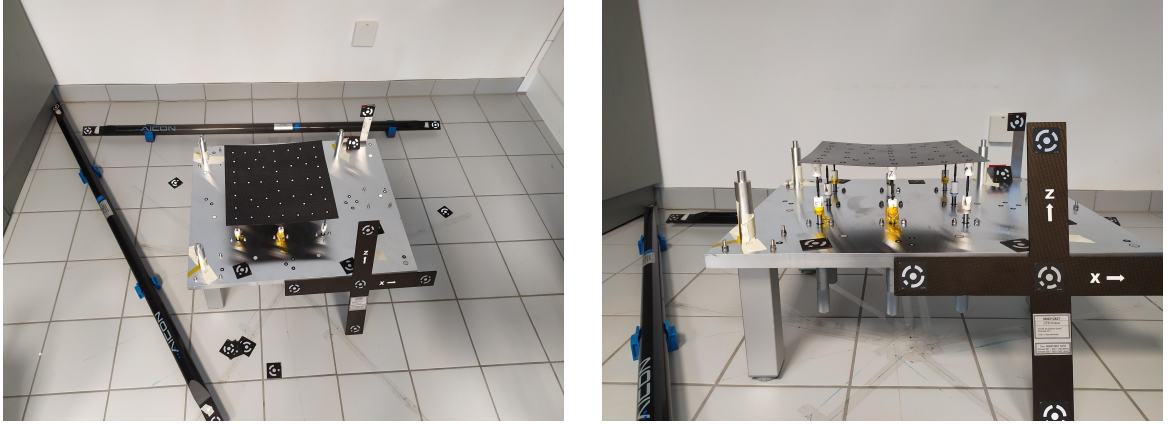


FIGURE 4.29: Setup of the photogrammetry.

The interpretation of the taken pictures leads, in the frame of photogrammetry test, to a series of points with their coordinates, which corresponds to the location in the space of the targets. In our case, three specific points associated with three targets placed on the rear-structure plate are taken to define a reference plane. The distances between each point associated with a target located on the ground plane and the reference plane are derived. Then, these distances are used to plot the ground plane shape.

The series of tests consist of three different load cases repeated several times:

- 4 initialization cases which correspond to a flat ground plane. All actuators are in the same motion state
- 2 deformations corresponding to the first configuration
- 2 deformations associated with the second configuration

The first test is the initialization case, then the series alternate between deformation case and initialization one.

It is important to note that these tests have been done considering the deformations presented in the first section of this chapter. Nevertheless, they give sufficient information on the accuracy of the ground plane shape and the repeatability of the deformations, even if the deformation is less complicated.

One target is located in the center of the ground plane, and as for the actuator displacements in the simulation, it is now considered as a reference for the coordinates.

By interpolating the points obtained from the photogrammetry tests, it is possible to compare the predicted ground plane shapes with the measured ones. The center of each computed surface is superimposed as the central actuator is considered as a reference. This reference is then used to compare the predicted and the measured shape. The accuracy of the photogrammetry results has been evaluated between 0.005 mm and 0.009 mm which allows to prove the correlation between the mechanical model and the reality. Both predicted and measured ground plane shapes are discretized to be divided in 21x21 nodes (K is the total number of nodes) associated with the center of each cell composing the panel. The difference of displacement for $Cell_{lm}$ is noted $\Delta h_{lm}^{S_i}$ for both coverage S_1 and S_2 . Nevertheless, even if these tests are accurate enough to validate the mechanical model, it presents some uncertainties due to the manual procedure notably for the localization of the targets on the demonstrator compared to the distribution of the actuators.

The root mean square *RMS* error can be computed with the Equation 4.3 in order to evaluate the shaping accuracy between the predicted and the measured ones.

$$RMS = \sqrt{\frac{\sum_{l=1}^{21} \sum_{m=1}^{21} (\Delta h_{lm}^{S_i})^2}{K}} \quad (4.3)$$

4.5.2 Photogrammetry tests results

Table 4.5 presents the *RMS* values for each test realized for both coverages.

	S_1	S_2
Test 1	0.51 mm	0.78 mm
Test 2	0.74 mm	0.65 mm

TABLE 4.5: *RMS* computed for each photogrammetry test.

The average *RMS* obtained for the initial state is equal to 0.14 mm.

In [39], some photogrammetry tests have been realized on a shaped of 500 mm diameter reflector deformed thanks to 19 mechanical actuators and developed by Large Space Structures and ESA. It presents the results for three different concepts by their materials or numbers of actuators. The *RMS* of the deformation values are between 0.4845 mm and 1.2606 mm. Even if it is hard to compare these results

with the one obtained in this work due to the structure dissimilarities (as the size), it allows to have a general idea on the *RMS* range of values which can be expected.

Hence, the breadboard developed in this thesis shows *RMS* in the same range of value. The control of the ground plane is then considered acceptable compared to the existing solutions using manual actuation. It also shows that the actuators, the rear-structure, and the membrane are well assembled.

Moreover, the *RMS* value does not change drastically between two consecutive tests, which means that the process is repeatable. It is also important to notice that due to the non-linearity between the phase and the distance h , the best *RMS* does not imply to provide the best *RF* performance.

4.6 RF performance

The RF measurements have been performed at IETR in a frequency range between 12.35 GHz and 13.35 GHz. The ground plane is manually actuated to achieve the displacements presented by Tables 4.3 and 4.4. Figure 4.30 shows the antenna mounted in an anechoic chamber at *IETR*.

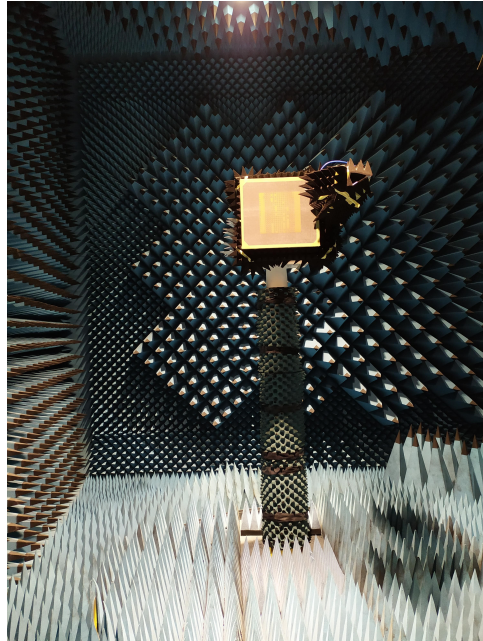


FIGURE 4.30: Photo of the antenna in the anechoic chamber.

To evaluate the RF performance of the antenna, the excitation law applied over the panel by the feeding horn needs to be derived from its radiation pattern. This is illustrated in Figure 4.31.

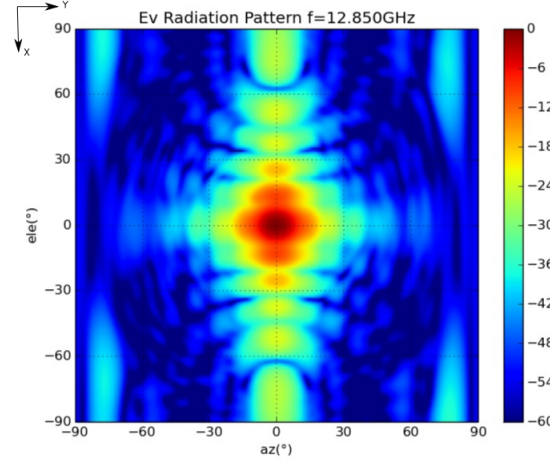


FIGURE 4.31: Radiation pattern of the horn at $f=12.85$ GHz.

By applying this excitation law to the predicted phase provided by the cells, it is possible to deduce the predicted (u, v) pattern for S_1 , which is presented in Figure 4.32.

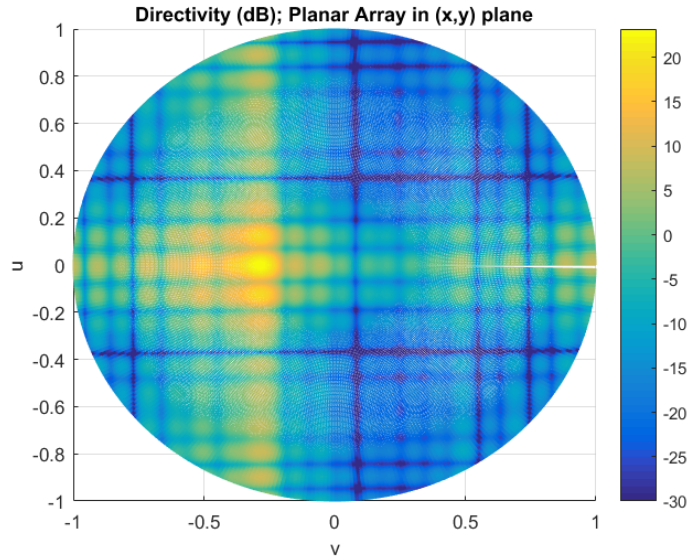


FIGURE 4.32: Predicted (u, v) pattern for S_1 at $f=12.85$ GHz.

As it can be noticed in Figure 4.32, the application of the excitation law implies a modification of the predicted (u, v) pattern previously presented in Figure 4.21

which does not consider it. Indeed, the main beam is enlarged compared to the ideal one along the v -axis for $u=0$ and along u -axis for $v=-0.25$, which leads to a lower directivity level. This shows that the compensation of the phase error made along the x -axis by the modification of the ground plane shape is not fully achieved.

Figure 4.33 illustrates the measured (u, v) pattern for S_1 considering the central frequency $f=12.85$ GHz.

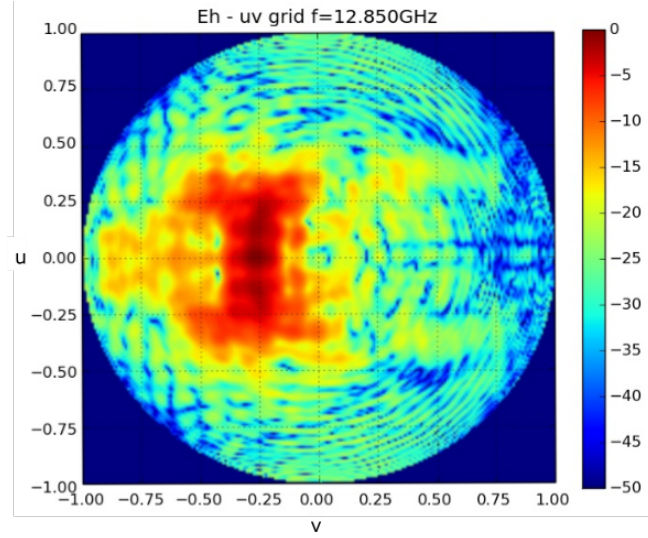


FIGURE 4.33: Measured (u, v) pattern for S_1 at $f=12.85$ GHz.

Figure 4.33 shows the same enlargement of the main lobe along the v -axis for $u=0$ and along the u -axis for $v=-0.25$ as the predicted (u, v) pattern illustrated in Figure 4.32.

The prediction seems more accurate for the enlargement along the v -axis than along the u -axis. The wider beam along the u -axis as the one predicted in Figure 4.32 can be explained by a non-optimal compensation of the phase error due to the wrong layout used.

Furthermore, Figure 4.33 presents higher level of secondary lobes than Figure 4.32 for the predicted (u, v) pattern. This enlargement of the beam leads to a loss of power and so, a low directivity level as illustrated in Table 4.6. The directivity level could also be impacted by:

- the hypothesis taken concerning the local planarity of the ground plane under each cell.

- the deformation of the ground plane
- the errors of h ...

Unfortunately, these investigations have not been pursued during the thesis due to the lack of time even if several paths have been identified to improve the design methodology. Appendix A presents notably some studies done in this context.

Frequency	12.35	12.85	13.35
Predicted directivity	25 dB	26.5 dB	24 dB
Measured directivity	20 dB	20.2 dB	20 dB

TABLE 4.6: Predicted and measured directivities for coverages S_1 and S_2 .

The average difference value between predicted and measured directivity presented in Table 4.6 is around 5.2 dB which is too important to consider that the results are satisfactory. Figure 4.34 presents the directivity measured for all studied frequencies.

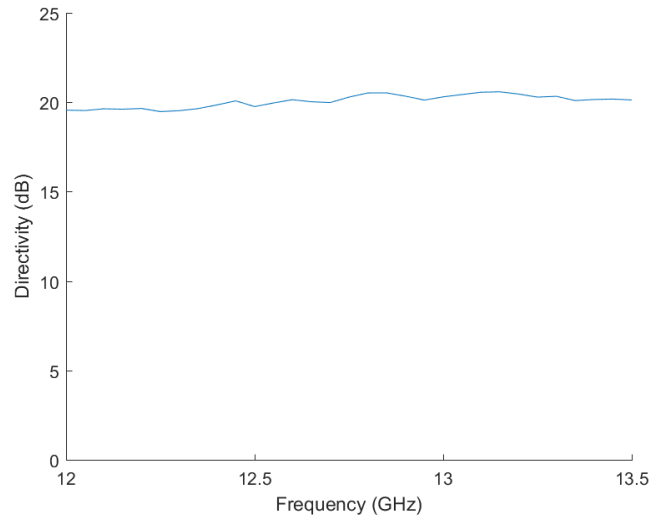


FIGURE 4.34: Measured directivity for the whole frequency range.

Even if the directivity level is not satisfactory considering the targeted ones, Figure 4.34 shows that the antenna has a stable behavior in the whole studied frequency range. The impact of the distance h on the frequency dispersion of the cells has been studied in Chapter 2 and has highlighted different cells behaviors in frequency

with some of them critical. The design methodology has then be identified in order to avoid distance h close to 0 mm or $\frac{\lambda}{2}$ (as a reminder, this has been executed by adding phase offset to the ideal phase laws). Considering the frequency stability of the array, this method seems to be interesting to simplify the cells selection.

The predicted normalized field produced for each frequency using the array factor computation and the results obtained by measurements are then compared for the cut-plane $\Phi=90^\circ$. The normalized field for the cut-plane $\Phi=90^\circ$ are presented Figures 4.35, 4.36, and 4.37 for the central frequency and the extreme ones.

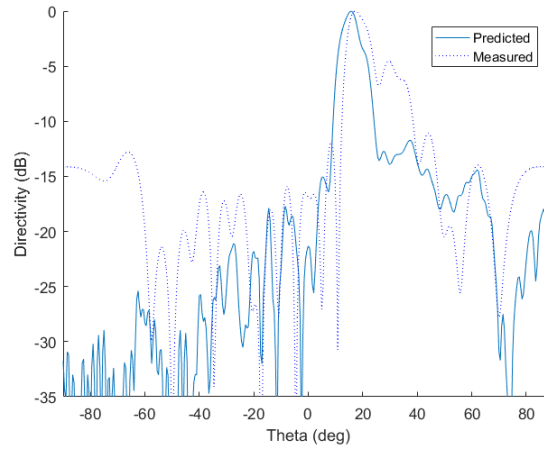


FIGURE 4.35: Normalized field at $f=12.85$ GHz, Cut-plane $\Phi=90^\circ$.

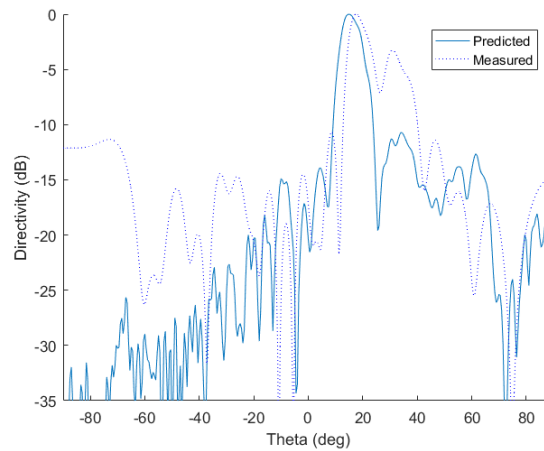


FIGURE 4.36: Normalized field at $f=12.35$ GHz, Cut-plane $\Phi=90^\circ$.

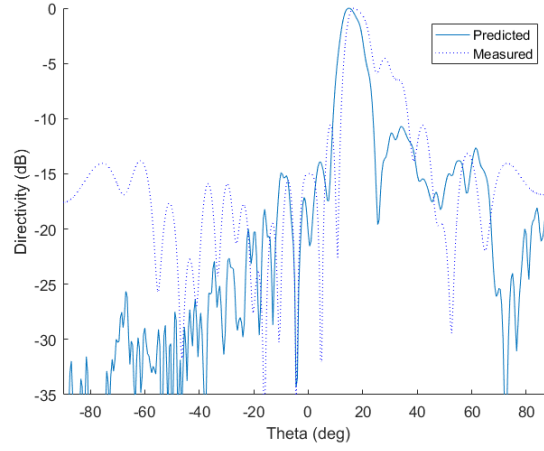


FIGURE 4.37: Normalized field at $f=13.35$ GHz, Cut-plane $\Phi=90^\circ$.

Consequently, considering Figures 4.35, 4.36 and 4.37, it can be noticed that the predicted and the measured profiles of the normalized field show an acceptable agreement in the main plane even if a shift along θ is noticeable.

The acceptable correlation between the predicted and measured radiation patterns profiles lets expect better results with the last updated methodology even in terms of directivity level.

4.7 Conclusion

Chapter 4 presents the breadboard designed to validate the concept of the two-configurations *RA* developed in Chapter 3.

The design and conception of this prototype has revealed several technical constraints and requirements to respect in order to ensure good alignment and parallelism specifications of the components. These requirements have been deduced from the necessity to provide with good accuracy the wanted distance h to each cell constituting the panel.

To verify the control and prediction of the ground plane deformation, a series of photogrammetry tests have been performed. The results obtained are acceptable, and show its repeatability capability which is mandatory for a *RRA*.

Once the control of the deformation has been validated, the antenna has been measured in the anechoic chamber. The RF measurements show an acceptable

correlation between the normalized predicted and measured radiation patterns for the first configuration. Nevertheless, it presents a big directivity loss explained by the non-optimal ground plane deformation due notably to the layout error made during the design process. Other paths to explain the differences between measurements and predicted results would be to study the impact of ground plane deformation, the local planarity hypothesis of the database, the impact of the wave incidence on the cells phase response, or the non-ideal deformation of the ground plane.

Chapter 5

Conclusion

This thesis proposes a new concept of reconfigurable reflectarray antennas (*RRAs*) based on the modification of its ground plane shape. This new type of antenna relies on printed reflectarray antennas technology and Phoenix cells capabilities to provide dynamical modification of the radiation patterns. This reconfiguration is based on the principle that the modification of the distance between the substrate on which the reflecting elements are printed and the ground plane (noted h) leads to a modification of each radiating element's reflected phase.

The first chapter investigates the existing types of antennas and reconfiguration methods to propose a state-of-art. Among them, the reflectarray antennas consist of arrays of radiating elements periodically spaced on a flat surface to reflect the incident wave from a feed source in the desired direction. Hence, they are considered as a hybrid between reflector antennas and array antennas.

Considering the advantages of this new antenna technology, this concept relies on the mechanical reconfiguration of the *RRA* which has been preferred in this work to the three other methods (electrical, optical, material change) notably to investigate the advantages and limitations of this kind of reconfiguration. Nevertheless, the dependence between the ground plane shape and the RF performances of the antenna leads to a multi-objectives optimization such as proposed in this work. This methodology's primary purpose is therefore to find the design which enhances the RF performances while maintaining low levels of deformations to ensure the low-profile characteristic of the *RA*. These are conflicting objectives, and it underlines several problems in terms of engineering aspects such as the control and the prediction of the ground plane deformations. It is even more complicated

as the good accuracy of this prediction directly influences the RF performance predictions.

The first issue is then to model the cells behavior versus the distance to the ground plane to initialize the definition of the design methodology. In Chapter 2, a semi-analytical tool has been developed and detailed. It is used to create a database which links the distance h , the geometry of the cells, and its reflected phase. The analysis of different geometries led to categories of cells regarding their behavior with the distance h . This highlights the necessity to correctly select the cells to avoid degradation of the radiation pattern as the impact of this distance could significantly affect the reflected phase of the cells or their frequency dispersion.

Using the information gathered about the reflecting elements and their behavior versus h , the third chapter proposes a design methodology to provide, at one frequency, an optimized array layout associated with two-ground plane shapes, two radiation patterns. Hence, the aim is that the antenna can provide two-configuration with the same layout. In the first instance, some simplifications are applied to identify a procedure. This methodology is then applied to an test case and discussed to be improved. Mechanical model of the ground plane deformation and fullwave model of the panel are used to validate the model while considering realistic constraints. Finally, the final design is compared with a shaped reflector to identify the advantages and drawbacks of this concept compared to existing ones. The main difference with shaped reflector is that the *RRA* needs a lower magnitude of deformation (approx. more than twice the magnitude of deformation for the shaped reflector). This represents a significant interest as it reduces the constraints on the material while ensuring the same RF performances.

A breadboard has been used to prove the reconfiguration capability of the *RRA* with a flexible ground plane. It has been assembled at Large Space Structures and tested for the RF measurements at IETR. Two series of tests have been carried out, a mechanical to validate the prediction model of the ground plane deformation and RF measurements to ensure that the antenna provides the desired radiation patterns. The photogrammetry tests have demonstrated an acceptable prediction of the deformation compared to the state-of-the-art with manual actuators and the repeatability capacity of this deformation. Due to an error during the design of the panel, only one coverage has been tested. The RF measurements show an acceptable correlation between the normalized predicted and measured radiation patterns profiles and underline the good compensation capability of the antenna.

Indeed, the deformations have been identified considering an established design of the panel and distribution of the actuators. Nevertheless, an important loss of directivity prevents to make a clear conclusion. Indeed, the methodology developed in this work helps to identify the starting parameters for such technology and to propose a first non-optimal solution. In this context, several preliminary assessments and priorities have been considered such as the uniform actuators distribution, the need to minimize the number of actuators... This first path leads to the necessity of more investigations notably on the impact of the ground plane deformation on the radiation pattern. The different studies done have also highlighted the necessity of a design process considering simultaneously the mechanical and RF aspects of this type of reconfigurable antennas.

The main perspective to improve this technology is to increase the membrane deformation and its prediction accuracy considering the selection of cells, the actuators distribution and the membrane characteristics. The main perspective for this work would be to improve the control of the flexible membrane. As it has been shown, it is of prime importance to perfectly master its shape in order to produce the required phase shifts over the reflecting panel. Two complementary directions have to be followed: increase the number of actuators to better reach the optimal shape and improve the prediction of its impact on radiation (for instance the influence of a non parallel ground at the cell level). The main idea to achieve the ideal shape is to increase the number of actuators to control more precisely the membrane behavior. Nevertheless, this implies a gain of mass and cost.

Another way to improve the methodology detailed in this document could be to increase the number of coverages targeted as it has been initiated in the [Appendix A](#).

Appendix A

Investigation for a three-configurations *RRR*

Contents

A.1 Description of the proposed structure	133
A.1.1 Initial cells' selection process	135
A.1.2 Refinement in the selection process	136
A.2 Results and limits	136
A.2.1 Optimized design	136
A.2.2 Theoretical radiation patterns	137
A.2.3 Radiation patterns using fullwave simulations	140

In these investigations, the goal was to optimize the radiation pattern of the *RAA* for three different configurations. As in the two-configuration case *RAA* presented in this document, the design of the panel consists in optimizing three different types of parameters: the geometry of the M cells forming the panel, the number (N) of regularly distributed actuators and their vertical displacements for the three configurations. The required phase laws must again be provided with the best accuracy while minimizing the number of actuators. In the meantime, the maximum slope of the membrane must be kept lower than 15%, which is compatible with acceptable stress in existing materials used to realize it [39].

A.1 Description of the proposed structure

As for the two-configurations case, a linear panel is considered at a first instance to simplify the methodology. This panel consists of a flat dielectric layer supporting $M=38$ printed *RA* cells with an inter-element spacing equals to $P=8$ mm at a frequency $f=12.2$ GHz. N actuators are distributed regularly along the flexible ground plane to control its shape. As for the case detailed in Chapter 3, one actuator is associated to each cell ($N=M$) at a first instance, then the number is reduced to obtain a realistic system.

For this new *RAA*, the panel is intended to provide three different patterns named (S_1 , S_2 and S_3), each one being associated to a particular deformation of the ground membrane. These patterns have been derived from the 1D-cuts of an actual space mission with three different coverages over Central and South America, in the 11.2-14.5 GHz band. The panel is assumed to be used as a sub-reflector in a Cassegrain configuration. Figure A.1 shows the phase of the reflection coefficient of each cell constituting the *RA* panel.

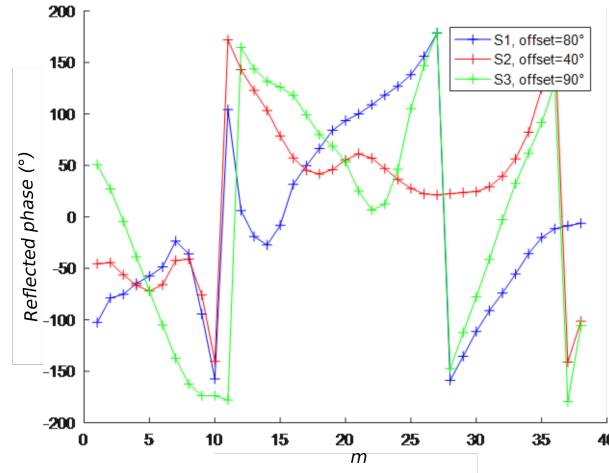


FIGURE A.1: Phase laws that the cells along the panel have to produce for the three patterns (S_1 , S_2 , and S_3 at $f=12.2$ GHz).

It has been shown in Chapter 3 that even if the relationship between the reflected phase of the cells and the distance h is not linear, a minimization of the variation of the phase that an element has to provide helps to avoid big deformations. Consequently, phase offsets have been identified and optimized to minimize the differences between the three cases S_1 , S_2 and S_3 .

As for the test case illustrated in the previous chapters, second-order Phoenix cells [2] are used due to its good performance detailed in Chapter 1. A large number of such geometries is first simulated with the semi-analytical tool presented in the Chapter 2, assuming periodicity and normal incidence. This gives a database for the cells selection process. It is important to note that this database is not the same as the one used for the previous two-configuration case as it is not the same frequency range used.

Figure A.2 shows the variations of the reflected phase for a non-exhaustive set of cell geometries versus h at 12.2 GHz. As it has been detailed in Chapter 2, it exists different types of cell behavior versus h with various sensitivities to a variation of this distance.

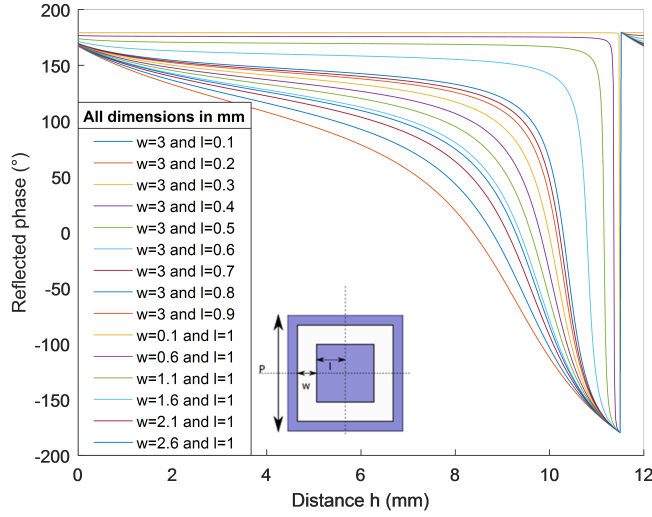


FIGURE A.2: Impact of the distance h on the reflected phase of the cells composing the database.

A.1.1 Initial cells' selection process

The design process itself starts with the selection of the first cell in the panel. It is defined by (G_1, h_1) , G_1 being its geometry and h_1 a 3-component vector:

$$h_i = \begin{bmatrix} h_i^{S_1} & h_i^{S_2} & h_i^{S_3} \end{bmatrix} \quad (\text{A.1})$$

with $h_i^{S_i}$ the convenient distance to ground plane so that geometry G_1 produces the required phase for pattern S_i . Among possible solutions in the database, the one with less dispersion is preferred. The frequency dispersion of the cell is defined as the ratio of the absolute difference between the phases reached at the two extreme frequencies and the frequency range.

The second cell is then selected and the vector h_2 is determined in such a way that the required phases at S_1 , S_2 and S_3 are reached, the membrane slope is kept below the required threshold and the dispersion is minimized. If no solution is found, the frequency dispersion constraint is relaxed, then the slope one. If there is still no solution, the starting point (cell1) has to be changed. The process is finally repeated for the successive cells in the array to determine the M cells and h_j vectors ($1 < j < M$).

At this stage, an initial solution is available. However, it still has to be processed further. Indeed, two aspects have to be addressed. Firstly, we remind that the process may have relaxed somehow the dispersion and slope constraints. Secondly, it considered ideal h_j vectors for all cells in the array. Unfortunately, this is only possible if one actuator is used for each cell, which is not feasible due to cost, weight and complexity. The subsequent refinement process then consists in reaching an acceptable trade-off between these various constraints.

A.1.2 Refinement in the selection process

The main objective of the refinement process is to progressively decrease the number of actuators. As a first hypothesis, the membrane shape is supposed to be linear between two consecutive actuators. We also remind that we enforce a regular distribution of actuators along the panel. Due to the reduced number of actuators, h_j can no longer reach its required value for each cell. Consequently, some phase errors are now produced over the panel, which have to be minimized. In practice, the refinement consists in repeating the iterative process described before while decreasing the number of actuators until the average error is not acceptable anymore. More precisely, at each iteration, the array radiation patterns are recalculated while taking into account the actual phases produced by the cells for the considered deformation. These obtained patterns are compared to the desired ones for the three possible configurations (S_1 , S_2 and S_3) and for different frequencies in the band. An average error is thus derived, which has to be minimized.

A.2 Results and limits

A.2.1 Optimized design

The obtained array needs four actuators positionned under cells 1, 13, 26, and 38. As previously, two of them are placed at the extremities of the membrane. Figure A.3 is a representation of the optimized deformations. Actuators along the panel are illustrated by the stars in the figure.

For all three possible deformations, h_j values are in the range $[0.06, 4.31]$ mm. The maximum slope of the ground plane (which can be critical from a mechanical point of view) across the three coverages is 4.43%.

Until now, linear variations have been assumed between two consecutive actuators, as can be seen in the figure. For a more realistic representation of the deformed ground plane, polynomial approximations (6th order) can be introduced. They are given by the dotted lines in Figure [?]. They will be used for simulations in the next section. Note that this involves a slight modification of h_j values. In practice, it has been compensated by few modifications of some cell geometries, as a last step in the design process.

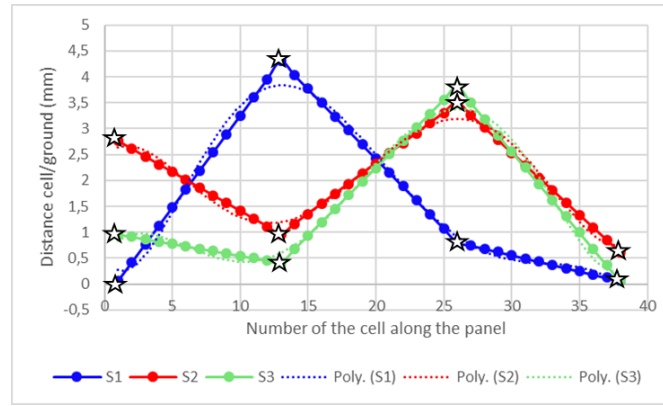


FIGURE A.3: Optimized ground deformation for S_1 , S_2 , and S_3 (cells are represented by dots and actuators by stars).

A.2.2 Theoretical radiation patterns

Figures A.4, A.5, and A.6 compare the desired radiation patterns (assuming the required phase laws are perfectly reached) and the ones obtained from the optimized design for the three radiation pattern configurations S_1 , S_2 and S_3 respectively. These theoretical patterns are based on array factor calculations using Matlab and are given here at $f=12.2$ GHz.

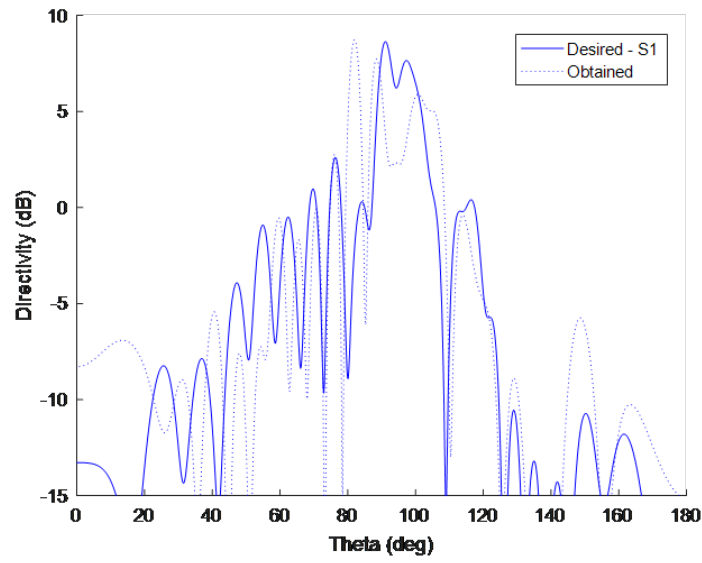


FIGURE A.4: Theoretical radiation patterns (desired and obtained ones) for S_1 at 12.2 GHz.

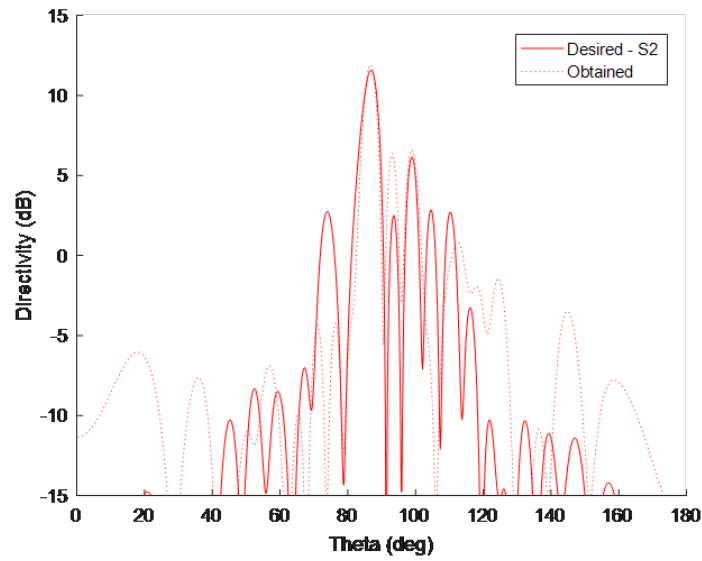


FIGURE A.5: Theoretical radiation patterns (desired and obtained ones) for S_2 at 12.2 GHz.

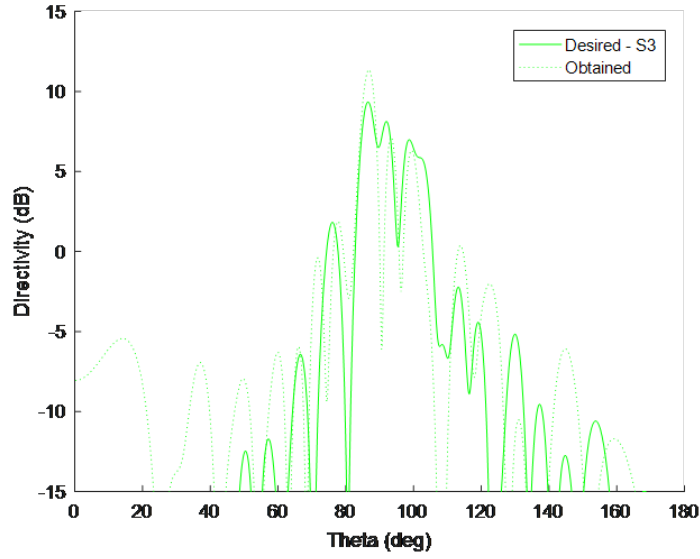


FIGURE A.6: Theoretical radiation patterns (desired and obtained ones) for S_3 at 12.2 GHz.

Although ground plane deformations result from a quite complex design process and only four actuators are used to shape the membrane, the obtained patterns overall fit the desired evolution. It must also be reminded that the synthesis process aimed at minimizing the average error over the bandwidth and thus couldn't produce a perfect match at a single frequency. To get a more quantitative comparison, the error between the desired patterns and the obtained ones is given in Table.1 for a few frequencies, including the two extreme ones.

	S_1	S_2	S_3
11.2 GHz	9.3%	2.8%	5.5%
12.2 GHz	8.3%	2.4%	5.2%
14.5 GHz	7.1%	3.2%	5.9%

TABLE A.1: Percentage of error in the radiation patterns.

For the optimized design, the maximum error over the band is 9.3%. A smaller error could be achieved for an increased number of actuators. Typically, simulations have shown that the minimum error is 4.6% for $N=9$. This result is computed using an array factor computation and not a fullwave one.

A.2.3 Radiation patterns using fullwave simulations

We now use full-wave simulations (HFSS) to model the overall designed panel (cf. Figure A.7). This aims at improving the realism of the predictions. These phase responses computed in the database assume local periodicity and parallelism between cells and ground, which are questionable approximations. To make full-wave simulations simpler, the array is now supposed to be excited by a y-polarized plane wave under normal incidence. The resulting patterns at 12.2 GHz are shown in Figure A.8, A.9, and A.10 for the three configurations S_1 , S_2 , and S_3 respectively. They are compared to theoretical results based on array factor calculations using Matlab, as explained in the previous section.

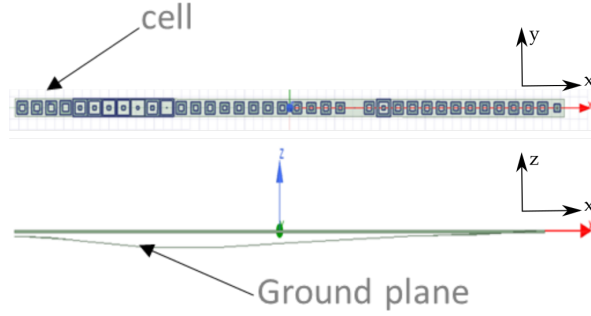


FIGURE A.7: HFSS model (top view and side views for S_1).

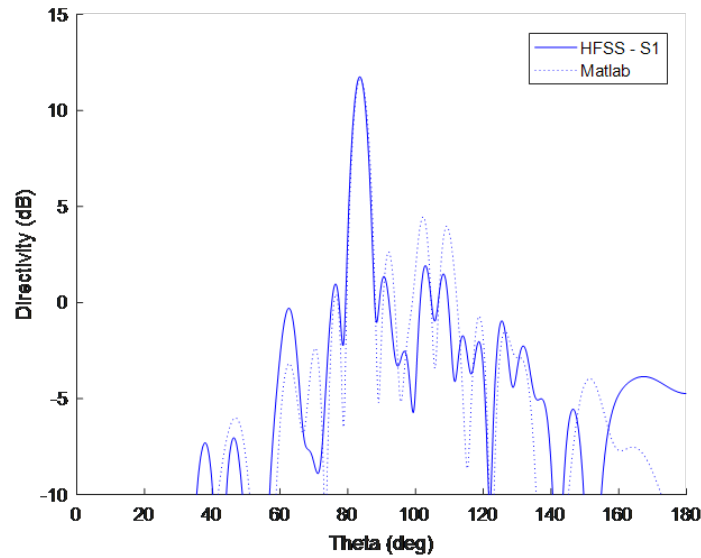


FIGURE A.8: HFSS radiation patterns and targeted ones for S_1 in the case of a plane incident wave.

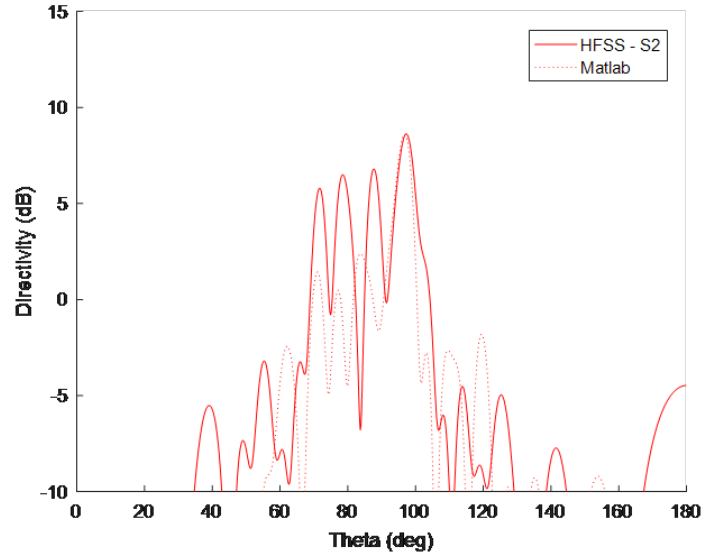


FIGURE A.9: HFSS radiation patterns and targeted ones for S_2 in the case of a plane incident wave.

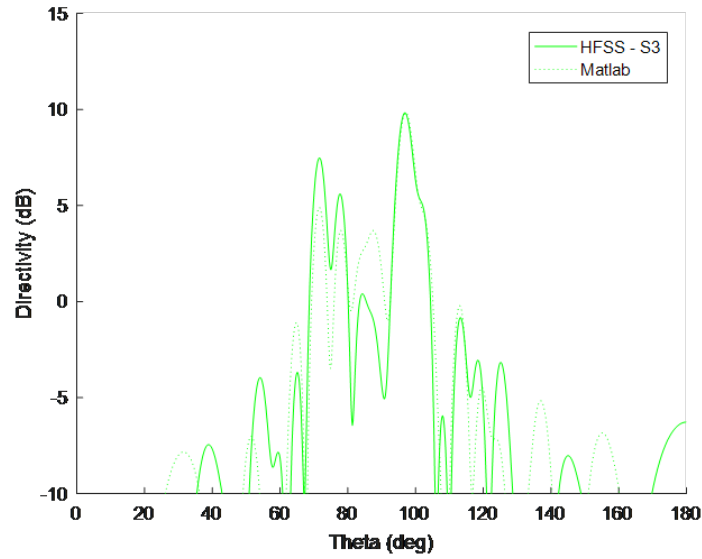


FIGURE A.10: HFSS radiation patterns and targeted ones for S_3 in the case of a plane incident wave.

The agreement is overall good especially for the main lobes for S_1 and S_3 . Nevertheless, big differences in the secondary lobes could be noticed notably for S_2 . This suggests the simplified model used in the design approach is satisfactory and used assumptions (local periodicity and local parallelism of the ground plane under each cell) are acceptable for a preliminary design. Improvements of the radiation

patterns could be expected while increasing the number of actuators. Nevertheless, this depends on the ideal ground plane shapes to reach and the actuators distribution. Moreover, this also implies additional weight, cost, and complexity.

It seems that even for a number of configurations limited to 3, the system is already complex notably due to the set of configurations targeted.

Bibliography

- [1] D. Gonzalez-Ovejero O. Yurduseven M. J. Radway R. E. Hodges P. Estabrook J. D. Baker D. J. Bell T. A. Cwik G. Chattopadhyay N. Chahat, E. Decrossas. Advanced cubesat antennas for deep space and earth science missions: A review. *IEEE Antennas and Propagation Magazine*, 61(5):37–46, 2019.
- [2] V. Richard, R. Gillard, R. Loison, H. Legay, M. Romier, J. . Martinaud, D. Bresciani, and F. Delepaux. Advanced synthesis of reflectarrays using a spherical mapping of the 2nd order phoenix cell. In *2019 13th European Conference on Antennas and Propagation (EuCAP)*, pages 1–5, 2019.
- [3] N. Behdad and K. Sarabandi. A varactor-tuned dual-band slot antenna. *IEEE Transactions on Antennas and Propagation*, 54(2):401–408, 2006.
- [4] E. Antonino-Daviu, M. Cabedo-Fabres, M. Ferrando-Bataller, and A. Vila-Jimenez. Active uwb antenna with tunable band-notched behaviour. *Electronics Letters*, 43(18):959–960, 2007.
- [5] W. Jeong, S. Lee, W. Lim, H. Lim, and J. Yu. Tunable band-notched ultra wideband (uwb) planar monopole antennas using varactor. In *2008 38th European Microwave Conference*, pages 266–268, 2008.
- [6] C. R. White and G. M. Rebeiz. Single- and dual-polarized tunable slot-ring antennas. *IEEE Transactions on Antennas and Propagation*, 57(1):19–26, 2009.
- [7] H. Jiang, M. Patterson, C. Zhang, and G. Subramanyam. Frequency tunable microstrip patch antenna using ferroelectric thin film varactor. In *Proceedings of the IEEE 2009 National Aerospace Electronics Conference (NAECON)*, pages 248–250, 2009.

- [8] S. . Oh, Y. . Jung, Y. . Ju, and H. . Park. Frequency-tunable open-ring microstrip antenna using varactor. In *2010 International Conference on Electromagnetics in Advanced Applications*, pages 624–626, 2010.
- [9] S. Shelley, J. Costantine, C. G. Christodoulou, D. E. Anagnostou, and J. C. Lyke. Fpga-controlled switch-reconfigured antenna. *IEEE Antennas and Wireless Propagation Letters*, 9:355–358, 2010.
- [10] D. Peroulis, K. Sarabandi, and L. P. B. Katehi. Design of reconfigurable slot antennas. *IEEE Transactions on Antennas and Propagation*, 53(2):645–654, 2005.
- [11] M. K. Fries, M. Grani, and R. Vahldieck. A reconfigurable slot antenna with switchable polarization. *IEEE Microwave and Wireless Components Letters*, 13(11):490–492, 2003.
- [12] Symeon Nikolaou, R. Bairavasubramanian, C. Lugo, I. Carrasquillo, D. C. Thompson, G. E. Ponchak, J. Papapolymerou, and M. M. Tentzeris. Pattern and frequency reconfigurable annular slot antenna using pin diodes. *IEEE Transactions on Antennas and Propagation*, 54(2):439–448, 2006.
- [13] N. Jin, Fan Yang, and Y. Rahmat-Samii. A novel patch antenna with switchable slot (pass): dual-frequency operation with reversed circular polarizations. *IEEE Transactions on Antennas and Propagation*, 54(3):1031–1034, 2006.
- [14] S. Chen, J. Row, and K. Wong. Reconfigurable square-ring patch antenna with pattern diversity. *IEEE Transactions on Antennas and Propagation*, 55(2):472–475, 2007.
- [15] S. Wu and T. Ma. A wideband slotted bow-tie antenna with reconfigurable cpw-to-slotline transition for pattern diversity. *IEEE Transactions on Antennas and Propagation*, 56(2):327–334, 2008.
- [16] B. Kim, B. Pan, S. Nikolaou, Y. Kim, J. Papapolymerou, and M. M. Tentzeris. A novel single-feed circular microstrip antenna with reconfigurable polarization capability. *IEEE Transactions on Antennas and Propagation*, 56(3):630–638, 2008.

- [17] R. Chen and J. Row. Single-fed microstrip patch antenna with switchable polarization. *IEEE Transactions on Antennas and Propagation*, 56(4):922–926, 2008.
- [18] J. Sarrazin, Y. Mahe, S. Avrillon, and S. Toutain. Pattern reconfigurable cubic antenna. *IEEE Transactions on Antennas and Propagation*, 57(2):310–317, 2009.
- [19] J. Perruisseau-Carrier, P. Pardo-Carrera, and P. Miskovsky. Modeling, design and characterization of a very wideband slot antenna with reconfigurable band rejection. *IEEE Transactions on Antennas and Propagation*, 58(7):2218–2226, 2010.
- [20] P. Qin, A. R. Weily, Y. J. Guo, T. S. Bird, and C. Liang. Frequency reconfigurable quasi-yagi folded dipole antenna. *IEEE Transactions on Antennas and Propagation*, 58(8):2742–2747, 2010.
- [21] Chang won Jung, Ming-jeer Lee, G. P. Li, and F. De Flaviis. Reconfigurable scan-beam single-arm spiral antenna integrated with rf-mems switches. *IEEE Transactions on Antennas and Propagation*, 54(2):455–463, 2006.
- [22] G. H. Huff and J. T. Bernhard. Integration of packaged rf mems switches with radiation pattern reconfigurable square spiral microstrip antennas. *IEEE Transactions on Antennas and Propagation*, 54(2):464–469, 2006.
- [23] B. A. Cetiner, G. Roqueta Crusats, L. Jofre, and N. Biyikli. Rf mems integrated frequency reconfigurable annular slot antenna. *IEEE Transactions on Antennas and Propagation*, 58(3):626–632, 2010.
- [24] A. Grau, J. Romeu, M. Lee, S. Blanch, L. Jofre, and F. De Flaviis. A dual-linearly-polarized mems-reconfigurable antenna for narrowband mimo communication systems. *IEEE Transactions on Antennas and Propagation*, 58(1):4–17, 2010.
- [25] S. Nikolaou, N. D. Kingsley, G. E. Ponchak, J. Papapolymerou, and M. M. Tentzeris. Uwb elliptical monopoles with a reconfigurable band notch using mems switches actuated without bias lines. *IEEE Transactions on Antennas and Propagation*, 57(8):2242–2251, 2009.

- [26] E. Erdil, K. Topalli, M. Unlu, O. A. Civi, and T. Akin. Frequency tunable microstrip patch antenna using rf mems technology. *IEEE Transactions on Antennas and Propagation*, 55(4):1193–1196, 2007.
- [27] L. N. Pringle, P. H. Harms, S. P. Blalock, G. N. Kiesel, E. J. Kuster, P. G. Friederich, R. J. Prado, J. M. Morris, and G. S. Smith. A reconfigurable aperture antenna based on switched links between electrically small metallic patches. *IEEE Transactions on Antennas and Propagation*, 52(6):1434–1445, 2004.
- [28] C. J. Panagamuwa, A. Chauraya, and J. C. Vardaxoglou. Frequency and beam reconfigurable antenna using photoconducting switches. *IEEE Transactions on Antennas and Propagation*, 54(2):449–454, 2006.
- [29] M. R. Chaharmir, J. Shaker, M. Cuhaci, and A. . Sebak. Novel photonicallly-controlled reflectarray antenna. *IEEE Transactions on Antennas and Propagation*, 54(4):1134–1141, 2006.
- [30] Y. Tawk, A. R. Albrecht, S. Hemmady, G. Balakrishnan, and C. G. Christodoulou. Optically pumped frequency reconfigurable antenna design. *IEEE Antennas and Wireless Propagation Letters*, 9:280–283, 2010.
- [31] Y. Tawk, J. Costantine, S. E. Barbin, and C. G. Christodoulou. Integrating laser diodes in a reconfigurable antenna system. In *2011 SBMO/IEEE MTT-S International Microwave and Optoelectronics Conference (IMOC 2011)*, pages 794–796, 2011.
- [32] S. J. Mazlouman, M. Soleimani, A. Mahanfar, C. Menon, and R. G. Vaughan. Pattern reconfigurable square ring patch antenna actuated by hemispherical dielectric elastomer. *Electronics Letters*, 47(3):164–165, 2011.
- [33] Y. Tawk and C. G. Christodoulou. A cellular automata reconfigurable microstrip antenna design. In *2009 IEEE Antennas and Propagation Society International Symposium*, pages 1–4, 2009.
- [34] J. Constantine Y. Tawk and C. G. Christodoulou. A frequency reconfigurable rotatable microstrip antenna design. pages 1 – 4, 08 2010.
- [35] D. M. Pozar and V. Sanchez. Magnetic tuning of a microstrip antenna on a ferrite substrate. *Electronics Letters*, 24(12):729–731, 1988.

- [36] L. Dixit and P. K. S. Pourush. Radiation characteristics of switchable ferrite microstrip array antenna. *IEE Proceedings - Microwaves, Antennas and Propagation*, 147(2):151–155, 2000.
- [37] W. Hu, M. Y. Ismail, R. Cahill, J. A. Encinar, V. F. Fusco, H. S. Gamble, D. Linton, R. Dickie, N. Grant, and S. P. Rea. Liquid-crystal-based reflectarray antenna with electronically switchable monopulse patterns. *Electronics Letters*, 43(14), 2007.
- [38] L. Liu and R. J. Langley. Liquid crystal tunable microstrip patch antenna. *Electronics Letters*, 44(20):1179–1180, 2008.
- [39] L. Datashvili, H. Baier, B. Wei, J. Hoffman, E. Wehrle, L. Schreider, C. Mangenot, J. Santiago-Prowald, L. Scolamiero, and J-C. Angevain. Mechanical investigations of in-space-reconfigurable reflecting surfaces. *Proc. ESA Antenna Workshop*, 01 2010.
- [40] W. A. Imbriale. Distortion compensation techniques for large reflector antennas. In *2001 IEEE Aerospace Conference Proceedings (Cat. No.01TH8542)*, volume 2, pages 2/799–2/805 vol.2, 2001.
- [41] L. Datashvili, H. Baier, B. Wei, S. Endler, and L. Schreider. Design of a morphing skin using flexible fiber composites for space-reconfigurable reflectors. 04 2013.
- [42] P. J. B. Clarricoats, Z. Hai, R. C. Brown, G. T. Poulton, and G. E. Crone. A reconfigurable mesh reflector antenna. In *1989 Sixth International Conference on Antennas and Propagation, ICAP 89 (Conf. Publ. No.301)*, pages 112–116 vol.1, 1989.
- [43] H. . Viskum, P. J. B. Clarricoats, and G. A. E. Crone. Coverage flexibility by means of a reconformable subreflector. In *IEEE Antennas and Propagation Society International Symposium 1997. Digest*, volume 2, pages 1378–1381 vol.2, 1997.
- [44] G. Washington, Hwan-Sik Yoon, M. Angelino, and W. H. Theunissen. Design, modeling, and optimization of mechanically reconfigurable aperture antennas. *IEEE Transactions on Antennas and Propagation*, 50(5):628–637, 2002.

- [45] C. Cappellin and K. Pontoppidan. Feasibility study and sensitivity analysis for a reconfigurable dual reflector antenna. In *2009 3rd European Conference on Antennas and Propagation*, pages 2017–2021, 2009.
- [46] P. Gabellini, N. Gatti, C. Capsoni, L. Resteghini, A. Martellucci, and P. Rinous. An on-board reconfigurable antenna system for ka-band broadcasting satellite services. *2012 6th European Conference on Antennas and Propagation (EUCAP)*, pages 2636–2640, 2012.
- [47] R. A. Hoferer and Y. Rahmat-Samii. Subreflector shaping for antenna distortion compensation: an efficient fourier-jacobi expansion with go/po analysis. *IEEE Transactions on Antennas and Propagation*, 50(12):1676–1687, 2002.
- [48] D. Berry, R. Malech, and W. Kennedy. The reflectarray antenna. *IEEE Transactions on Antennas and Propagation*, 11(6):645–651, 1963.
- [49] J. Volakis. *Antenna Engineering Handbook*, volume 23. 06 2007.
- [50] S. V. Hum and J. Perruisseau-Carrier. Reconfigurable reflectarrays and array lenses for dynamic antenna beam control: A review. *IEEE Transactions on Antennas and Propagation*, 62(1):183–198, 2014.
- [51] V. Richard. *Outils de synthèse pour les réseaux réflecteurs exploitant la cellule Phoenix et les réseaux de neurones*. PhD thesis, INSA de Rennes, April 2018.
- [52] P. D. Potter W. V. T Rusch. *Analysis of reflector antennas*. Academic Press, 2013.
- [53] A. W. Rudge and M. J. Withers. New technique for beam steering with fixed parabolic reflectors. *Proceedings of the Institution of Electrical Engineers*, 118(7):857–863, 1971.
- [54] P. Hannan. Microwave antennas derived from the cassegrain telescope. *IRE Transactions on Antennas and Propagation*, 9(2):140–153, 1961.
- [55] W. V. T. Rusch, A. Prata, Y. Rahmat-Samii, and R. A. Shore. Derivation and application of the equivalent paraboloid for classical offset cassegrain and gregorian antennas. *IEEE Transactions on Antennas and Propagation*, 1990.

- [56] Mark T Ma. Theory and application of antenna arrays(book). *New York, Wiley-Interscience, 1974. 422 p*, 1974.
- [57] R. C. Hansen. *Phased array antennas*, volume 213. John Wiley & Sons, 2009.
- [58] A. G. Roederer. Reflectarray antennas. In *2009 3rd European Conference on Antennas and Propagation*, pages 18–22, 2009.
- [59] C. S. Malagisi. Microstrip disc element reflect array. In *EASCON '78; Electronics and Aerospace Systems Convention*, pages 186–192, January 1978.
- [60] J. P. Montgomery. A microstrip reflectarray antenna element. *Antenna Applications Symposium*, 1978.
- [61] P. Nayeri, F. Yang, and A. Z. Elsherbeni. Single-feed multi-beam reflectarray antennas. In *2010 IEEE Antennas and Propagation Society International Symposium*, pages 1–4, 2010.
- [62] F. Yang. Progress in reflectarray antenna research: From enhanced frequency features to advanced radiation capabilities. In *2013 7th European Conference on Antennas and Propagation (EuCAP)*, pages 2484–2487, 2013.
- [63] A. Z. Elsherbeni, P. Nayeri, and F. Yang. Reflectarray antennas for space applications. In *2012 IEEE International Conference on Ultra-Wideband*, pages 362–365, 2012.
- [64] J. A. Encinar. Analysis and design of dual frequency reflectarrays using microstrip stacked patches of variable size. In *1996 26th European Microwave Conference*, volume 1, pages 221–224, 1996.
- [65] M. Beccaria, P. Pirinoli, M. Orefice, and P. di Torino. Design and analysis of reflectarray antennas printed on curved surfaces. In *2016 IEEE Sixth International Conference on Communications and Electronics (ICCE)*, pages 238–241, 2016.
- [66] P. De Vita, A. Di Maria, A. Freni, G. L. Dassano, P. Pirinoli, and R. E. Zich. Design, optimization and analysis of broadband reflectarray antennas. In *2007 International Conference on Electromagnetics in Advanced Applications*, pages 1070–1072, 2007.

- [67] J. Huang, C. Han, and K. Chang. A cassegrain offset-fed dual-band reflectarray. In *2006 IEEE Antennas and Propagation Society International Symposium*, pages 2439–2442, 2006.
- [68] J. Huang. Capabilities of printed reflectarray antennas. In *Proceedings of International Symposium on Phased Array Systems and Technology*, pages 131–134, 1996.
- [69] C. Apert, T. Koleck, P. Dumon, T. Dousset, and C. Renard. Erasp: A new reflectarray antenna for space applications. In *2006 First European Conference on Antennas and Propagation*, pages 1–5, 2006.
- [70] J. Huang. Reflectarray antenna. *Encyclopedia of RF and Microwave Engineering*, 2005.
- [71] Zhi-Quan Liu, Hui Qiu, Xiao Li, and Shu-Li Yang. Review of large spacecraft deployable membrane antenna structures. *Chinese Journal of Mechanical Engineering*, 30(6):1447–1459, 2017.
- [72] J. Huang. Bandwidth study of microstrip reflectarray and a novel phased reflectarray concept. In *IEEE Antennas and Propagation Society International Symposium. 1995 Digest*, volume 1, pages 582–585 vol.1, 1995.
- [73] D. M. Pozar. Bandwidth of reflectarrays. *Electronics Letters*, 39(21):1490–1491, 2003.
- [74] R. D. Javor, X. . Wu, and K. Chang. Dual polarisation of microstrip reflectarray antenna. *Electronics Letters*, 30(13):1018–1019, 1994.
- [75] R. D. Javor, Xiao-Dong Wu, and Kai Chang. Design and performance of a microstrip reflectarray antenna. *IEEE Transactions on Antennas and Propagation*, 43(9):932–939, 1995.
- [76] R. D. Javor, Xiao-Dong Wu, and Kai Chang. Design and performance of a microstrip reflectarray antenna. *IEEE Transactions on Antennas and Propagation*, 43(9):932–939, 1995.
- [77] J. Huang. Microstrip reflectarray. In *Antennas and Propagation Society Symposium 1991 Digest*, pages 612–615 vol.2, 1991.
- [78] R. D. Javor, Xiao-Dong Wu, and Kai Chang. Beam steering of a microstrip flat reflectarray antenna. In *Proceedings of IEEE Antennas and Propagation*

- Society International Symposium and URSI National Radio Science Meeting*, volume 2, pages 956–959 vol.2, 1994.
- [79] D-C. Chang and M-C. Huang. Multiple-polarization microstrip reflectarray antenna with high efficiency and low cross-polarization. *IEEE Transactions on Antennas and Propagation*, 43(8):829–834, 1995.
- [80] J. A. Encinar, M. Arrebola, L. F. de la Fuente, and G. Toso. A transmit-receive reflectarray antenna for direct broadcast satellite applications. *IEEE Transactions on Antennas and Propagation*, 59(9):3255–3264, 2011.
- [81] J. A. Encinar and J. A. Zornoza. Broadband design of three-layer printed reflectarrays. *IEEE Transactions on Antennas and Propagation*, 51(7):1662–1664, 2003.
- [82] M. R. Chaharmir, J. Shaker, M. Cuhaci, and A. Ittipiboon. A broadband reflectarray antenna with double square rings as the cell elements. In *2006 First European Conference on Antennas and Propagation*, pages 1–4, 2006.
- [83] M. R. Chaharmir, J. Shaker, M. Cuhaci, and A. Ittipiboon. Broadband reflectarray antenna with double cross loops. *Electronics Letters*, 42(2):65–66, 2006.
- [84] L. Moustafa, R. Gillard, F. Peris, R. Loison, H. Legay, and E. Girard. The phoenix cell: A new reflectarray cell with large bandwidth and rebirth capabilities. *IEEE Antennas and Wireless Propagation Letters*, 10:71–74, 2011.
- [85] H. Salti and R. Gillard. A single layer stub-patch phoenix cell for large band reflectarrays. In *2017 11th European Conference on Antennas and Propagation (EUCAP)*, Paris, France, March 2017. IEEE.
- [86] K. Zhang, Y. Fan, J. Xu, and C. Qu. Design of broadband, low cost single layer reflectarray using phoenix cell. In *2013 IEEE International Conference of IEEE Region 10 (TENCON 2013)*, pages 1–4, 2013.
- [87] T. Makdissy, R. Gillard, E. Fourn, M. Ferrando-Rocher, E. Girard, H. Legay, and L. Le Coq. 'Phoenix' reflectarray unit cell with reduced size and inductive loading. *IET Microwaves Antennas and Propagation*, 10(12):1363–1370, 2016.

- [88] Vincent Richard, Renaud Loison, R. Gillard, Hervé Legay, Maxime Romier, J. Martinaud, Daniele Bresciani, and Fabien Delepau. Spherical mapping of the second-order phoenix cell for unbounded direct reflectarray copolar optimization. *Progress In Electromagnetics Research C*, 90:109–124, 01 2019.
- [89] G. L. Davis and R. Tanimoto. *Mechanical Development of Antenna Systems*, pages 425 – 454. 04 2006.
- [90] X. Qi and B. Li Z. Chu, Z. Deng. Modeling and analysis of a large deployable antenna structure. *Acta Astronautica*, 95:51–60, 02 2014.
- [91] H. Fang J. Pearson J. Moore and J. Lin E. Im, M. Thomson. Prospects of large deployable reflector antennas for a new generation of geostationary doppler weather radar satellites. 09 2007.
- [92] S. Pellegrino. Deployable membrane reflectors. 2002.
- [93] R. E. Hodges and M. Zawadzki. Design of a large dual polarized ku band reflectarray for space borne radar altimeter. In *IEEE Antennas and Propagation Society Symposium, 2004.*, volume 4, pages 4356–4359 Vol.4, 2004.
- [94] H. Fang, M. Lou, J. Huang, L. Hsia, and G. Kerdanyan. An inflatable/self-rigidizable structure for the reflectarray antenna. 2001.
- [95] A.W. Love C.G. Cassapakis and A. Palisoc. Inflatable space antennas—a brief overview. volume 3, pages 453 – 459 vol.3, 04 1998.
- [96] J. Liu and S. Sun. *A Brief Survey on Inflatable Deployment Space Structures Research and Development*, pages 773–782. 01 2012.
- [97] J. Huang and A. Fera. Inflatable microstrip reflectarray antennas at x and ka-band frequencies. In *IEEE Antennas and Propagation Society International Symposium. 1999 Digest. Held in conjunction with: USNC/URSI National Radio Science Meeting (Cat. No.99CH37010)*, volume 3, pages 1670–1673 vol.3, 1999.
- [98] J. Huang J. Lin, D. Cadogan and V. Fera. An inflatable microstrip reflectarray concept for ka-band applications. 04 2000.
- [99] J. Huang V. Fera and D. Cadogan. 3-meter ka-band inflatable microstrip reflectarray. 2000.

- [100] D. M. Pozar, S. D. Targonski, and R. Pokuls. A shaped-beam microstrip patch reflectarray. *IEEE Transactions on Antennas and Propagation*, 47(7):1167–1173, 1999.
- [101] E. Labiole, R. Chiniard, R. Gillard, H. Legay, D. Bresciani. A multi facet composite panel reflectarray for a space contoured beam antenna in ku band. *Progress In Electromagnetics Research B*, 54:1–26, 06 2013.
- [102] T. Makdissy. *New phase-shifting cells of low cost and reduced complexity for broadband reflectarray antennas*. Theses, INSA de Rennes, November 2013.
- [103] M. Sterner, N. Somjit, S. U. A. Shah, S. Dudorov, D. Chicherin, A. Raisanen, and J. Oberhammer. Microwave mems devices designed for process robustness and operational reliability. *International Journal of Microwave and Wireless Technologies*, 3:547 – 563, 10 2011.
- [104] S. Pranonsatit, S. Lucyszyn. Rf mems for antenna applications. pages 1988–1992, 01 2013.
- [105] C. G. Christodoulou, Y. Tawk, S. A. Lane, and S. R. Erwin. Reconfigurable antennas for wireless and space applications. *Proceedings of the IEEE*, 100(7):2250–2261, 2012.
- [106] S. V. Hum, M. Okoniewski, and R. J. Davies. Modeling and design of electronically tunable reflectarrays. *IEEE Transactions on Antennas and Propagation*, 55(8):2200–2210, 2007.
- [107] H. Kamoda, T. Iwasaki, J. Tsumochi, T. Kuki, and O. Hashimoto. 60-ghz electronically reconfigurable large reflectarray using single-bit phase shifters. *IEEE Transactions on Antennas and Propagation*, 59(7):2524–2531, 2011.
- [108] H. Legay, B. Pinte, M. Charrier, A. Ziaei, E. Girard, and R. Gillard. A steerable reflectarray antenna with mems controls. In *IEEE International Symposium on Phased Array Systems and Technology, 2003.*, pages 494–499, 2003.
- [109] J. Perruisseau-Carrier and A. K. Skrivervik. Monolithic mems-based reflectarray cell digitally reconfigurable over a 360 ° phase range. *IEEE Antennas and Wireless Propagation Letters*, 7:138–141, 2008.
- [110] X. Li. *Multiple-Input Multiple-Output Communications Systems Using Reconfigurable Antennas*. PhD thesis, École Polytechnique de Montréal, 2015.

- [111] L. Petit, L. Dussopt, and J. . Laheurte. Mems-switched parasitic-antenna array for radiation pattern diversity. *IEEE Transactions on Antennas and Propagation*, 54(9):2624–2631, 2006.
- [112] M. Pisani R. Mahameed, N. Sinha and G. Piazza. Dual-beam actuation of piezoelectric aln rf mems switches monolithically integrated with aln contour-mode resonators. *Journal of Micromechanics and Microengineering - J MICROMECHANIC MICROENGINEER*, 18, 10 2008.
- [113] B. Wu, A. Sutinjo, M. E. Potter, and M. Okoniewski. On the selection of the number of bits to control a dynamic digital mems reflectarray. *IEEE Antennas and Wireless Propagation Letters*, 7:183–186, 2008.
- [114] A. A. Ibrahim, A. Batmanov, and E. P. Burte. Design of reconfigurable antenna using rf mems switch for cognitive radio applications. In *2017 Progress In Electromagnetics Research Symposium - Spring (PIERS)*, pages 369–376, 2017.
- [115] M. Matin. *Wideband, Multiband and Smart Reconfigurable Antennas for Modern Wireless Communications*. 08 2015.
- [116] P. J. B. Clarricoats and H. Zhou. The design and performance of a reconfigurable mesh reflector antenna. In *1991 Seventh International Conference on Antennas and Propagation, ICAP 91 (IEE)*, pages 322–325 vol.1, 1991.
- [117] R. C. Brown, P. Clarricoats, and Z. Hai. The performance of a prototype reconfigurable mesh reflector for spacecraft antenna applications. In *1989 19th European Microwave Conference*, pages 874–878, 1989.
- [118] H. Legay, D. Bresciani, E. Girard, R. Chiniard, E. Labiole, O. Vendier, and G. Caille. Recent developments on reflectarray antennas at thales alenia space. In *2009 3rd European Conference on Antennas and Propagation*, pages 2515–2519, 2009.
- [119] S-A. Gomanne. Réalisation d’une antenne réflecteur reconfigurable basée sur l’utilisation de réseaux transmetteurs. In *Thèse*, 2018.
- [120] X. Yang, S. Xu, F. Yang, M. Li, H. Fang, Y. Hou, S. Jiang, and L. Liu. A mechanically reconfigurable reflectarray with slotted patches of tunable height. *IEEE Antennas and Wireless Propagation Letters*, 17(4):555–558, 2018.

- [121] J. Chum E. Vassos and A. Feresidis. Ultra-low-loss tunable piezoelectric-actuated metasurfaces achieving 360° or 180° dynamic phase shift at millimeter-waves. *Scientific reports*, 2020.
- [122] S. Von Hoerner and Woon-Yin Wong. Improved efficiency with a mechanically deformable subreflector. *IEEE Transactions on Antennas and Propagation*, 27(5):720–723, 1979.
- [123] P. R. Lawson and Jui Lin Yen. A piecewise deformable subreflector for compensation of cassegrain main reflector errors. *IEEE Transactions on Antennas and Propagation*, 36(10):1343–1350, 1988.
- [124] S. Xu, Y. Rahmat-Samii, and W. A. Imbriale. Subreflectarrays for reflector surface distortion compensation. *Antennas and Propagation, IEEE Transactions on*, 57:364 – 372, 03 2009.
- [125] G. Rodrigues, J. Angevain, and J. Santiago-Prowald. Shape control of reconfigurable antenna reflector: Concepts and strategies. In *The 8th European Conference on Antennas and Propagation (EuCAP 2014)*, pages 3541–3545, 2014.
- [126] I. Anderson. On the theory of self-resonant grids. *The Bell System Technical Journal*, 54(10):1725–1731, 1975.
- [127] N. Marcuvitz. *Waveguide handbook*. Number 21. Iet, 1951.
- [128] C. K. Lee and R. J. Langley. Equivalent-circuit models for frequency-selective surfaces at oblique angles of incidence. In *IEE Proceedings H (Microwaves, Antennas and Propagation)*, volume 132, pages 395–399. IET, 1985.
- [129] Potential membrane technologies for in orbit reconfigurable reflector.

Titre : Réseau réflecteur reconfigurable avec un plan de masse flexible

Mots clés : Réseaux réflecteurs, Reconfiguration, Plan de masse déformable

Résumé : Dans le cadre du projet européen Horizon intitulé REVOLVE initié par Thales Alenia Space, Heriot Watt University, Large Space Structures, et l'Institut d'Electronique et des Technologies du numéRique, cette thèse s'intéresse à un nouveau concept d'antennes réseau réflecteurs (RRA) reconfigurables pour application spatiale. Celui-ci repose sur un concept d'antenne basé sur la technologie des réseaux réflecteurs et la reconfiguration mécanique. La distance entre le plan de masse et les cellules imprimées (notée h) sur le réseau est modifiée afin de contrôler leur phase réfléchie et ainsi, changer le diagramme de rayonnement de l'antenne. Cette distance est contrôlée par la déformation du plan de masse à l'aide d'actionneurs placés sous ce dernier. La première étape consiste en l'analyse de l'impact de la distance h sur la phase réfléchie des cellules.

La procédure de conception du RRA nécessite d'être clairement définie étant donné que la principale difficulté est de minimiser le nombre d'actionneurs et l'amplitude de déformation du plan de masse tout en garantissant les propriétés RF et mécanique de l'antenne.

Dans un premier temps, une méthodologie de conception est définie en considérant un contrôle idéal de la déformation et donc, de la distance h . Elle est ensuite appliquée à un exemple de RRA à deux configurations auquel des contraintes plus réalistes relatives au contrôle de la forme du plan de masse (nombre d'actionneurs, comportement du matériau...) sont introduites une par une. Cette méthodologie est ensuite étendue à un réseau 2D et testée à l'aide d'un prototype.

Title : Reconfigurable reflectarray with a flexible ground plane

Keywords : Reflectarrays, Reconfiguration, Deformable ground plane

Abstract : In the frame of the european project Horizon 2020 named REVOLVE project initiated by Thales Alenia Space, Heriot Watt University, Large Space Structures, and Institut d'Electronique et des Technologies du numéRique, this Ph.D. investigates a new Reconfigurable Reflectarray Antenna (RRA) for Space applications. This work proposes a concept based on reflectarray antennas and mechanical reconfiguration. The distance between the ground plane and the metallic elements printed on the higher panel (noted h) is modified to control their reflected phase and therefore, change the radiation pattern provided by the antenna. This distance is tuned by modifying the shape of the ground plane thanks to actuators placed under it. The first step is to analyze the impact of the distance h on the reflected phase of the cells.

The design process of the RRA needs to be clearly defined to identify the parameters to take into account to ensure good performance of the antenna. The main issue is to minimize the number of actuators and the magnitude of the ground plane deformation while ensuring good RF and payload performance.

In the first instance, the methodology is defined considering an ideal control of the deformation and so, of the distance h . It is then applied on a sample of a two-configuration RRA and discussed while introducing one by one realistic constraint (number of actuators, material behavior...) for the control of the ground plane shape.

The design methodology is then extended over a 2D array sample and tested using a prototype.

